

Electronic Supporting Information

for

Pd(/Fe₃O₄)-on-ZIFs: nanoparticle deposition on (nano-)MOFs from ionic liquids

by

Olga Koikolainen,^a Linda Sondermann,^a Stefan Roitsch,^b Ilka Simon,^a Dennis Dietrich,^a Vasily Gvilava,^a Juri Barthel,^c Jörg Thomas,^d Christoph Janiak*^a and Ishtvan Boldog*^a

- a) Institut für Anorganische Chemie und Strukturchemie, Heinrich-Heine-Universität Düsseldorf, Universitätsstraße 1, 40225 Düsseldorf, Germany. E-mails: janiak@hhu.de; boldogi@hhu.de.
- b) Institut für Physikalische Chemie, Universität zu Köln, Luxemburger Str. 116, 50939 Köln.
- c) Gemeinschaftslabor für Elektronenmikroskopie RWTH-Aachen, Ernst Ruska-Centrum für Mikroskopie und Spektroskopie mit Elektronen, 52425 Jülich, Germany.
- d) Abteilung Struktur und Nano- / Mikromechanik von Materialien
Transmissionselektronenmikroskopie, Max-Planck-Institut für Eisenforschung GmbH, 40237 Düsseldorf, Germany

Contents

1	Analytics.....	3
2	Non-analytical instrumentation	6
2.1	Chemicals and materials.....	6
3	Synthesis of the primary ionic liquid, [BMIm](NTf ₂).....	8
3.1	Synthesis of 1-butyl-3-methylimidazolium chloride, [BMIm]Cl	8
3.2	Synthesis of 1-butyl-3-methylimidazolium bistriflimidate, [BMIm](NTf ₂).....	9
4	Synthesis of MOF supports.....	10
4.1	Special methods	10
	<i>Summary on the properties of the MOF-supports</i>	<i>10</i>
4.2	Synthesis of Zn(2-methylimidazolate) ₂ , ZIF8-NP	11
4.3	Synthesis of Zn(2-formylimidazolate) ₂ , ZIF-90-CHO	13

4.4	Synthesis of ZIF-90-CHO-NP	15
4.5	Synthesis of ZIF-90-NH ₂	17
4.6	Synthesis of ZIF-90-NH ₂ -NP	20
4.7	Synthesis of ZIF-90-COOH.....	21
4.8	Synthesis of MAF-66.....	23
5	Screening of Pd deposition on ZIF-8 using various ionic liquids.....	26
6	Synthesis of MNP-on-ZIFs.....	33
	<i>Notes on the sample-naming conventions for NP-on-MOF composites</i>	34
	<i>Summary on the synthesis and properties of NP-on-MOF composites</i>	35
6.1	Pd-on-ZIF8-NP, Pd-on-ZIF-90-NH ₂ , Pd-on-ZIF90NH ₂ -NP, Pd-on-MAF66.....	37
6.2	Fe ₃ O ₄ -on-ZIF-8-NP, Fe ₃ O ₄ -on-ZIF90NH ₂ , and Fe ₃ O ₄ -on-ZIF90NH ₂ -NP	46
6.3	Pd/Fe ₃ O ₄ -on-ZIF8-NPs, Pd/Fe ₃ O ₄ -on-ZIF90NH ₂ , Pd/ Fe ₃ O ₄ -on-ZIF90NH ₂ -NP and Pd/Fe ₃ O ₄ -on-MAF-66	56
6.4	Fe ₃ O ₄ -/Pd-on-ZIF8-NPs and Fe ₃ O ₄ -/Pd-on-ZIF-90-NH ₂ -NP	77
6.5	Pd(PPh ₃) ₄ as a precursor in the attempted synthesis of Pd-on-ZIF-8.....	87
6.6	Rh deposition on ZIF-8-NP and ZIF-90-NH ₂	88
7	Pd-on-MOF nanocomposites as catalysts	90
7.1	Reduction of 4-nitrophenol to 4-aminophenol	90
7.2	Hydrogenation of cyclohexene.....	122
8	References	125

1 Analytics

AAS

Atomic Absorption Spectroscopy (AAS) was carried out using *PinAAcle 900T* instrument (Perkin Elmer) using an acetylene-air flame ionization.

Gas adsorption

N₂ gas adsorption isotherms were collected using the *Quantachrome Nova 4000e* (Quantachrome Instruments) automatic gas sorption analyzer at 77 K. The used gases (He, N₂) were of ultra-high purity (UHP, 99.999% or better) and the STP volumes are given according to the NIST standards (293.15 K, 101.325 kPa). Helium gas was used for the determination of the cold and warm free space of the sample tubes. The samples (11-25 mg) were activated immediately prior to the measurement at 100-140 °C for 2-12 h at 10⁻³ mbar vacuum.

Elemental analysis

CHN elemental analysis, only for MOF supports, was performed on a *Vario Micro Cube* (Elementar).

ESI-MS

ESI-MS spectra were acquired on a *Maxis 4G* quadrupole time-of-flight mass spectrometer (Bruker Corporation) with ionization voltage of 4 kV and the operating temperature of the inlet capillary of 180 °C.

IC

Ion chromatography (IC) was performed on a *Dionex ICS-1100* using IonPac™ AS22-Fast-4 μm columns (0.4 mm diameter, 150 mm length).

IR

FT-IR measurements were collected on samples dispersed in KBr pellets using a *Bruker Tensor 37* system in the 4000-400 cm⁻¹ range with a 2 cm⁻¹ resolution.

Karl-Fischer-titration

The water content was determined by Karl-Fischer-titration (KFT) using a *ECH / Analytik Jena Karl-Fischer-Titrator AQUA 40.00* instrument.

NMR

¹H, ¹³C and ¹⁹F NMR spectra were measured using a *Avance III-300 (300 MHz)* and *Avance III-600 (600 MHz)* instruments (Bruker Corporation) at 298 K. The characteristic solvent signals were

used as references (CDCl_3 : ^1H δ 7.26 s, ^{13}C δ 77.16 t; C_6D_6 ^1H δ 7.16 s, ^{13}C δ 128.1 t; D_2O ^1H δ 4.8 s instrument).

PXRD

Powder X-ray diffraction patterns (PXRD) were recorded by a *Bruker D2 Phaser* (0.02° formal angular resolution) diffractometer in reflective mode using a flat low-background silicon sample-holder (optionally with a protective dome, see below). The diffractometer was equipped with a Bragg-Brentano goniometer, graphite monochromator ($\text{Cu K}\alpha$, $\lambda = 1.5418 \text{ \AA}$), and Lynxeye 1D detector. The measurements were performed at room temperature with 0.02-0.05° steps under rotation at ~5 rpm. The $2\theta < 6^\circ$ area was not recorded due to the scattering of the primary beam, which strongly affected the background. The obtained patterns were not processed further, i.e. no background subtraction, smoothing, etc. were used.

All samples were measured in air (the identity of Fe_3O_4 -deposited species, synthesized under inert conditions could have been doubted, but the unchanged ferromagnetism upon exposure to air, the SAED measurements on samples with minimal air exposure, and the general chemical logic pointed out that the actual Fe_3O_4 -species are Fe_3O_4 . Hence no further precautions after initial attempts to use protective type/dome were further taken).

Due to the low amount of the samples and the decreased diffraction intensities of the nanoparticulated materials, the divergence slit was set to a considerably large value of 1 mm. The larger size of the divergence slit improved the efficiency but introduced significant additional line broadening convoluted with the line broadening associated with nanoparticulation.

The determination of the particle sizes according to the Scherrer equation, performed for selected cases, was based on the use of a microparticulated LaB_6 standard, collected under the same measurement conditions. The deconvolution of the instrumental peak broadening using the data on the LaB_6 standard was performed by the "Match!" Software [1].

SEM and SEM-based EDX element mapping

The samples for the scanning electron microscopy (SEM) were gold-coated using a *JEOL JFC 1200* fine-coater. SEM images were collected using a *JEOL JSM-6510LV QSEM* electron microscope (JEOL GmbH) with a LaB_6 cathode, equipped with a *Bruker Xflash 410* silicon drift detector with a capability to perform energy dispersive X-ray spectroscopy (EDX), including EDX-mapping. The latter was evaluated using the Bruker ESPRIT software.

TGA

Thermogravimetric analysis (TGA) was performed with a *Netzsch TG 209 F3 Tarsus* instrument (Netzsch Group) using an aluminum crucible at a 5 K min^{-1} heating rate.

TEM, STEM, TEM-based EDX mapping, and SAED

The measurements were performed on a JEM-2200 FS transmission electron microscope (*JEOL* 200 kV, $\sim 7.5 \text{ nA max.}$, 0-40 keV energy range of electrons), T3 PHA mode, or on a LEO912 transmission electron microscope (*Zeiss*; 120 kV) instrument, both equipped by an in-column 'Omega' energy filter.

A typical sample was prepared as follows: $\sim 0.01 \mu\text{L}$ of the IL dispersion was diluted by 1 mL acetonitrile, and a small amount of the thoroughly mixed diluted dispersion was immediately transferred to the TEM carbon-coated copper grids (CF200-Cu Mesh) *via* drop-casting. The drop on the grid was allowed to evaporate (up to 30 minutes), followed by accurate washing of the grid 5-10 mL acetonitrile concluded with a final drying.

The transmission electron microscopy- (TEM) images were collected using a FEI Tecnai G2 F20 electron microscope operated at 200 kV accelerating voltage and a Philips CM20 electron microscope operated at 200 kV accelerating voltage. The TEM-based average particle size was derived from a set of values (distribution), measured manually on the micrographs using the bundled- or *Gatan Digital Micrograph* software. Generally, at least ~ 50 particles were measured, often using multiple micrographs from different areas of the same sample. The size is given in the form $\langle d \rangle \pm \sigma$, where $\langle d \rangle$ is the average (mean) of the longest projection of the particle's image and σ is the variance (uncorrected sample standard deviation).

The SAED (selected area diffraction) was measured on the same samples and instrument as the TEM images. The radii of the diffraction rings were measured and converted to the corresponding d-spacing-values and, finally, to the *hkl* values corresponding to a given material using the *Digital Micrograph* software.

UV-Vis spectroscopy

The spectra in the range of 200-600 nm were collected on a Shimadzu UV-2400PC (Shimadzu Corporation) UV-Vis spectrophotometer. Polystyrene cuvettes (Sarstedt AG & Co. KG;), 10 x 4 x 45 mm, with a light beam path length of $l = 10 \text{ mm}$, were used. The spectra were collected with 0.5 nm spectral sampling rate (*cf.* with the 5 nm spectral bandwidth at FWHM of the beam).

2 Non-analytical instrumentation

Centrifugation

The centrifugation was performed using a Beckman Coulter Allegra 64R centrifuge (max. 10 000 rpm corresponding to 10 730 g acceleration) or the Hettich Rotina 4605 (max. 11 000 rpm, 13 800 g) or Hettich EBA 8S (max. 18 000 rpm, ~2850 g). If the centrifugation parameters are not given low-to-medium rotation speeds, corresponding to ~1000 g, were used for the MNP-on-MOF composites, which was sufficient to centrifuge out the larger composite particles, but generally not enough to centrifuge out the non-deposited small (~5-20 nm) metal nanoparticles

MW-assisted syntheses

The microwave-assisted syntheses (MW-syntheses) were performed in Discover CEM microwave synthesizer system, equipped with power/temperature/time control, magnetic stirring, and automatic overpressure venting. The reactions were performed in sealed 10 ml pressure vessels, $d = 20$ mm (the tube was charged by the reactants and sealed under Ar atmosphere by aluminum crimp cap with PTFE lined butyl rubber septum).

2.1 Chemicals and materials

The chemicals used in this work (general chemicals are listed in Table S1 and the ionic liquids in Table S3), were used as received except the cases explicitly stated in the subscripts to the tables or in the synthetic description.

Table S1. List of chemicals used in this work (except ionic liquids).

Chemical	Abbreviation	Formula	Vendor	CAS No.	Purity, %
Acetonitrile ^[b]	CH ₃ CN	CH ₃ CN	Sigma-Aldrich	75-05-8	99.9%
Active carbon		C	Merck	7440-44-0	-
Aluminum oxide (acidic)		Al ₂ O ₃	Alfa Aesar	1344-28-1	-
4-Aminophenol		C ₆ H ₇ NO	Alfa Aesar	123-30-8	98.0 %
3-Amino-1,2,4-triazole	aTz	C ₂ H ₄ N ₄	TCI	61-82-5	> 98.0%
Ammonium, 25% aq. sol		NH ₃	VWR Chemicals	1336-21-6	31.3% (content)
Benzimidazole	blm	C ₇ H ₆ N ₂	Sigma-Aldrich	51-17-2	98 %
2-Imidazole-carboxaldehyde	OHC-Im		Sigma-Aldrich	10111-08-7	97%
1-Chlorobutane ^[c]		C ₄ H ₉ Cl	Sigma-Aldrich	109-69-3	99.5%
Dichloromethane		CH ₂ Cl ₂	Sigma-Aldrich	75-09-2	≥ 99.9%
Ethanol, anhydrous		C ₂ H ₅ OH	TH Geyer / Riedel -de Haën	64-17-5	99.9%
Ethylacetate	EtOAc	CH ₃ COOC ₂ H ₅	Fischer Chemicals	141-78-6	99.9%

Ethylenediamine		NH ₂ CH ₂ CH ₂ NH ₂	VWR Chemicals	107-15-3	99%
Iron AAS standards		Fe	Sigma-Aldrich	-	-
Iron carbonyl		Fe ₂ (CO) ₉	Sigma-Aldrich	15321-51-4	98%
Lithium bis(trifluoromethylsulfonyl)-imide		C ₂ F ₆ LiNO ₄ S ₂	ABCR	90076-65-6	99%
Methanol	MeOH	CH ₃ OH	VWR Chemicals	67-56-1	≥99.8%
1-Methylimidazole ^[c]		C ₄ H ₆ N ₂	Fluorochem	616-47-7	99%
2-Methylimidazole	mIm	C ₄ H ₆ N ₂	Merck	693-98-1	99%
Molecular sieves(4 Å)		-	VWR Chemicals	70955-01-0	-
4-Nitrophenol		C ₆ H ₅ NO ₃	Carbolution Chemicals GmbH	100-02-7	99 %
N,N-Dimethylformamide	DMF	C ₃ H ₇ NO	Sigma-Aldrich	68-12-2	≥ 99.8%
Palladium on carbon (10% _{wt})	Pd/C		Merck Schuchardt OHG, Art.-Nr.: 807104, surf. area 900-950 m ² g ⁻¹ , V _{por. tot} = 0.9-1.2 m ² g ⁻¹		
Palladium(II)-chloride ^[a]		PdCl ₂	Degussa	7647-10-1	99. %
Palladium, iron AAS standard		Pd, Fe	Sigma-Aldrich	-	-
Polyvinylpyrrolidone, PVP (av. mol. weight 40 kDa)		(C ₆ H ₉ NO) _n	Sigma-Aldrich	9003-39-8	-
2-Propanol	iPrOH				
Silver nitrate		AgNO ₃	Strem chemicals	7761-88-8	99.9%
Sodium borohydride, powdered		NaBH ₄	AppliChem GmbH	16940-66-2	≥ 95%
Zinc acetate, dihydrate		Zn(OAc) ₂ · 2H ₂ O	Sigma-Aldrich	5970-45-6	≥98%
Zinc chloride		ZnCl ₂	Fluorochem	20427-58-1	98%
Zinc hydroxide		Zn(OH) ₂	Fluorochem	20427-58-1	98%
Zinc nitrate, hexahydrate		Zn(NO ₃) ₂ · 6H ₂ O	Sigma-Aldrich	10196-18-6	98%

^[a] Stored in a glovebox under Ar after first use.

^[b] Dried using MB-SPS 800 solvent purification system (MBraun company) prior to use.

^[c] Distilled and stored over 4A molecular sieves.

The molecular sieves were dried at 400 °C and <10⁻³ mbar vacuum and stored under inert gas. EtOAc, 1-methylimidazole, 1-chlorobutane were distilled prior to use. Acetonitrile was dried using the MB-SPS 800 (*Braun*) solvent purification system. The term “Millipore water” denotes water purified by a Millipore Water purification system, producing ultrapure water with a resistivity of 5-15 MΩ·cm at 25 °C. For further details see the synthetic descriptions below.

3 Synthesis of the primary ionic liquid, [BMIm](NTf₂)

3.1 Synthesis of 1-butyl-3-methylimidazolium chloride, [BMIm]Cl

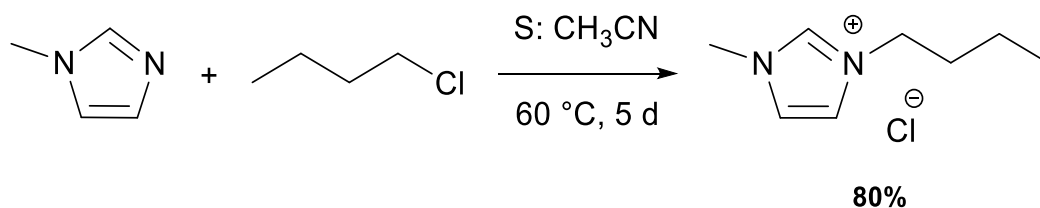


Fig. S1 Synthesis of [BMIm]Cl.

1-Methylimidazole (b.p. 60-65 °C, 5 mbar) 1-chlorobutane (78-79 °C, 1 bar), acetonitrile, and ethyl acetate were freshly distilled prior to the synthesis and additionally dried over 4A molecular sieves during a few days.

A 1L three-neck round-bottom flask equipped with a condenser was sequentially charged under nitrogen by 70 ml of dry acetonitrile, 125 ml of 1-methylimidazole (1.48 mol), and 162.5 ml of 1-chlorobutane (1.98 mol, 1.3 excess). The mixture was stirred during 5 days at 60 °C under inert conditions. The obtained light-yellow viscous liquid was concentrated and finally dried under vacuum (10⁻³ mbar) at 60 °C for app. 4 hours. Towards the end of the drying procedure, the oil crystallized to yield an almost white solid.

The crude product was dissolved in 150 ml of dry acetonitrile and the solution was added dropwise (2-4 drops sec⁻¹) to 700 ml of cold (~10 °C) ethyl acetate. The solution was preliminary seeded with a small amount of the crude crystalline product and the addition was performed under stirring using an efficient mechanical stirrer (150 rpm). The pure product precipitated as a white solid composed of small crystals. The supernatant was removed by overhead suction under inert gas, washed with 3×200 ml of cold ethyl acetate, and dried in vacuum (up to ~10⁻⁶ mbar, turbomolecular pump vacuum) for 5 days. Yield: 275.7 g (~80%, based on 1-methylimidazole).

Analyticals

¹H NMR (D₂O, 300 MHz) δ [ppm]: 0.80 (t, 3H), 1.25 (m, 2H), 1.80 (m, 2H), 3.80 (s, 3H), 4.15 (t, 2H), 4.75 (s, 2H), 7.40 (s, 1H).

¹³C-NMR (D₂O, 75 MHz) δ [ppm]: 12.5, 18.6, 31.2, 35.5, 49.2, 122.1, 123.3, 135.0 (possible overlaps).

IR (ATR) cm⁻¹: 3151, 3090, 2965, 2950, 2872, 1560, 1466, 1433, 1387, 1336, 1163.

ESI-MS: 139.2 (M⁺).

3.2 Synthesis of 1-butyl-3-methylimidazolium bistriflimidate, [BMIm](NTf₂)

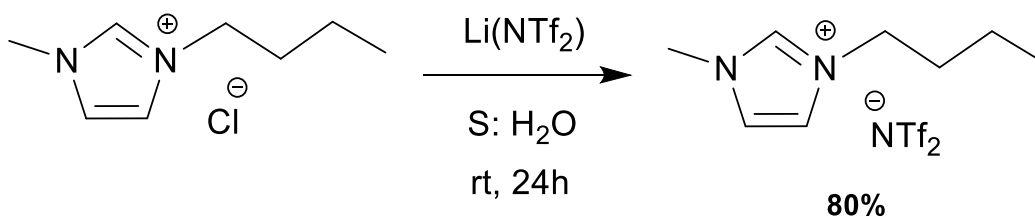


Fig. S2 Synthesis of [BMIm](NTf₂)

50.0 g (0.29 mol) of 1-butyl-3-methylimidazolium chloride and 82.2 g (0.29 mol) of Li(NTf₂) were dissolved in 25 ml of “Millipore water” and the formed solution stirred for 24 h. The solution was extracted by CH₂Cl₂ (3 × 50 ml) and the organic layer was washed by “Millipore water” (15 × 50 ml) until a negative test for chloride ions by a silver nitrate test. The dichloromethane was concentrated using a rotation evaporator at normal and then at reduced pressure (40 °C, 240 mbar). The liquid residue was slightly diluted by CH₂Cl₂ in order to decrease the viscosity and stirred with active coal overnight. The product was filtered through a column with acidic alumina (4-5 cm) applying N₂ pressurization of the column. The column was washed by dichloromethane and the combined filtrates were concentrated under reduced pressure. The obtained colorless viscous oil was dried at 10⁻³ mbar and 70 °C during 5 days followed by drying at 1×10⁻⁶ mbar (turbomolecular pump) and 70 °C during 4 days. Yield: 89.4 g (~74 %).

Analytcs

¹H NMR (CDCl₃, 600 MHz) δ [ppm]: 0.89 (t); 1.29 (m); 1.78 (m); 3.87 (s); 4.10 (t); 7.23 (m); 8.67 (s).

¹³C-NMR (CDCl₃, 150 MHz) δ [ppm]: 13.2; 19.3; 31.9; 36.3; 50.0; 118.7; 122.2-123.2 (overlapping); 136.1

Water content (KFT): < 5 ppm.

IC based ion content [mg L⁻¹]: Br⁻ = 0.086 (0.11 %); Cl⁻ = 0.365 (0.46%); F⁻ = 0.057 (0.07%); PF₆⁻ = 1.495 (1.88); NTf₂⁻ = 77.5 (97.5%). Note: the source of the PF₆⁻ impurity is unidentified, and we believe that it is rather a measurement artefact caused by the electrode. In any case this impurity does not pose problems for the intended use of the synthesis of NPs.

4 Synthesis of MOF supports

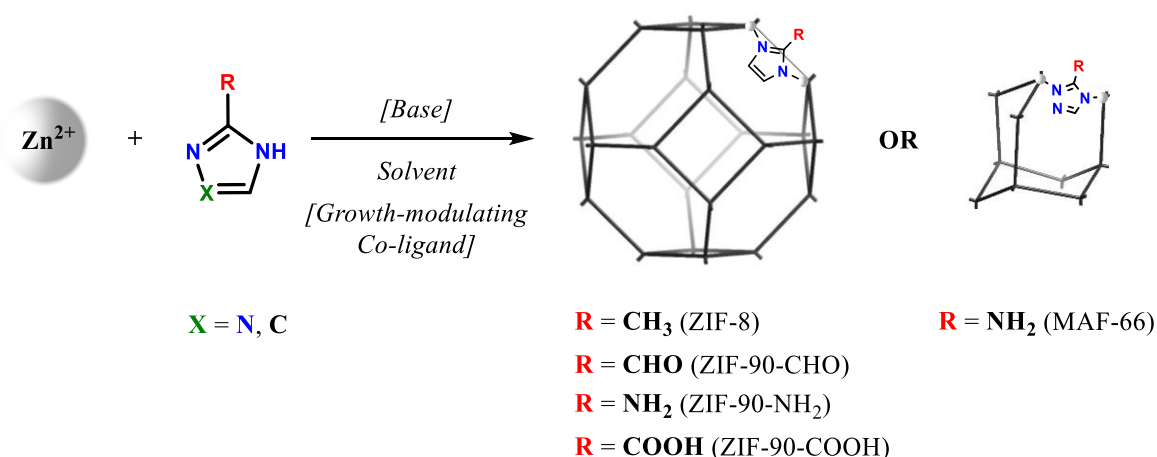


Fig. S3 General synthetic scheme from the MOF and MOFNP materials in this work.

4.1 Special methods

The addition of the solutions with an explicitly given addition rate (in ml h⁻¹), was performed by a programmable NE-1000 syringe pump (New Era Pump Systems). The washing of the nanoparticulated product was done *via* repeated washings by the indicated solvent, employing thorough redispersion at each washing cycle. The isolated dry products after drying were stored under argon atmosphere in a glovebox, if else is not indicated explicitly.

Summary on the properties of the MOF-supports

Table S2. Properties of the synthesized MOF-supports

Sample	Activation Conditions [K], [h]	S _{BET} , (N ₂) [m ² g ⁻¹]	SEM based average particle size, <d> ± σ ^{a)} [nm]	TEM based average particle size (given for NPs only), <d> ± σ ^{a)} [nm]	PXRD based (Scherrer equation) average crystallite size, <d> [nm]
ZIF8-NP	120, 3	1641	114±8	75±17	60
ZIF90-CHO	140, 12	1003	3662±1005	-	330
ZIF90-CHO-NP	140,12	~1100	110±20	-	127
ZIF90-NH ₂	140, 12	344	3461±581	-	980
ZIF90-NH ₂ -NP	140,12	~400	107±12	71±11	105
ZIF90-COOH	140, 12	1029	3592±874	-	211
MAF66	100, 2	1014	800±300	-	124

^{a)} <d>±σ, where <d> is the average size and σ is the variance. Note that the TEM-based data were collected only for the smaller particles, where the resolution advantage is strong (for those cases, where the TEM sizes are given, the SEM-based data are indicative).

4.2 Synthesis of Zn(2-methylimidazolate)₂, ZIF8-NP

1.85 g (6.17 mmol) of Zn(NO₃)₂ · 6H₂O was dissolved in 125 ml of methanol at room temperature in a 500 ml Erlenmeyer flask. A second solution of 2.03 g (24.6 mmol) of 2-methylimidazole in 125 ml methanol was added at once and stirred for a few minutes. The closed vessel was left standing for 24 h, meanwhile the colorless solution turned turbid. The suspension was centrifuged, and the sediment was washed by 3×50 ml MeOH. The white product ZIF-8-NP1, consisting of ZIF-8 nanocrystals was dried at 10⁻³ mbar at RT (= room temperature). Yield: 0.25 g (~27 %).

The synthesis is an adaptation of the method described in Cravillon et al. [2].

Analytcs

Elemental analysis for Zn(MeIm)₂, C₈H₁₀N₄Zn; calcd (%): C 42.22, H 4.43, N 24.62; found (%): C 41.53, H 4.32, N 24.37.

SEM (Fig. S4).

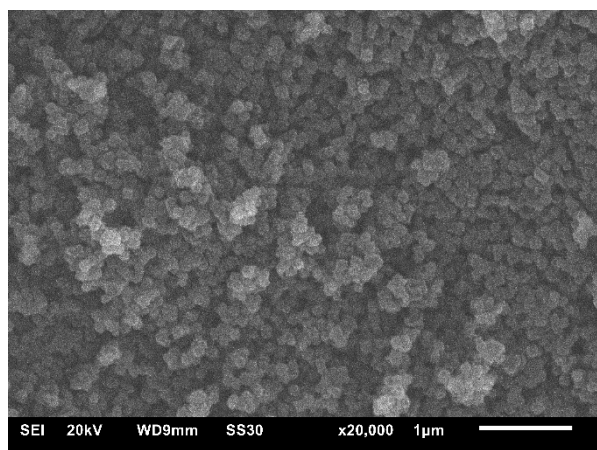


Fig. S4 SEM image of the ZIF-8-NP material (114±8 nm).

Surface area, N₂ adsorption isotherm based (Fig. S5) S_{BET}: 1641 m² g⁻¹ (lit.: 1696 [2]).

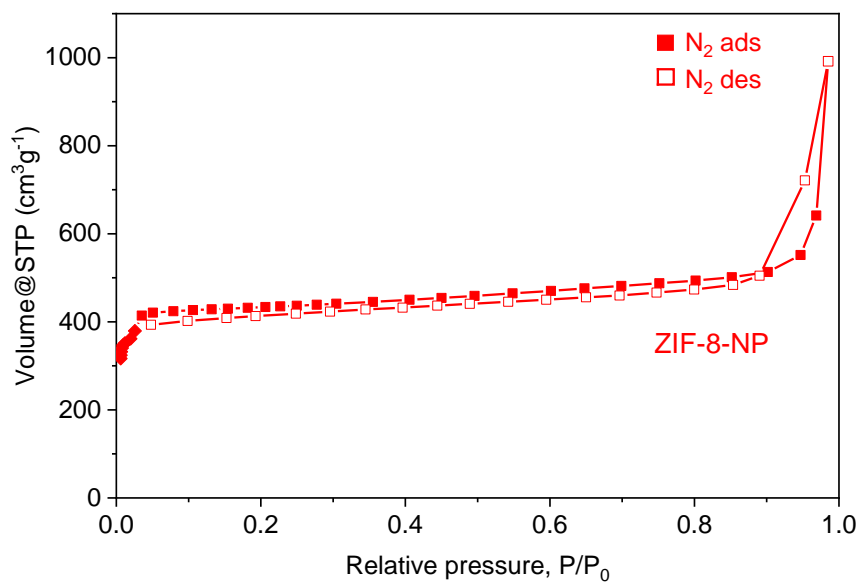


Fig. S5 N₂ gas adsorption isotherm for ZIF8-NP.

PXRD (Fig. S6): 60 nm average crystallite size according to the Scherrer equation.

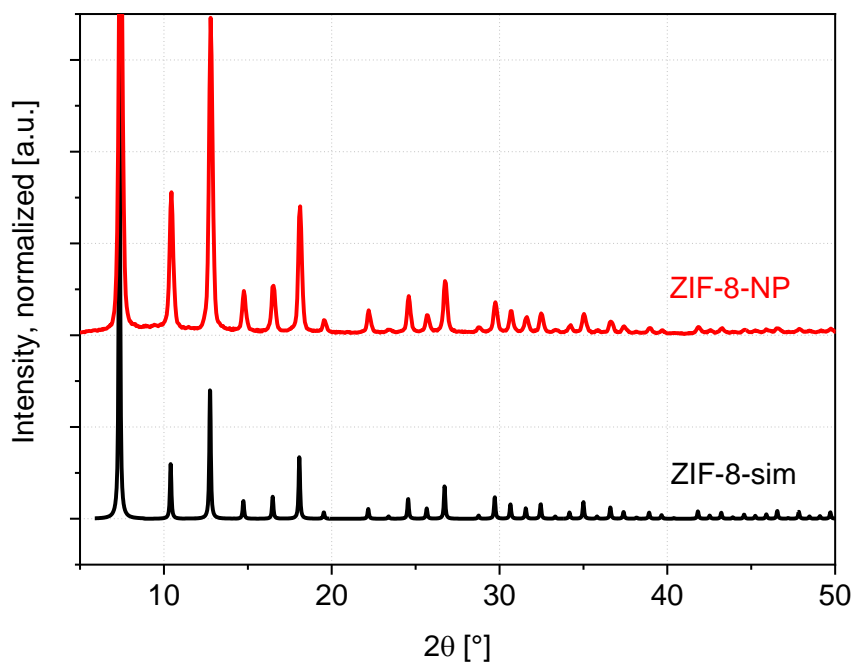


Fig. S6 Comparison of the simulated (ZIF-8-sim based on single-crystal XRD structure) and the experimental ZIF8-NP PXRD patterns.

TGA (Fig. S7).

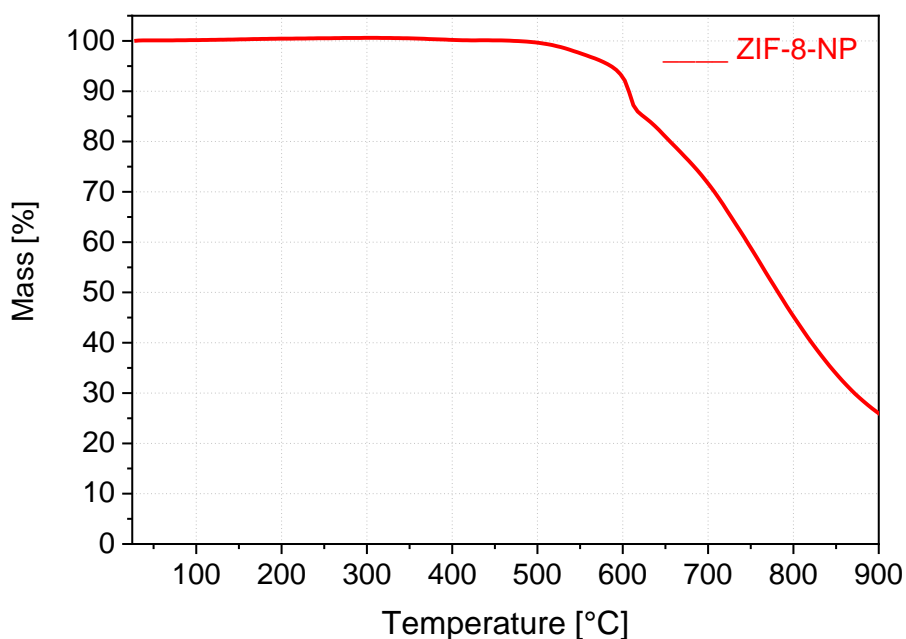


Fig. S7 TGA of the ZIF-8-NP.

4.3 Synthesis of Zn(2-formylimidazolate)₂, ZIF-90-CHO

A solution of 2.50 g of Zn(NO₃)₂ · 6H₂O was dissolved in 130 ml of tBuOH/H₂O, 1:1 by volume, was prepared in a 250 ml Erlenmeyer flask. The second solution was prepared by sequential dissolution of 3.20 g of 2-imidazolecarbaldehyde and 0.40 g PVP (40 kDa) in 130 ml of glycerol/water (1:1 by volume) in a 500 ml flask. The first solution was added to the second at once under intensive stirring and was stirred for a ~10 minutes to yield a slightly yellowish turbid solution. The solution was left to stay unmoved for 10 min, then centrifuged, followed by washing with 3×50 ml (150 ml) of MeOH and drying at 10⁻³ mbar and RT. The yield of the slightly yellowish product was 246 mg (~7.3%).

The synthesis is an adaptation of the method described in [3].

Analytcs

Elemental analysis for Zn(OHC-Im)₂, C₈H₆N₄O₂Zn; calcd (%): C 37.60, H 2.37, N 21.93; found (%): C 36.04, H 2.72, N 20.54.

SEM (Fig. S8).

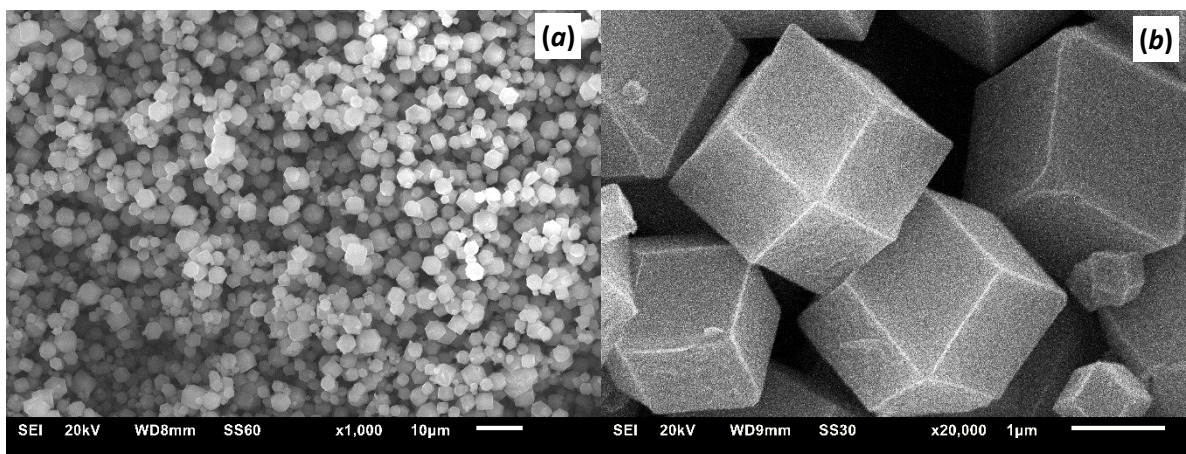


Fig. S8 SEM images of the ZIF-90-CHO material (4000 ± 1000 nm).

Surface area, N_2 adsorption isotherm based (Fig. S9) S_{BET} : $1003 \text{ m}^2 \text{ g}^{-1}$ (lit.: 897 [3]).

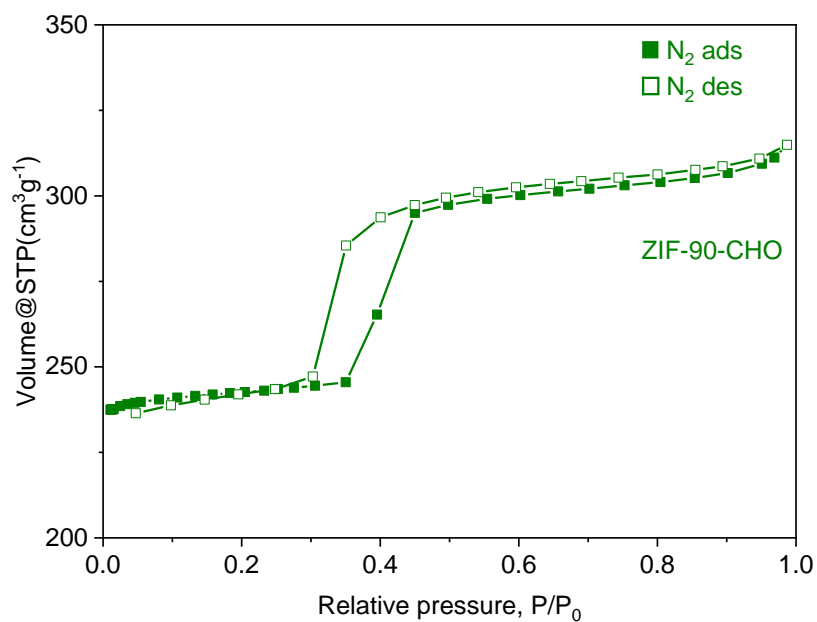


Fig. S9 N_2 gas adsorption isotherm for ZIF-90-CHO.

PXRD (Fig. S16): 330 nm average crystallite size according to the Scherrer equation.

TGA (Fig. S10).

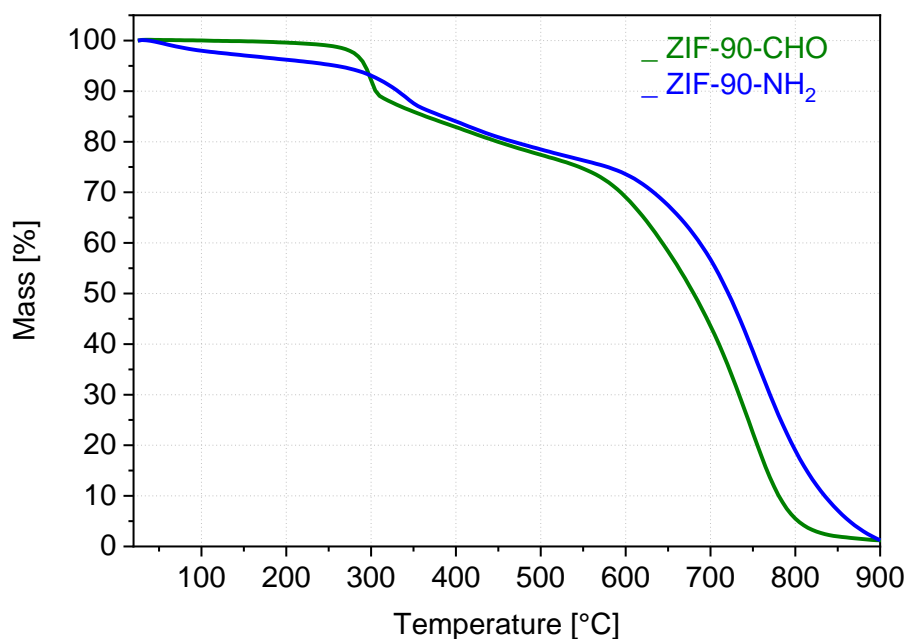


Fig. S10 TGA for ZIF-90-CHO and ZIF-90-NH₂ samples

4.4 Synthesis of ZIF-90-CHO-NP

1.76 g (18.3 mmol, ~3.4 excess) imidazole-2-carboxaldehyde was dissolved in warm (~60 °C) 105 ml of DMF to ensure complete dissolution. The solution cooled to RT was filtered through a 0.45 μm PTFE filter. The second solution, 500 mg (2.73 mmol) of Zn(OAc)₂·2H₂O in 105 ml of DMF, was added to the previous one at once at RT under intensive stirring. The formed turbid solution was stirred for a further 4 h at RT. The white product was centrifuged (30 min) and washed multiple times with DMF (3×50 ml total) followed by methanol (3×50 ml total). The product was dried at 10⁻³ mbar and RT. Yield: 366 mg (~62.7%).

The synthesis is an adaptation of the method described in [4].

Analytcs

Elemental analysis for Zn(OHC-Im)₂, C₈H₆N₄O₂Zn; calcd (%): C 37.60, H 2.37, N 21.93; found (%): C 33.50, H 3.33; N 19.03.

SEM (Fig. S11).

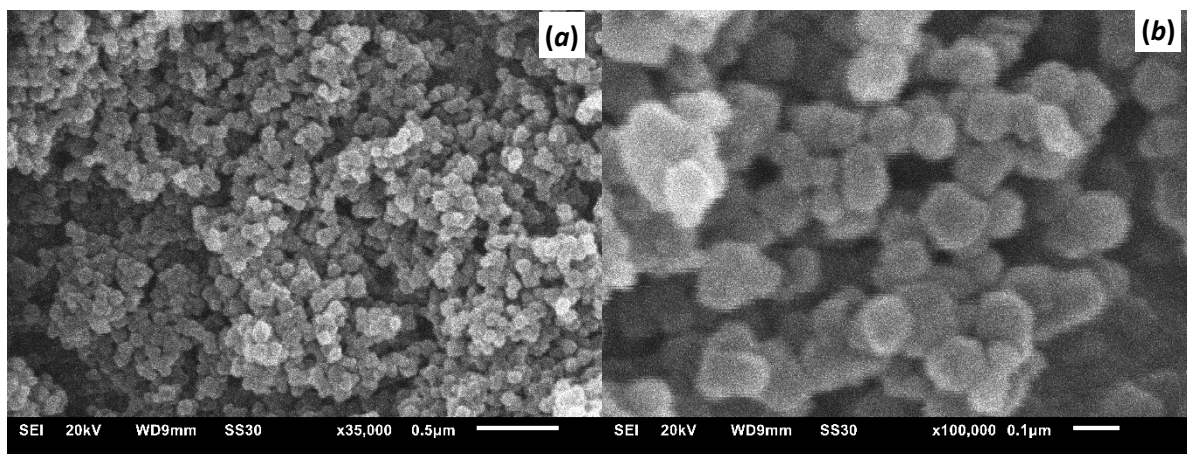


Fig. S11 SEM images for the ZIF-90-CHO-NP material (110 ± 20 nm).

Surface area, N_2 adsorption based (Fig. S15) S_{BET} : $1106 \text{ m}^2 \text{ g}^{-1}$ (lit.: 897 [4]).

PXRD (Fig. S12): 127 nm average crystallite size according to the Scherrer equation.

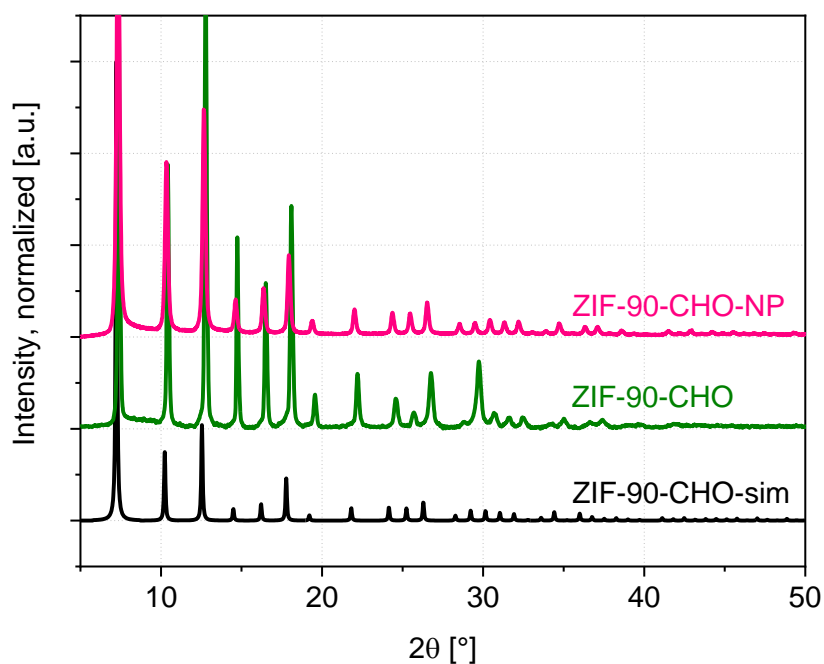


Fig. S12 Comparison of the simulated (ZIF-90-CHO-sim based on single-crystal XRD structure) and the experimental ZIF-90-CHO and ZIF90-CHO-NP patterns.

TGA (Fig. S13).

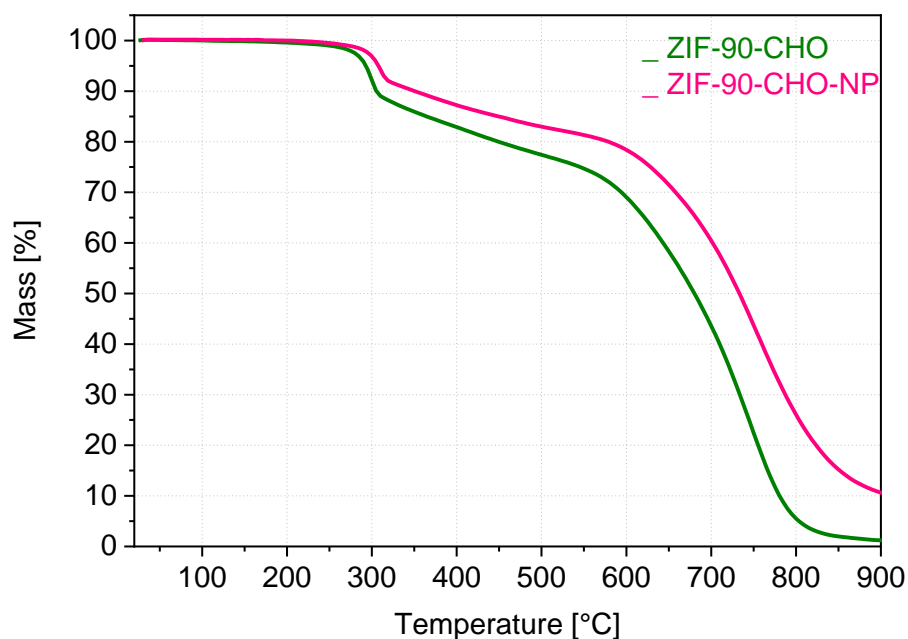


Fig. S13 TGA of the ZIF-90-CHO and ZIF-90-CHO-NP.

4.5 Synthesis of ZIF-90-NH₂

101.5 mg (0.40 mmol) ZIF-90-CHO was dispersed in 30 ml of dry methanol in a 100 ml flask. The dispersion was heated to 60 °C and 27.5 μ L (0.41 mmol) ethylenediamine (EDA) in 20 ml methanol was added dropwise (9 ml h⁻¹), under stirring. The reaction mixture was heated for the following 24 h at 60 °C under stirring. The formed yellowish turbid solution was centrifuged and the sediment was washed by 3 \times 50 ml of MeOH, followed by drying at 10⁻³ mbar and RT. The yield of the slightly yellowish product was 96.1 mg (~91 %).

The synthesis is an adaptation of the method described in [5].

Analytcs

Elemental analysis for Zn(ImCHNC₂H₄NH₂)₂, C₁₂H₁₈N₈Zn; calcd (%): C 42.43, H 5.34, N 32.99; found (%): C 39.89, H 4.20, N 27.18.

SEM (Fig. S14).

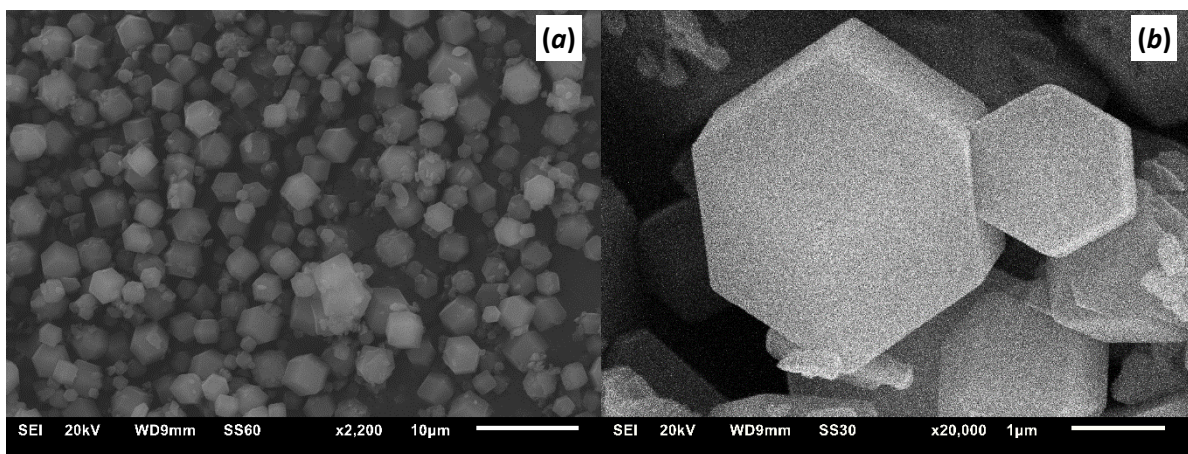


Fig. S14 SEM images of the ZIF-90-NH₂ material (3500±600 nm).

Surface area, N₂ adsorption isotherm based (Fig. S15) S_{BET} : 344 m² g⁻¹ (lit.: 536 [2]).

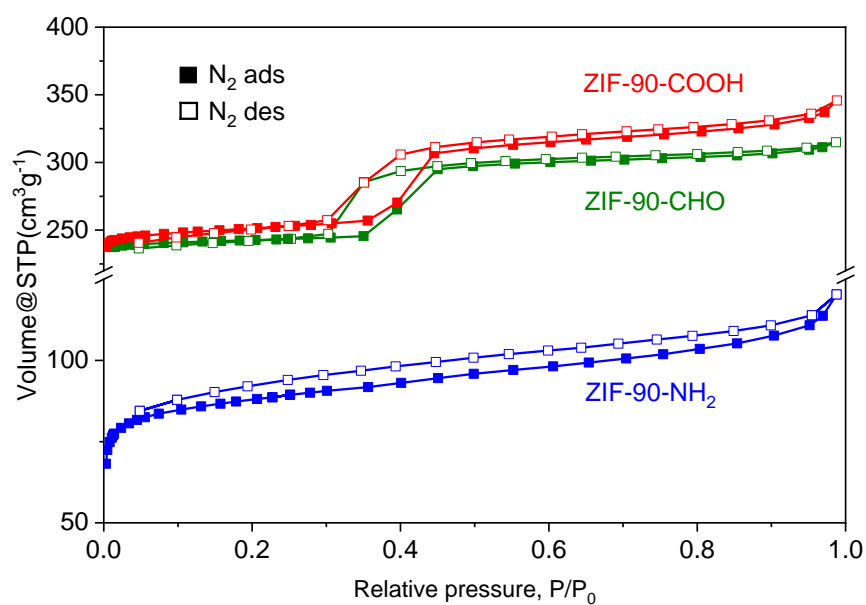


Fig. S15 Comparison of N₂ gas adsorption isotherms for ZIF-90-CHO, ZIF-90-COOH, ZIF-90-NH₂.

PXRD (Fig. S16): 980 nm average crystallite size according to the Scherrer equation.

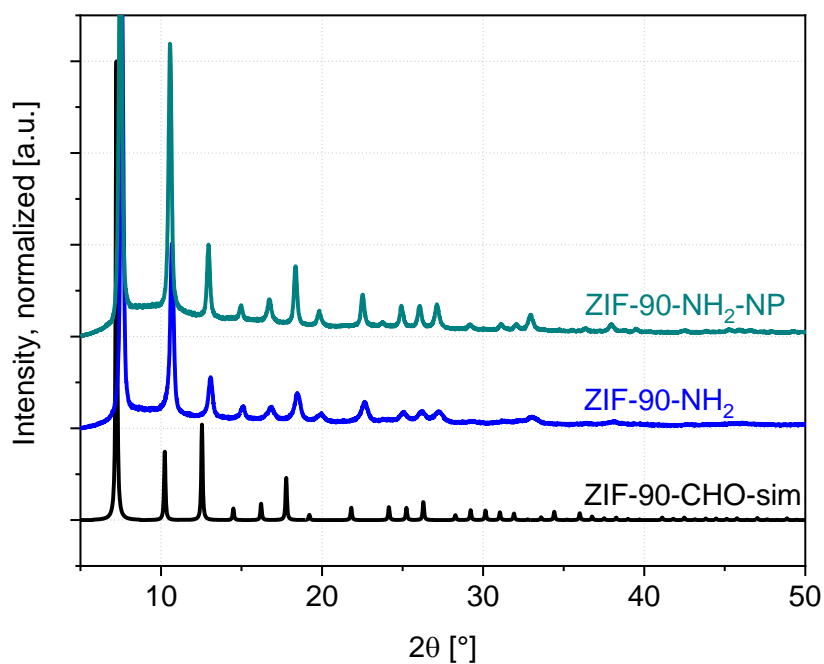


Fig. S16 Comparison of the PXR D patterns: the experimental ZIF-90-NH₂ and ZIF-90-NH₂-NP compared to the simulated ZIF-90-CHO (isostructural precursor) based on single-crystal XRD structure.

IR (Fig. S17).

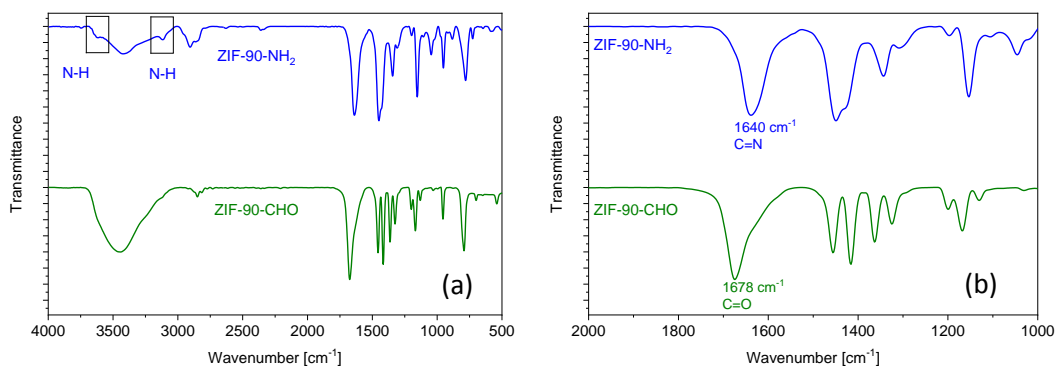


Fig. S17 Comparison of the IR (KBr) spectra for ZIF-90-CHO and ZIF-90-NH₂: (a) full spectrum and (b) expansion.

The differences between the characteristic $\nu(\text{C}=\text{O})$ stretching at 1678 cm^{-1} and $\nu(\text{C}=\text{N})$ stretching at 1640 cm^{-1} of the formyl- and imino groups respectively are well visible on (b).

The $\nu(\text{C}(\text{O})-\text{H})$ stretching of the formyl group at $\sim 2800\text{ cm}^{-1}$ is not distinguished enough from the broad $\nu(\text{C}-\text{H})$ stretching generated by the ethylene moiety in the $\sim 3000\text{-}2800\text{ cm}^{-1}$ region.

TGA (Fig S18).

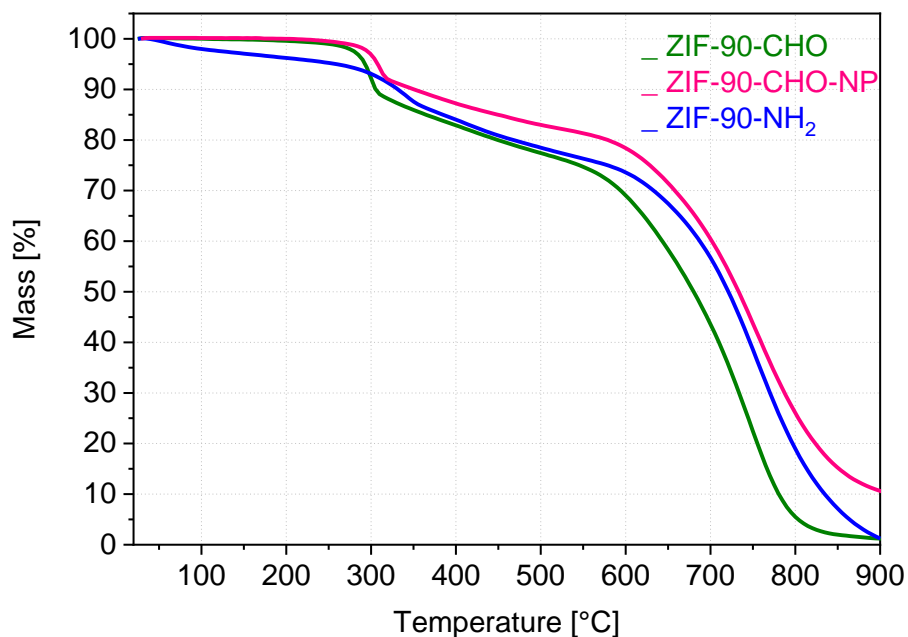


Fig. S18 Comparison of the TGA for ZIF-90-CHO, ZIF-90-CHO-NP, and ZIF-90-NH₂.

Note the similar TGA-based stability, with the decomposition onset at ~300 °C for ZIF-90-CHO and ~330 °C for ZIF-90-NH₂.

4.6 Synthesis of ZIF-90-NH₂-NP

To a stirred dispersion of 360.7 mg (1.42 mmol) of ZIF-90-CHO-NP in 107 ml MeOH at 60 °C a solution of 97.5 µl (1.45 mmol) EDA in 71 ml MeOH was added dropwise (9 ml h⁻¹). The solution was heated at 60 °C for an additional 24 h. The dispersion was centrifugated, isolated yellowish product washed by 3×50ml of MeOH, and dried at 10⁻³ mbar, room temperature. Yield: 352.4 mg (71 %).

The synthesis is an adaptation of the method described in [5].

Elemental analysis for Zn(ImCHNC₂H₄NH₂)₂, C₁₂H₁₈N₈Zn; calcd (%): C 42.43, H 5.34, N 32.99; found (%): C 39.29, H 3.70, N 26.68

SEM (Fig. S19).

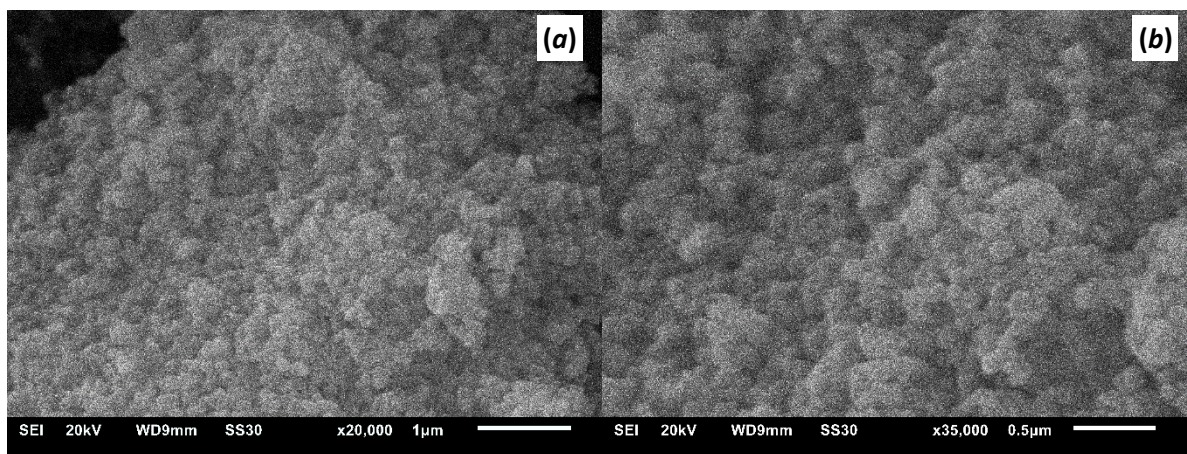


Fig. S19 SEM images of the ZIF-90-NH₂-NP material (110±12 nm).

PXRD (Fig. S20): 105 nm average crystallite size according to the Scherrer equation.

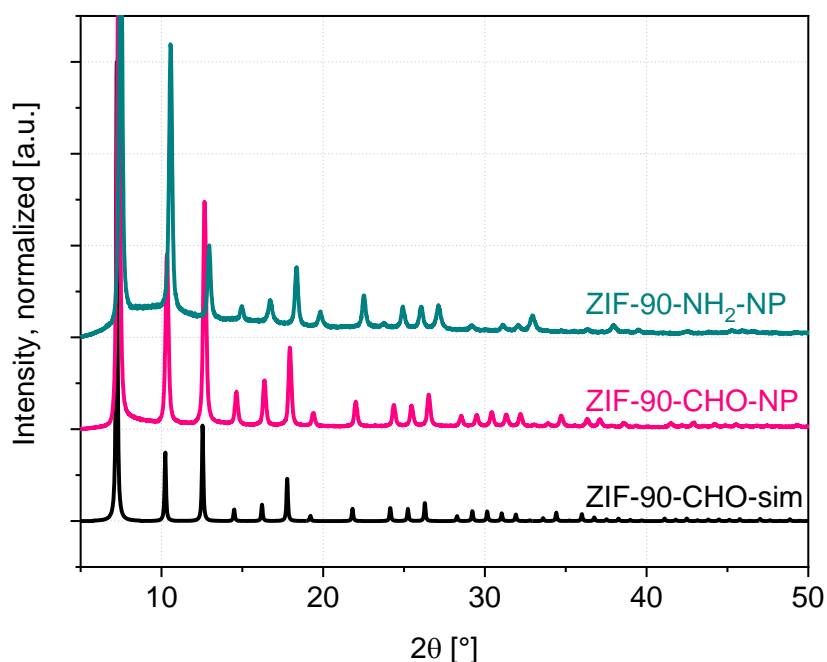


Fig. S20 Comparison of the PXRD patterns: the simulated (ZIF-90-sim based on single-crystal XRD structure) and the experimental ones for ZIF-90-CHO-NP and the derived ZIF-90-NH₂-NP.

4.7 Synthesis of ZIF-90-COOH

100 mg (0.39 mmol) of ZIF-90-St was dispersed in 30 ml of “Millipore water” in a 100 ml flask. 12.6 ml 35% H₂O₂ diluted in 20 ml, was added to the first solution dropwise (2 ml h⁻¹) under stirring, followed by 24 h of stirring (all procedures were performed at RT). The light yellowish turbid solution was centrifuged and washed thoroughly by 3×50 ml of methanol. The light-yellow product was dried at 10⁻³ mbar at RT. Yield: 50 mg (~44 %, significant losses during the washing procedures).

The synthesis is an adaptation of the method described in [5].

Analytcs

Elemental analysis for $\text{Zn}(\text{HOOC-Im})_2$, $\text{C}_8\text{H}_6\text{N}_4\text{O}_4\text{Zn}$; calcd (%): C 33.42, H 2.10, N 19.49; found (%): C 28.47, H 4.32, N 15.77.

SEM (Fig. S21).

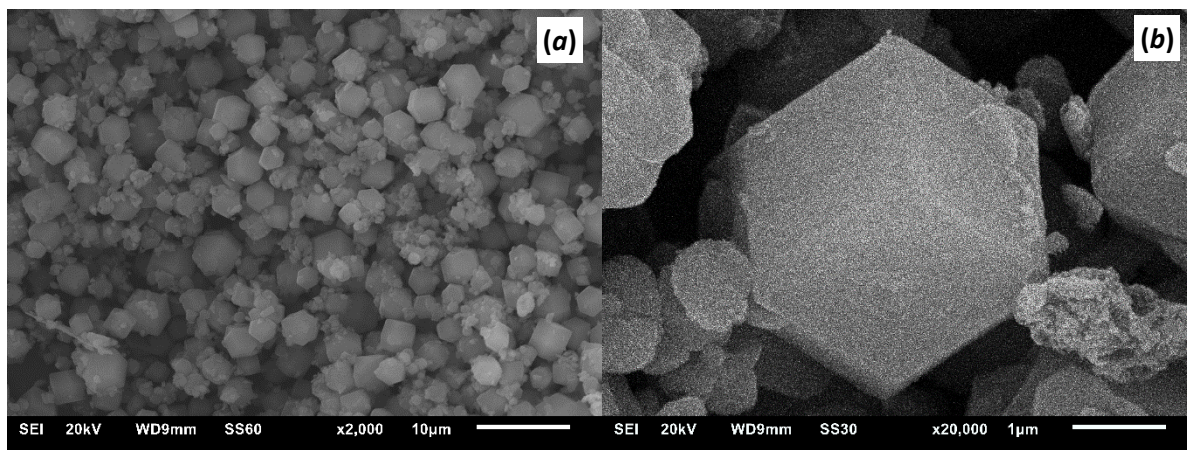


Fig. S21 SEM images of the ZIF-90-COOH material (3600 ± 900 nm).

Surface area, N_2 adsorption isotherm based (Fig. S22) S_{BET} : $1029 \text{ m}^2 \text{ g}^{-1}$ (lit.: 920 [5]).

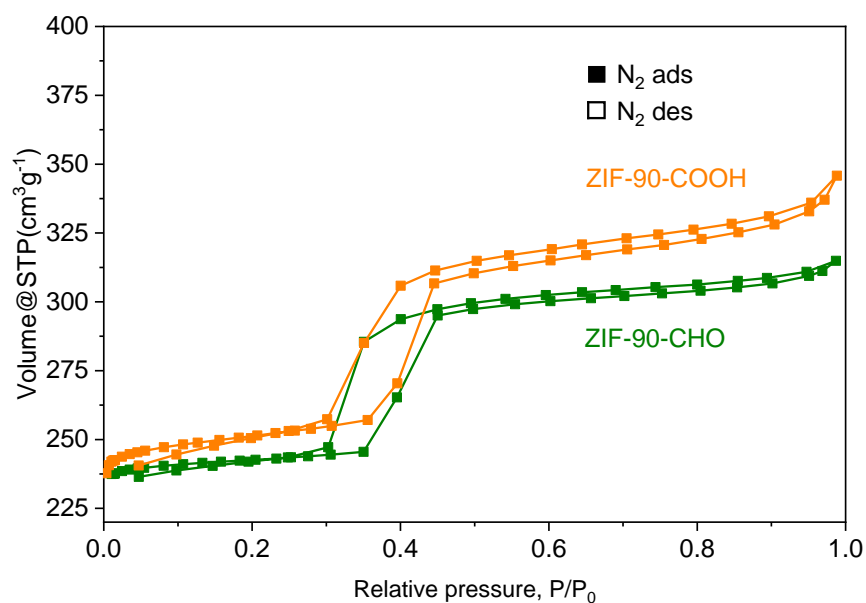


Fig. S22 Comparison of the N_2 gas adsorption isotherms for ZIF-90-CHO and the post-synthetically derived ZIF-90-COOH.

PXRD (Fig. S16): 211 nm average crystallite size according to the Scherrer equation.

TGA (Fig. S23).

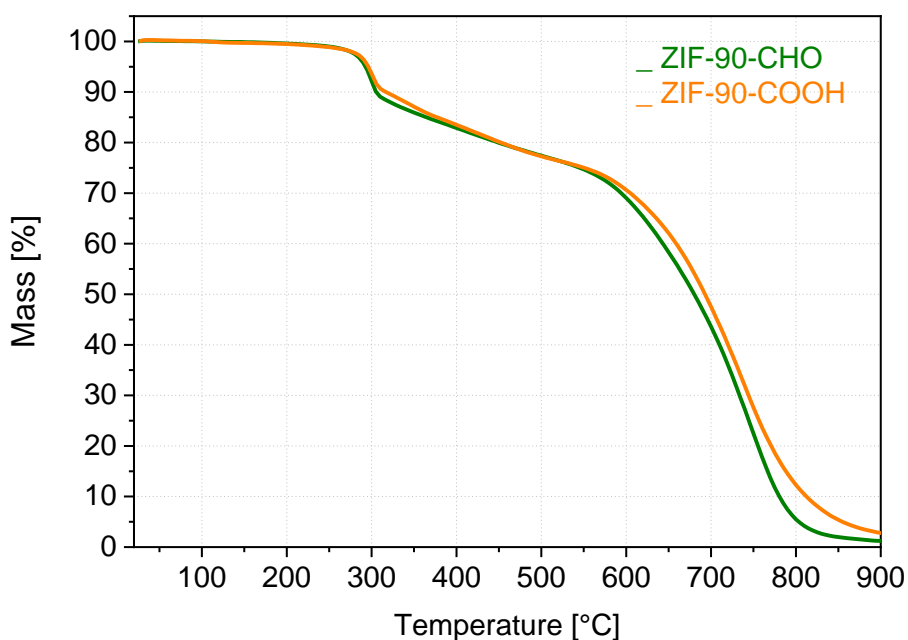


Fig. S23 TGA comparison for ZIF-90-CHO and ZIF-90-COOH.

4.8 Synthesis of MAF-66

Two solutions, 0.4 g (4.00 mmol) of $\text{Zn}(\text{OH})_2$ in 50 ml of conc. ammonia (~25%) and 3-amino-1,2,4-triazole in 50 ml of iPrOH were prepared at RT in Erlenmeyer flasks and subsequently cooled to ~10 °C. The second solution was added to the first one at once under intensive stirring and the combined solution was left for 5 minutes to stir, allowing the temperature to rise to near RT (~19 °C). The colorless turbid solution was centrifuged and washed 3×50 ml by “Millipore water” followed by 2×50 ml of 2-propanol. The fine white powder was dried at 10^{-3} mbar at RT. Yield: 0.76 g (~72%, based on $\text{Zn}(\text{OH})_2$; lit.: 85%).

The synthesis is an adaptation of the method described in [6].

Analytics

Elemental analysis for $[\text{Zn}(\text{3-atr})_2] \cdot 0.6 \text{ H}_2\text{O} \cdot \text{iPrOH}$, $\text{C}_7\text{H}_{15.2}\text{N}_8\text{O}_{1.6}\text{Zn}$; calcd (%): C 27.80, H 5.07; N 37.05; found (%): C 20.73; H 2.82; N 37.38.

SEM (Fig. S24).

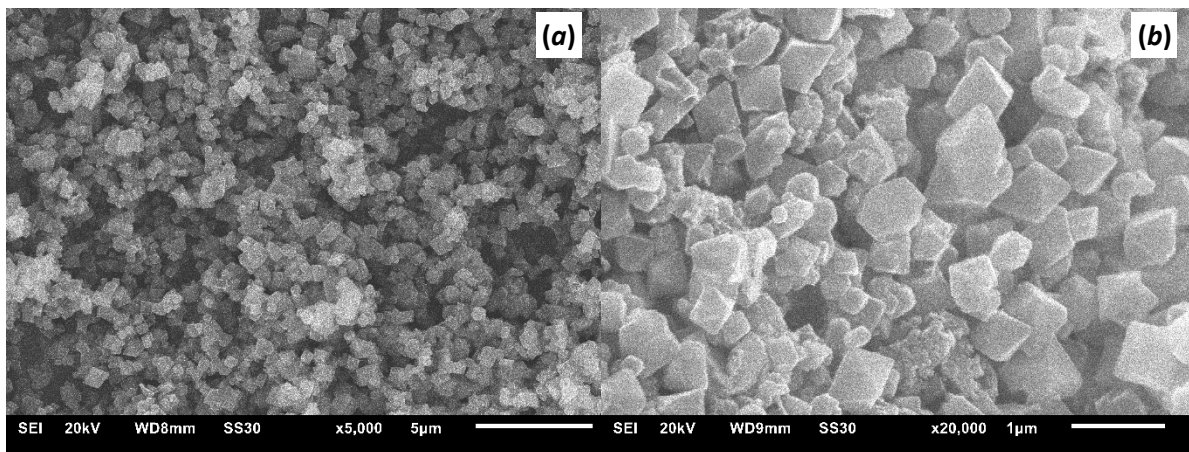


Fig. S24 SEM images of the MAF-66 material (800 ± 300 nm).

PXRD (Fig. S25): 124 nm average crystallite size according to the Scherrer equation.

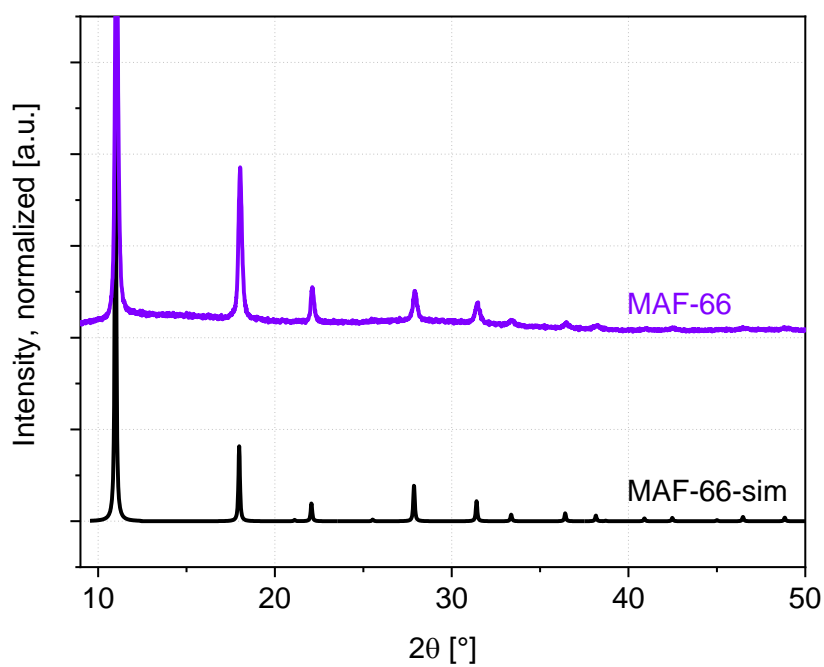


Fig. S25 The comparison of the experimental PXRD pattern of MAF-66 with the simulated MAF-66-sim, derived from the single crystal XRD structure, CSD code 860996, [6].

TGA (Fig. S26).

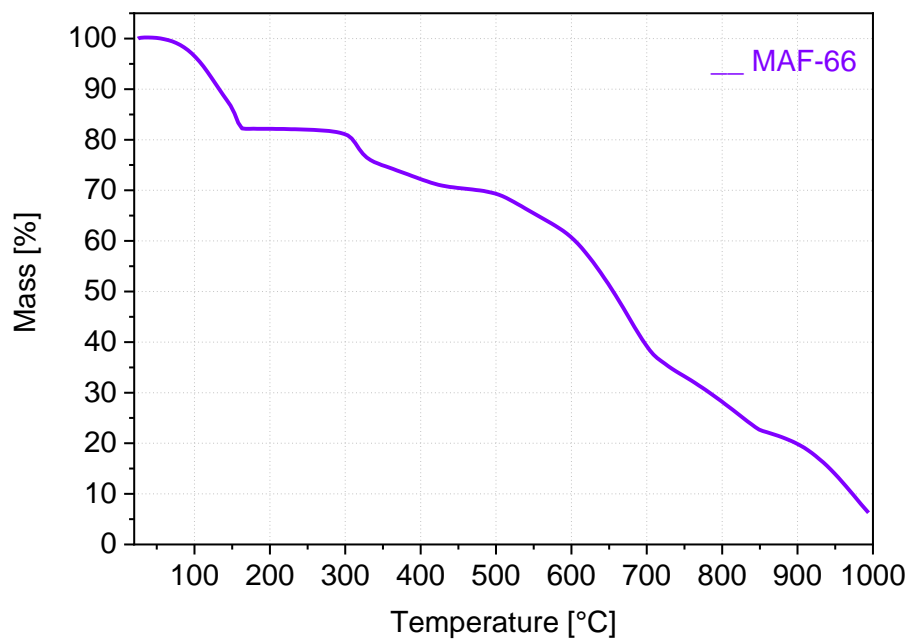


Fig. S26 TGA for the MAF-66 material [6].

5 Screening of Pd deposition on ZIF-8 using various ionic liquids

Table S3 Ionic liquids, used for screening of Pd deposition on ZIF-8.

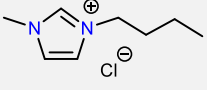
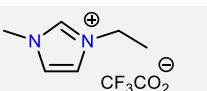
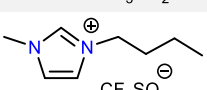
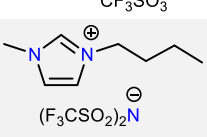
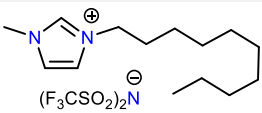
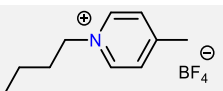
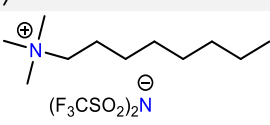
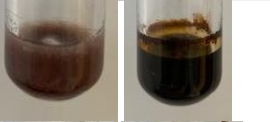
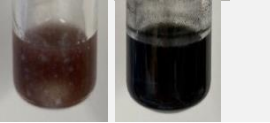
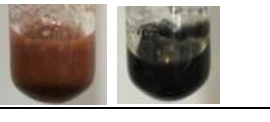
Ionic liquid (IL)	Abbreviation	Chemical formula	Vendor
1-Butyl-3-methylimidazolium-chloride	[BMIm]Cl		Iolitec
1-Butyl-3-methylimidazolium-tetrafluoroborate	[BMIm]BF ₄		Iolitec
1-Ethyl-3-methylimidazolium-trifluoroacetate	[EMIm]TFA		Iolitec
1-Butyl-3-methylimidazolium-triflate	[BMIm]OTf		Iolitec
1-Butyl-3-methylimidazolium-bis(trifluoromethylsulfonyl)imide	[BMIm]NTf ₂		- (Synthesized from [BMIm]Cl)
1-Decyl-3-methylimidazolium-bis(trifluoromethylsulfonyl)imide	[DMIm]NTf ₂		Abcr
1-Butyl-4-methylpyridinium-tetrafluoroborate	[BMPy]BF ₄		Iolitec
Trimethyloctylammonium-bis(trifluoromethylsulfonyl)imide	[TmOA]NTf ₂		Iolitec

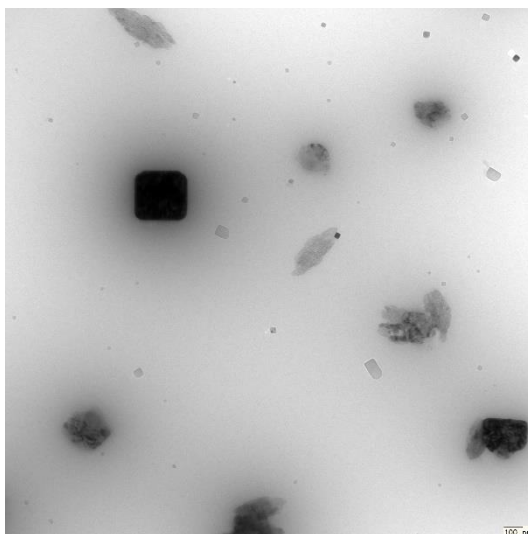
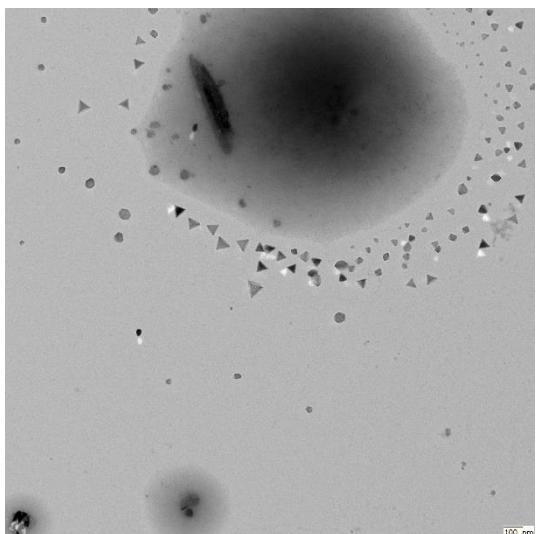
Table S4. Screening experiments on the deposition of Pd-on-ZIF-8.

Sample code	PdCl ₂ [mg]	ZIF8-NP [mg]	Ionic liquid, quantity [g]	Conditions	The synthetic medium before (left) and after the synthesis (right)
BMIm-Cl-P2	17.5	50.0	[BMIm]Cl 1.01	230°C, 3 min (20 W)	
BMIm-BF4-P2	17.0	51.2	[BMIm]BF ₄ 1.07	230°C, 3 min (20 W)	
EMIm-TFA-P2	17.2	51.0	[EMIm]TFA 1.03	230°C, 3 min (20 W)	
BMPy-BF4-P2	17.5	50.5	[BMPy]BF ₄ 0.53	230°C, 3 min (20 W)	
BMIm-OTf-P2	17.5	50.2	[BMIm]OTf 0.56	230°C, 3 min (20 W)	
DMIm-NTf2-P2	17.2	53.5	[DMIm]NTf ₂ 1.02	230°C, 3 min (20 W)	
TmOA-NTf2-P2	17.3	57.0	[TmOA]NTf ₂ 1.01	230°C, 3 min (20 W)	
Pd-on-ZIF8-NP	17.0	55.0	[BMIm]NTf ₂ 1.02	230°C, 3 min (20 W)	

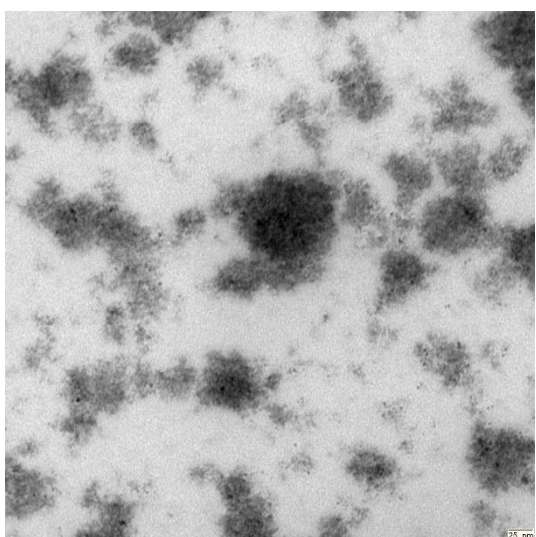
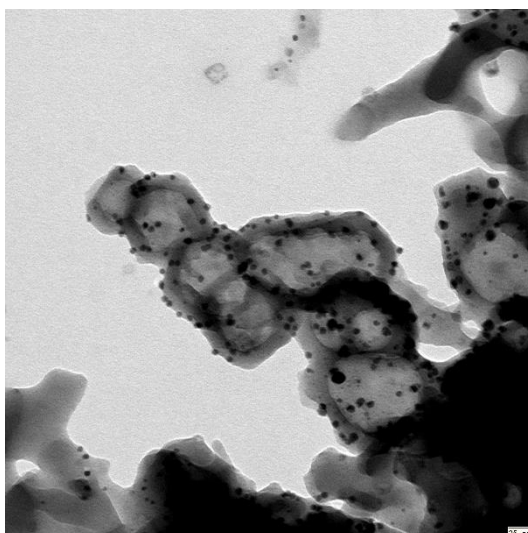
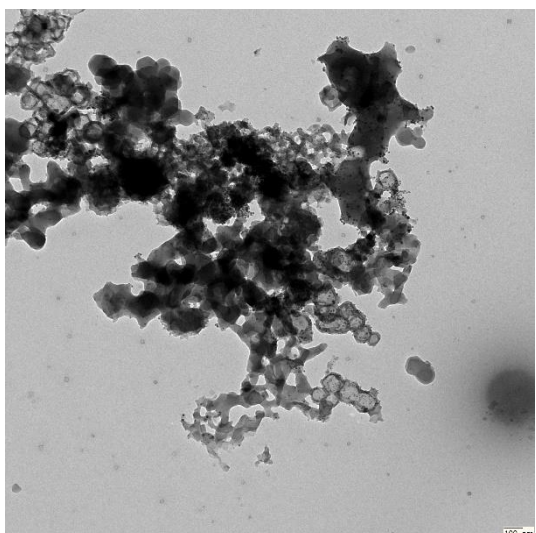
Standard synthesis (more details are given in the next chapter devoted to the synthesis of the composites in [BMIm]NTf₂): the 10 ml pressure MW-reactor tubes (further vessels) were charged with PdCl₂, ZIF-8-NP, and the respective ionic liquid (IL) under argon atmosphere in a glovebox. The pressure vessels were sealed and transferred to the MW reactor. The contents of the vessels were heated at 230 °C for 3 min under stirring. The formed suspension was diluted with 5 ml of acetonitrile, mixed, and centrifuged during 10 min (~1000 g). The supernatant was removed by a syringe and the residue was washed by 3×5 ml of acetonitrile (the addition and removal of the liquids were performed while the vessel was pressurized by nitrogen gas). The residue was dried under vacuum (10⁻³ mbar) at room temperature during one day and stored under inert atmosphere.

The TEM micrographs and the PXRD patterns of the screening products are shown in Fig. S27, S28 respectively.

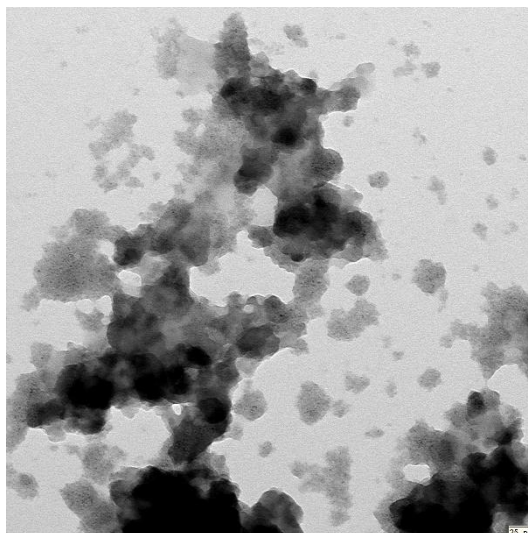
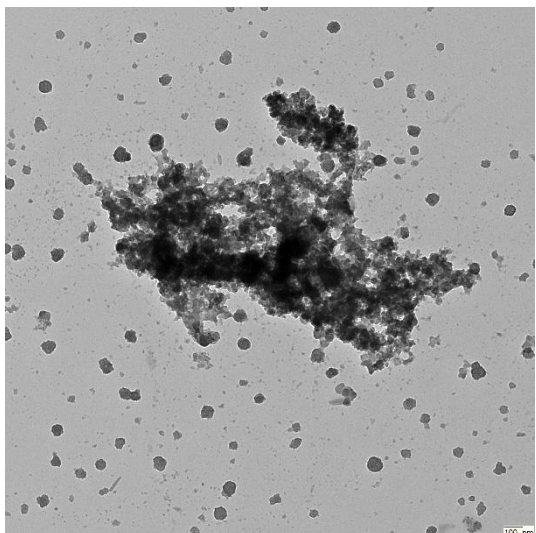
TEM BMIm-Cl-P2:



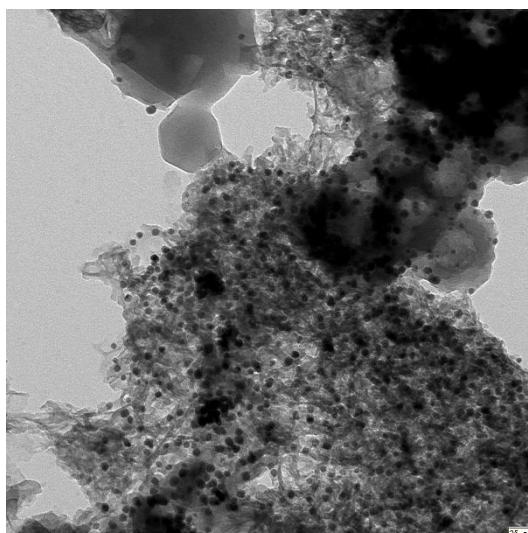
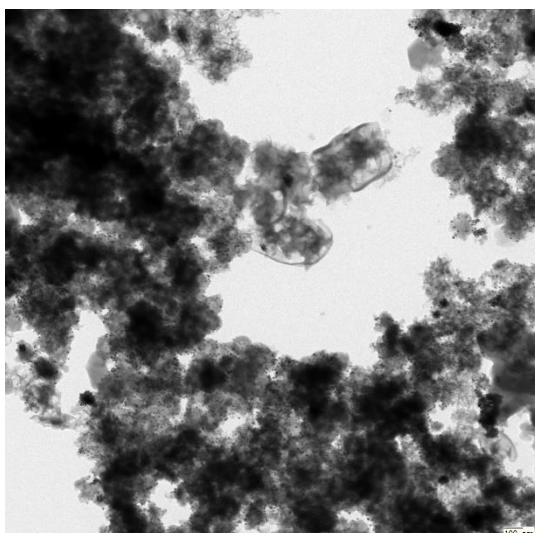
TEM BMIm-BF4-P2:



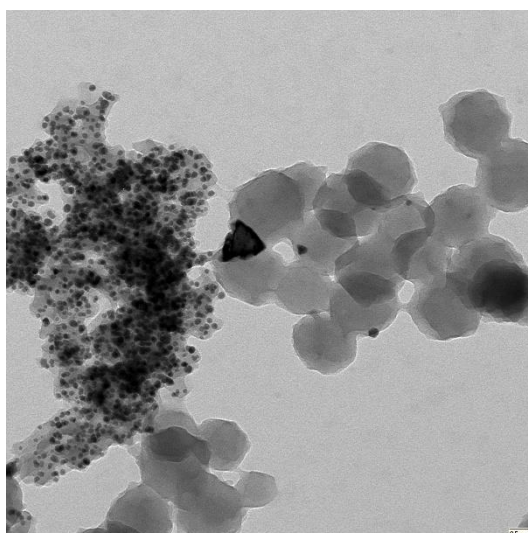
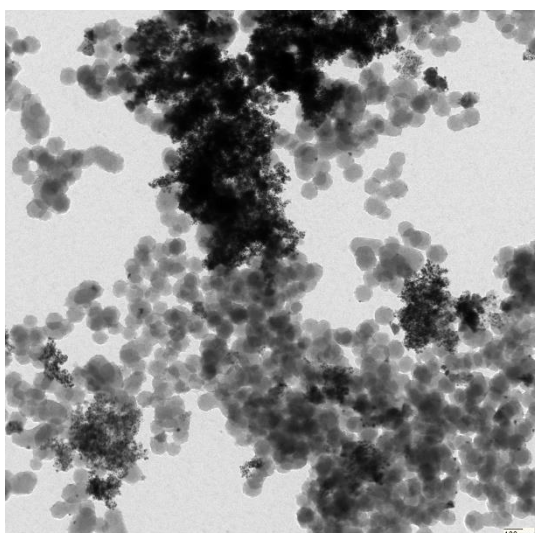
TEM EMIm-TFA-P2:



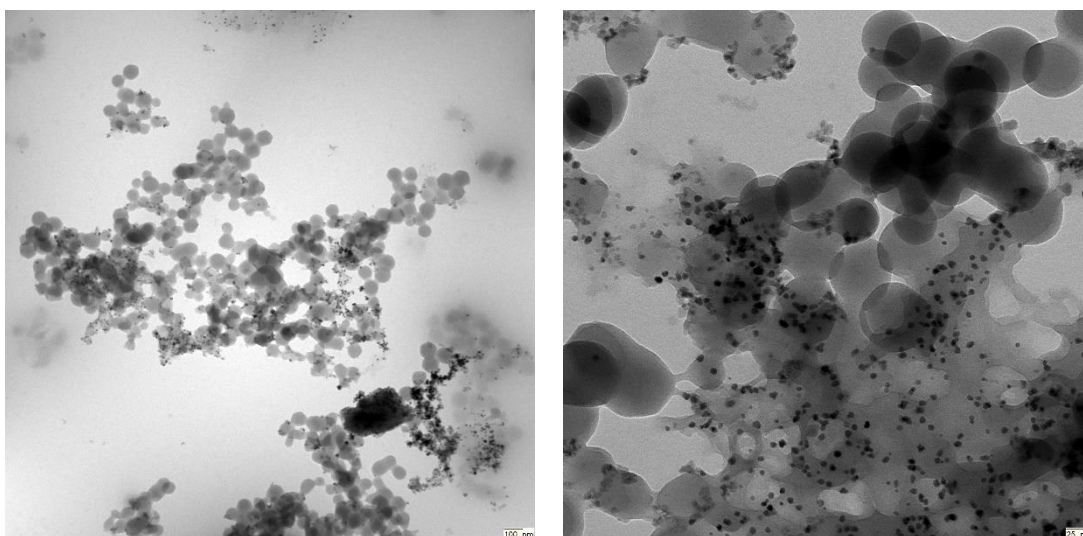
TEM BMPy-BF4-P2:



TEM BMIm-OTf-P2:



TEM DMIm-NTf2-P2:



TEM TmOA-NTf2-P2:

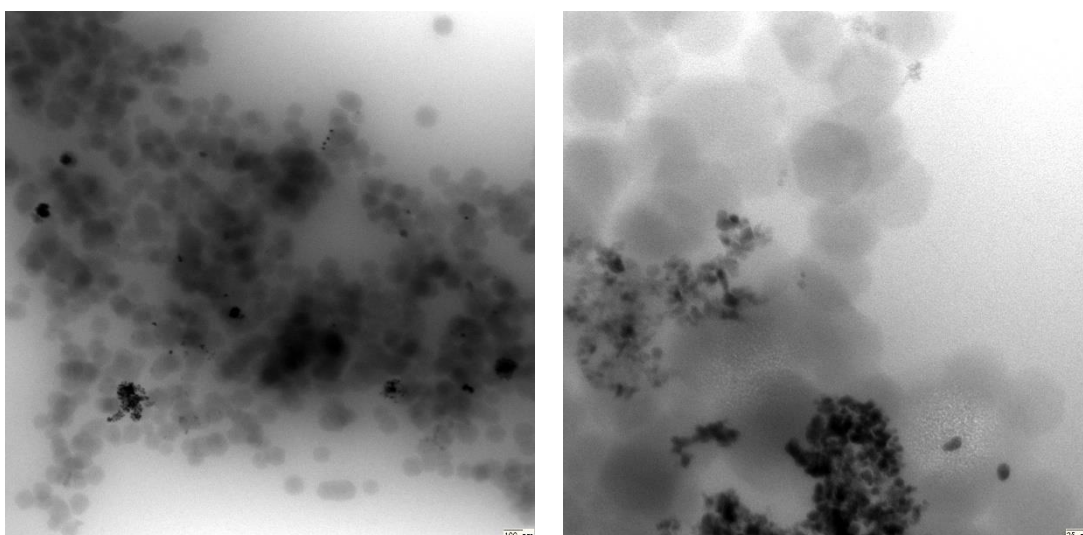
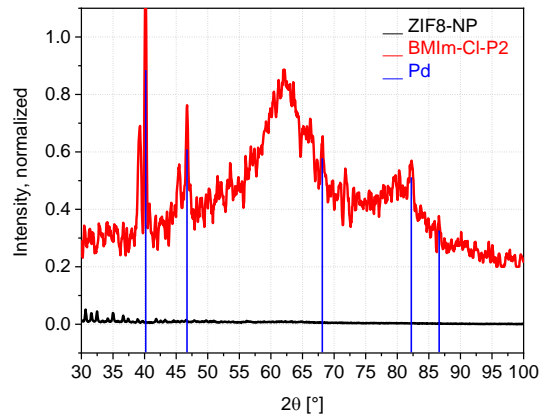
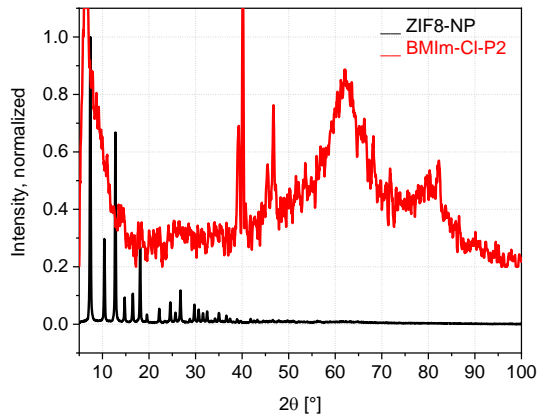
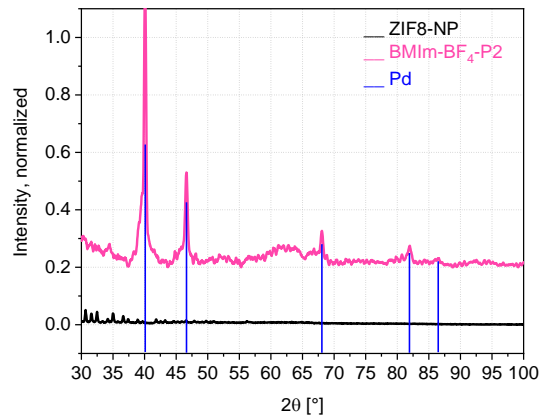
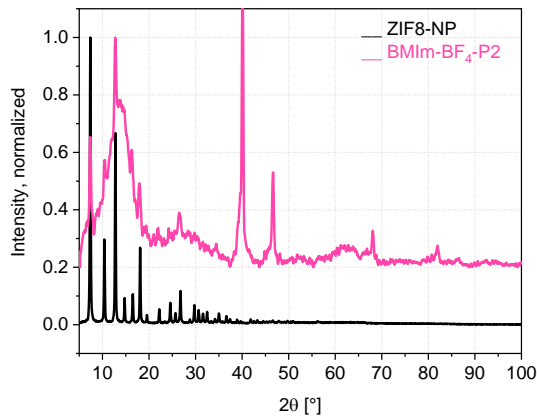


Fig. S27 TEM images of the products obtained in the course of screening targeted Pd-on-ZIF-8-NPs formation from different ILs (scale-bars on the left images are 100 nm and on the right images are 25 nm).

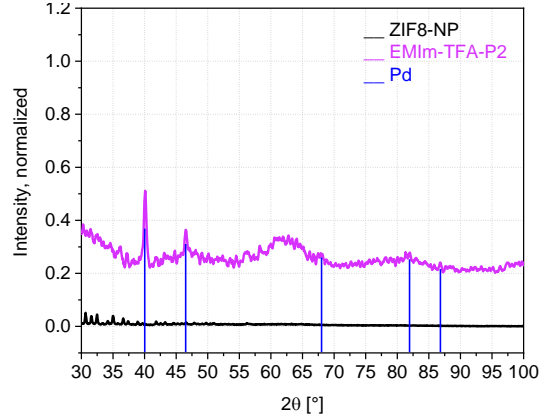
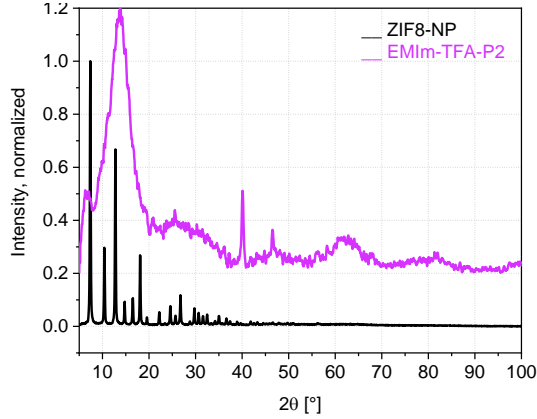
PXRD BMIm-Cl-P2:



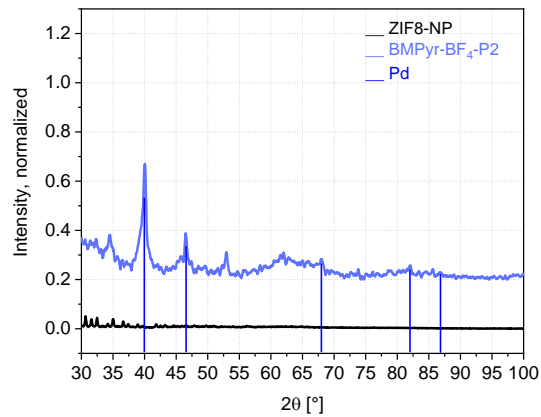
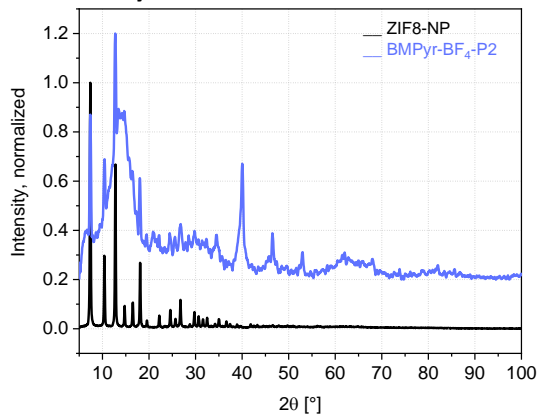
PXRD BMIm-BF₄-P2:



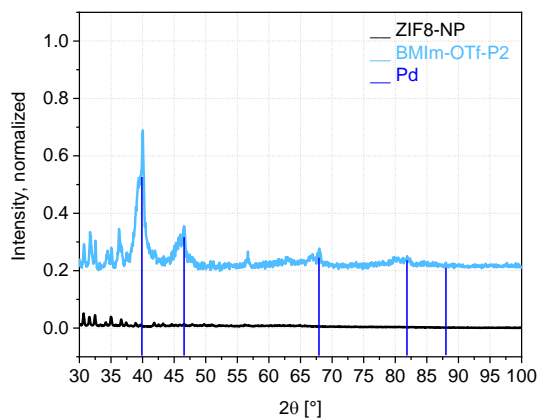
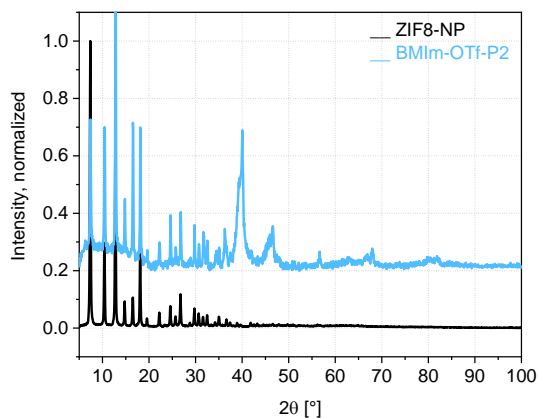
PXRD EMIm-TFA-P2:



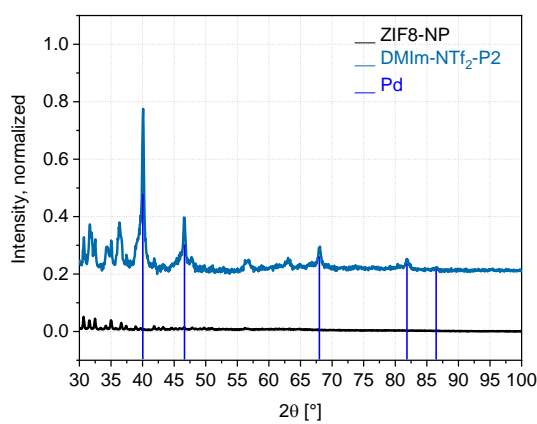
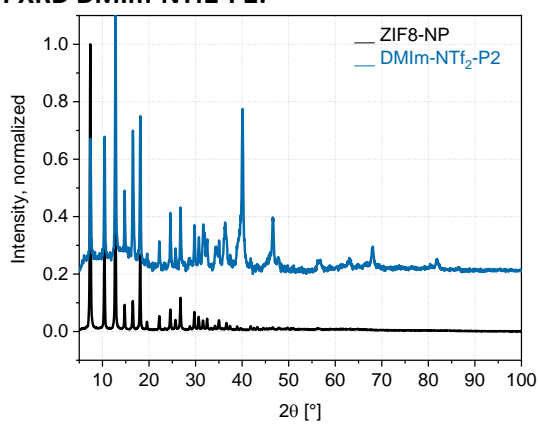
PXRD BMPy-BF₄-P2:



PXRD BMIm-OTf-P2:



PXRD DMIm-NTf2-P2:



PXRD TmOA-NTf2-P2:

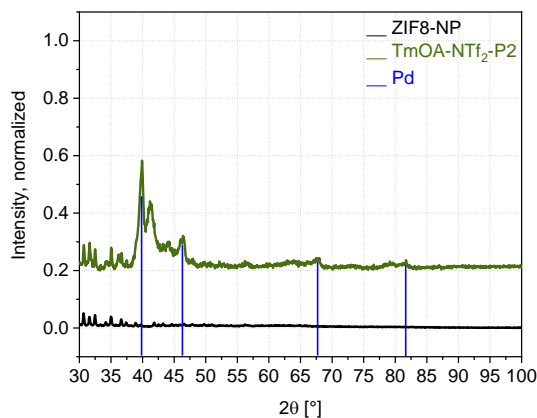
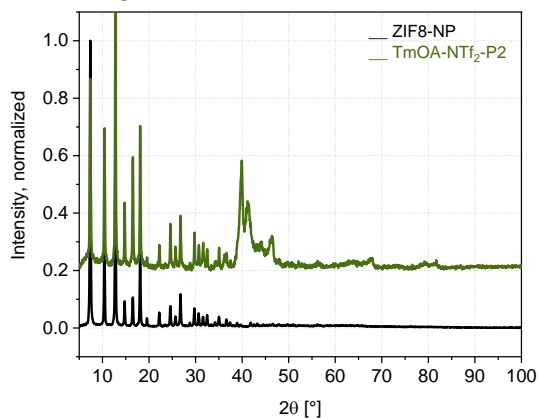


Fig. S28 PXRDs of the products obtained in the course of screening that targeted Pd-on-ZIF-8-NPs formation from different ILs (Pd phases, Fm-3m: COD 9008478 for BMIm-Cl-P2 and BMIm-BF₄-P2; COD 9009820 for BMIm-TFA-P2, BMPy-BF₄-P2, BMIm-OTf-P2, BMIm-NTf₂-P2 and DMIm-NTf₂-P2; COD 1011110 for TmOA-NTf₂-P2).

6 Synthesis of MNP-on-ZIFs

Methods

The preparations were performed in 10 ml borosilicate glass tubes (MW-tubes) equipped with a PTFE-coated magnetic stirring bar and sealed after charging by precursors by a crimp cap with chemically resistant septa. The MW-tube charging and sealing had been performed in a glove box under argon. If not specified, the order of addition was the next: metal precursor, MOF material, and finally the ionic liquid (the order of addition was considered as completely insignificant, as the conversion starts at elevated temperature). The mixture was stirred for a few minutes prior to the start of the process, which was performed under stirring. The typical reaction temperatures were in the range of 180-230 °C during 1-10 minutes. For two-step depositions, the cooled tube was transferred to the glovebox, charged with the solid precursor (either Fe₂CO₉ or PdCl₂), sealed and the MW-treatment was repeated as described above. The reaction parameters are summarized in Table S5.

The workup, performed after automatic cooling down in the MW-reactor was performed as follows. The formed suspension of the nanoparticles was diluted by CH₃CN (4 ml per 1 g of the ionic liquid). This and subsequent operations with liquids were performed using syringing techniques under inert gas conditions via pressurization of MW-tubes by nitrogen gas) and thoroughly mixed. The addition of acetonitrile made the mixture much less viscous. The suspension was centrifuged for 10 minutes (typically ~1000 g) and the residues were washed by 3×4 ml acetonitrile, with a thorough redispersion of the precipitate each time. The product was dried for one day at 10⁻³ mbar and the long-time storage was performed in sealed vessels within a glovebox.

The weight of the isolated products was ~70-90% relative to the weight of the used MOF support. The yields (neither absolute nor percentual) were not given, because they were strongly influenced by the losses during the washing process: part of the nanoparticles was removed during the syringing-off the supernatant.

The simulated PXRD patterns were generated by the program Match [1] using the next Crystallography Open Database (COD) [7] entries: Pd metal - COD 9009820; Fe₃O₄ - COD 1526955.

Analytics (additional notes)

All analyses were performed on materials, which were purified by multiple washings with acetonitrile, as described above.

Notes on the sample-naming conventions

The general encoding convention follows the general code pattern of **[Nanoparticle type(s) by primary element][“-on-“ | “@”][Support type]-[“NP” | -]_[#]**, where “|” is logical OR and expressions in “” are given as they written. The hyphens in the support name might be omitted for better readability (e.g. Pd-on-ZIF-90-CHO-NP is equivalent to the shortened Pd-on-ZIF90NH₂-NP). Further explanations are given below:

[Nanoparticle type(s) by primary element] - the type of the metal nanoparticle(s), enumerated in order of their synthetic immobilization on the support. *E.g.* Fe₃O₄/Pd means that the Fe₃O₄-species were immobilized first, followed by Pd-species.

[“-on-“ | “@”] - “-on-“ designates the formation of composite with deposition of particles, listed on the left on the outside surface of the particles of the type, given on the right. “@” sign corresponds to its standard usage as an indicator of encapsulation: the particles indicated on the left side relative to the designator are encapsulated within (i.e. mostly inside) the support given on the right.

[Support type] - the standard encoding of the MOF support, given with- (full name) or without the “-“ signs (shortened notation, e.g. ZIF8).

[#]-numeric identifier, distinguishing the experiments with otherwise identical codes.

Example: Fe₃O₄/Pd-on-ZIF8-NP_3 means material a nanoparticulated composite no. 3, consisting of ZIF-8 support with surface-immobilized Fe₃O₄ and palladium-based species, with Fe₃O₄ immobilized first.

Summary on the synthesis and properties of NP-on-MOF composites

Table S5 Synthesis and properties of the NP-on-MOF composites.

Probe name	Pd precursor; quantity [mg]	Fe precursor; quantity [mg]	MOF support; quantity [mg]	Ionic liquid; quantity; [g]	Conditions ^{a)}	Size d(M-NP)/d(MOF) ^{b)} [nm]	The synthetic medium before (left) and after the synthesis (right) ^{c)}
Pd-on-ZIF-8-NP	PdCl ₂ ; 17.0	-	ZIF-8-NP; 55.0	[BMIIm][NTf ₂]; 1.02	230°C, 3 min (20 W)	6±1 / 85±9	
Pd-on-ZIF90NH₂	PdCl ₂ ; 20.5	-	ZIF90-NH ₂ ; 51.5	[BMIIm][NTf ₂]; 1.00	180°C, 10 min (20 W)	11±3 / 1200±500	
Pd-on-ZIF90NH₂-NP	PdCl ₂ ; 17.1	-	ZIF90NH ₂ -NP; 50.0	[BMIIm][NTf ₂]; 1.00	180°C, 10 min (20 W)	12±4 / 88±13	
Pd-on-MAF66	PdCl ₂ ; 20.5	-	MAF-66; 51.5	[BMIIm][NTf ₂]; 1.03	180°C, 10 min (20 W)	11±3 / -	
Fe₃O₄-on-ZIF8-NP	-	Fe ₂ (CO) ₉ ; 16.5	ZIF-8-NP; 51.5	[BMIIm][NTf ₂]; 1.01	230°C, 3 min (20 W)	5±2 / 102±16	
Fe₃O₄-on-ZIF90NH₂	-	Fe ₂ (CO) ₉ ; 39.5	ZIF-90-NH ₂ ; 45.0	[BMIIm][NTf ₂]; 1.01	180°C, 10 min (20 W)	13±5 / ~2500±1000	

Fe₃O₄-on-ZIF90NH₂-NP	-	Fe₂(CO)₉ ; 32.9	ZIF-90-NH ₂ -NP; 50.1	[BMIm][NTf ₂]; 1.03	180°C, 10 min (20 W)	11±4 / 81±14	
Pd/Fe₃O₄-on-ZIF8-NP	PdCl₂ ; 17.0	Fe₂(CO)₉ ; 32.5	ZIF-8-NP; 53.3	[BMIm][NTf ₂]; 1.01	230°C, 2×3 min (20 W)	Pd: 11±2 Fe: - / 113±17	
Pd/Fe₃O₄-on-ZIF90NH₂	PdCl₂ ; 8.5	Fe₂(CO)₉ ; 17.0	ZIF-90-NH ₂ ; 21.0	[BMIm][NTf ₂]; 0.52	180°C, 2×10 min (20 W)	Pd: 6±1 Fe: - / 2400±600	
Pd/Fe₃O₄-on-ZIF90NH₂-NP	PdCl₂ ; 17.3	Fe₂(CO)₉ ; 33.4	ZIF-90-NH ₂ -NP; 50.5	[BMIm][NTf ₂]; 1.03	180°C, 2×10 min (20 W)	Pd: 10±2 Fe: - / 74±12	
Pd/Fe₃O₄-on-MAF-66	PdCl₂ ; 9.0	Fe₂(CO)₉ ; 16.5	MAF-66; 25.5	[BMIm][NTf ₂]; 0.51	200°C, 2×3 min (20 W)	Pd: 8±5 / Fe: - 430±180	
Fe₃O₄-/Pd-on-ZIF8-NP	PdCl₂ ; 17.0	Fe₂(CO)₉ ; 33.3	ZIF-8-NP 50.5	[BMIm][NTf ₂]; 1.02	230°C, 2×3 min (20 W)	Fe: 5±3 Pd: - 104±17	
Fe₃O₄-/Pd-on-ZIF90NH₂-NP	PdCl₂ ; 17.4	Fe₂(CO)₉ ; 33.2	ZIF-90-NH ₂ -NP (1) 49.5 mg	[BMIm][NTf ₂]; 1.02	180°C, 2×10 min (20 W)	Fe: 13±4 Pd: - / 71±13	

^{a)} The notation “2×10 min” means that two deposition stages were done. In the arbitrary example of Pd/Fe₃O₄-on-ZIF8-NP, the first stage MW-reaction had been done on the Pd-precursor and MOF, while the second stage on the Fe₃O₄-precursor was added to outcome of the first stage.

^{a)} TEM-based size, <d>±σ, where <d> is the average size and σ is the variance.

6.1 Pd-on-ZIF8-NP, Pd-on-ZIF-90-NH₂, Pd-on-ZIF90NH₂-NP, Pd-on-MAF66

TEM

Pd-on-ZIF8-NP

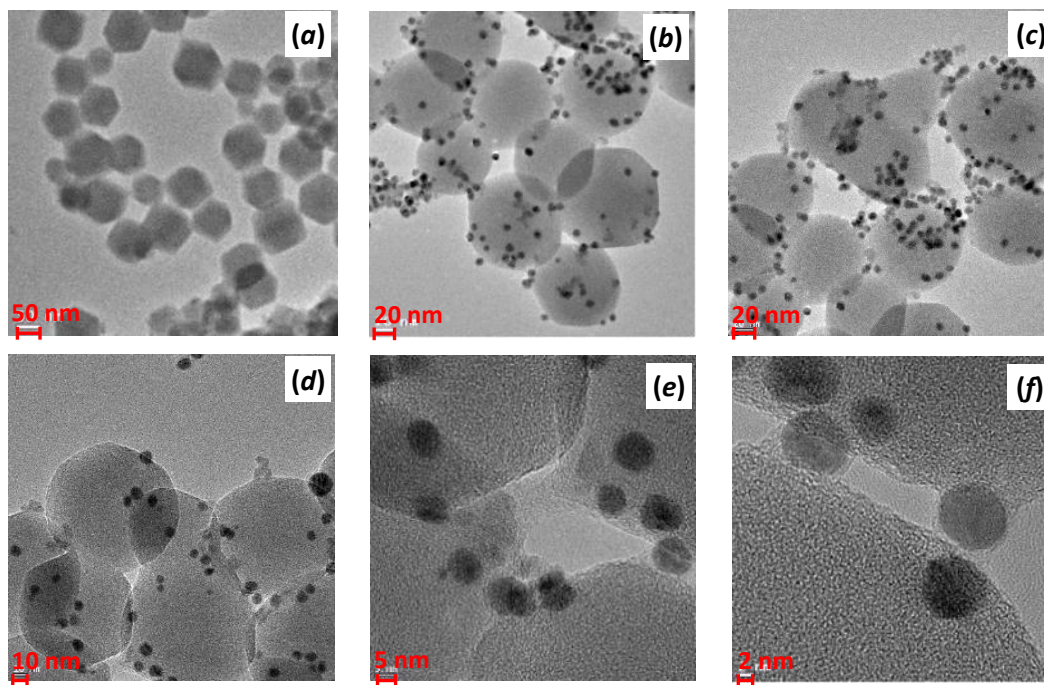


Fig. S29 Comparison of the TEM images of (a) ZIF8-NP [ZIF-8 prior to deposition: 75 ± 17 nm] and (b-e) Pd-on-ZIF8-NP [Pd: 6 ± 1 nm; ZIF-8: 85 ± 9 nm]

Pd-on-ZIF-90-NH₂

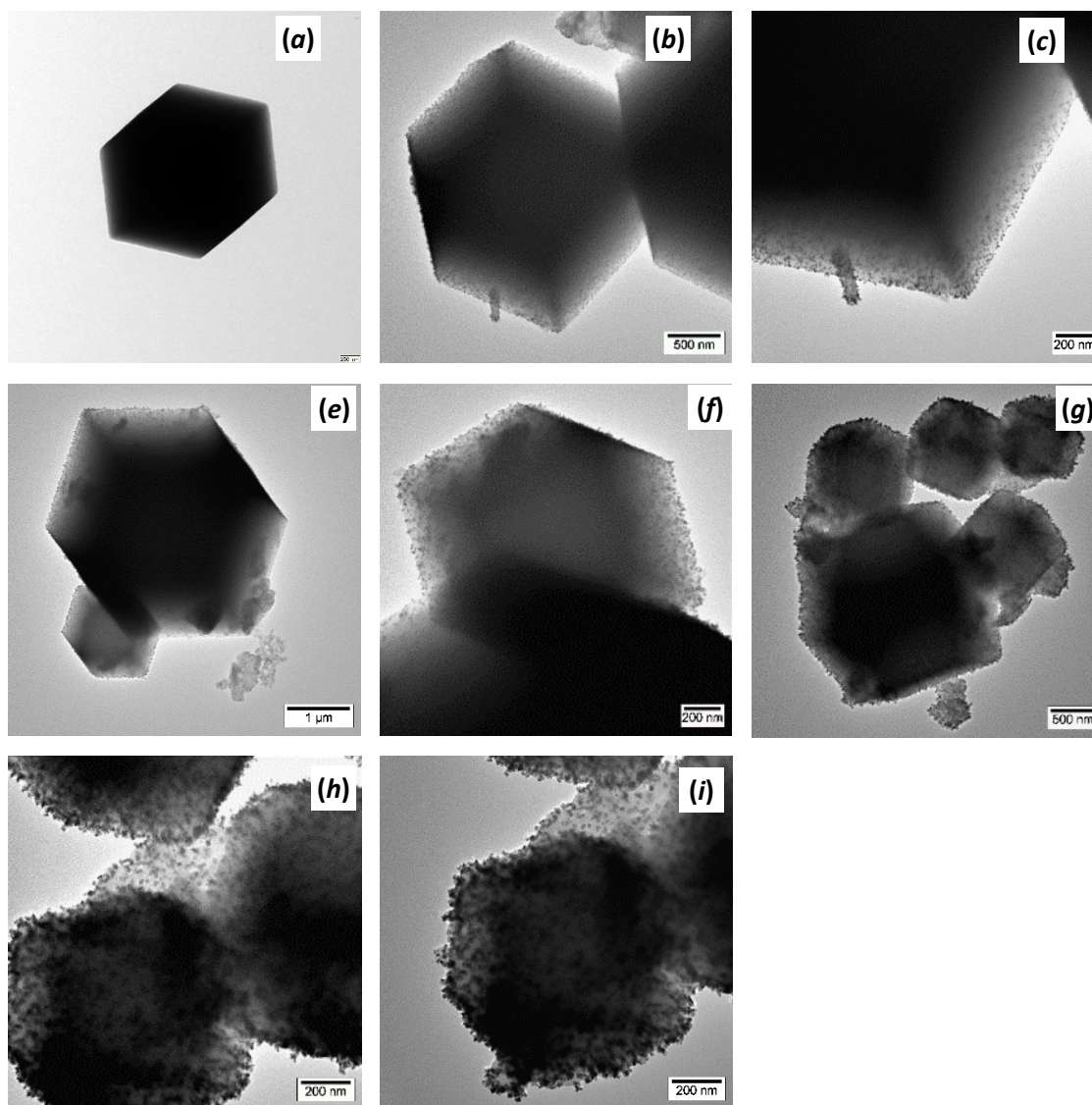


Fig. S30 Comparison of the TEM images of (a) ZIF90NH₂ [ZIF90NH₂ prior to deposition: 1.2 ± 0.5 μm] and (b-h) Pd-on-ZIF90NH₂ [Pd: 11 ± 3 nm; ZIF90NH₂: 1.2 ± 0.5 μm]

ZIF-90-NH₂-NP

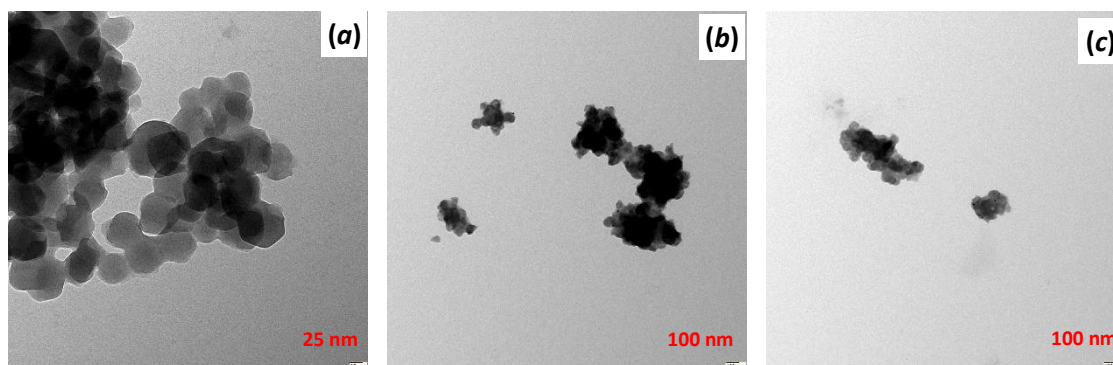


Fig. S31 Comparison of the TEM images of (a) ZIF90NH₂-NP [ZIF90NH₂-NP prior to deposition: 71±12 nm] and (b-h) Pd-on-ZIF90NH₂-NP [Pd: 12±4 nm; ZIF90NH₂-NP: 88±13 nm]

Pd-on-MAF66

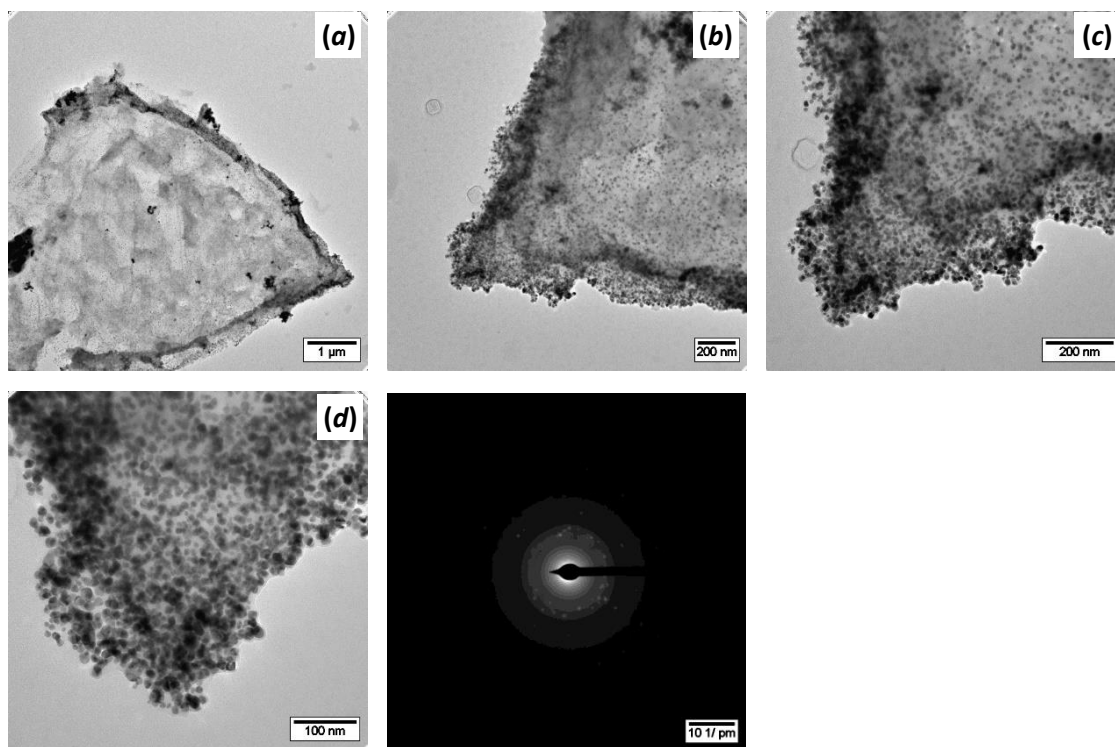


Fig. S32 Comparison of the TEM images of (a) MAF-66 [MAF-66 prior to deposition: no reliable TEM based data] and (b-e) Pd-on-MAF66 [Pd: 11 ± 3 nm; no reliable TEM based data].

SEM/EDX element mapping/composition

Pd-on-ZIF8-NP

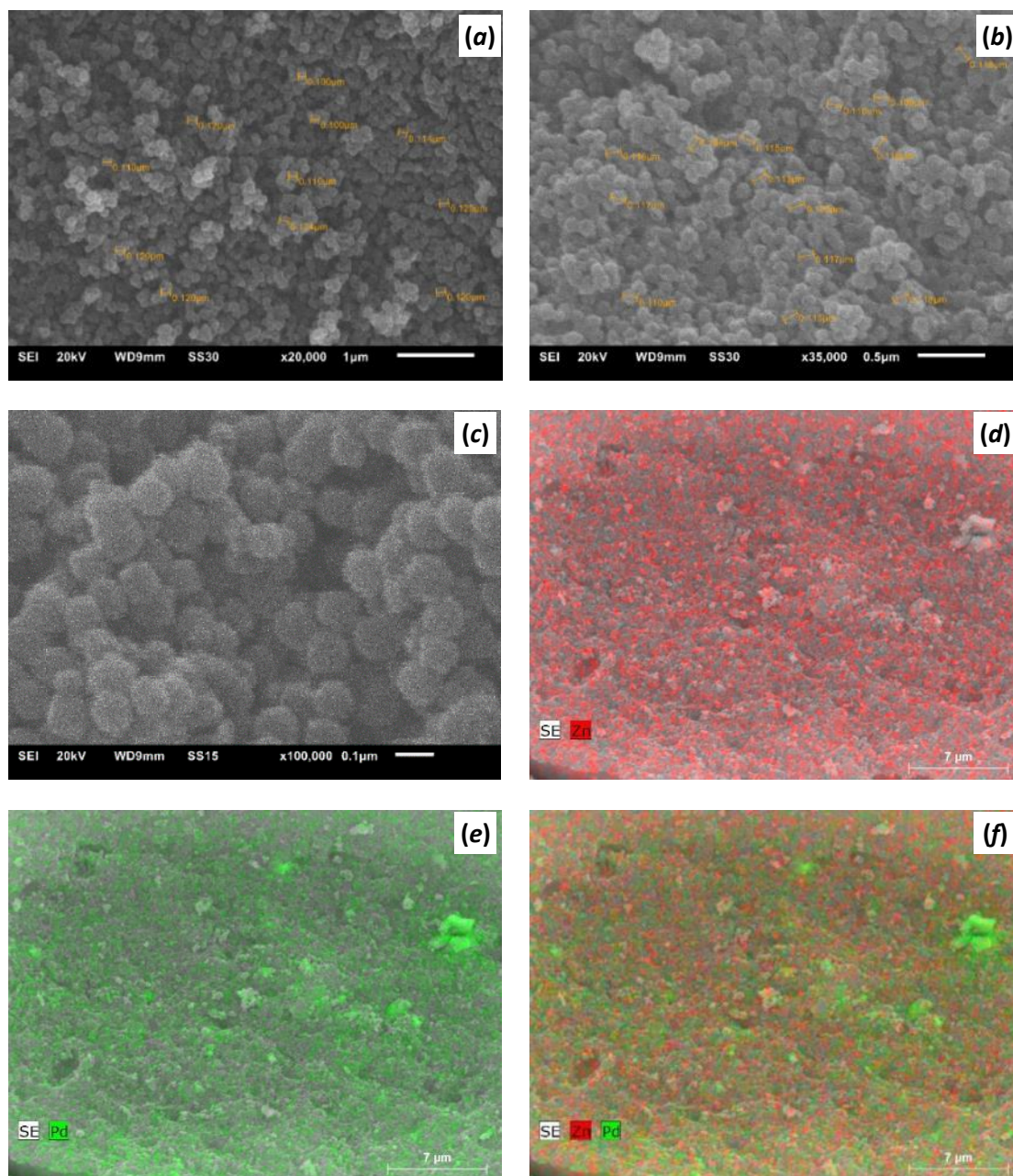


Fig. S33 SEM micrographs of: (a) ZIF8-NP and (b-c) Pd-on-ZIF8-NP materials. (d-f) EDX-Mapping of Pd-on-ZIF8-NP. Zn:Pd ratio is 5.47.

Pd-on-ZIF90NH₂

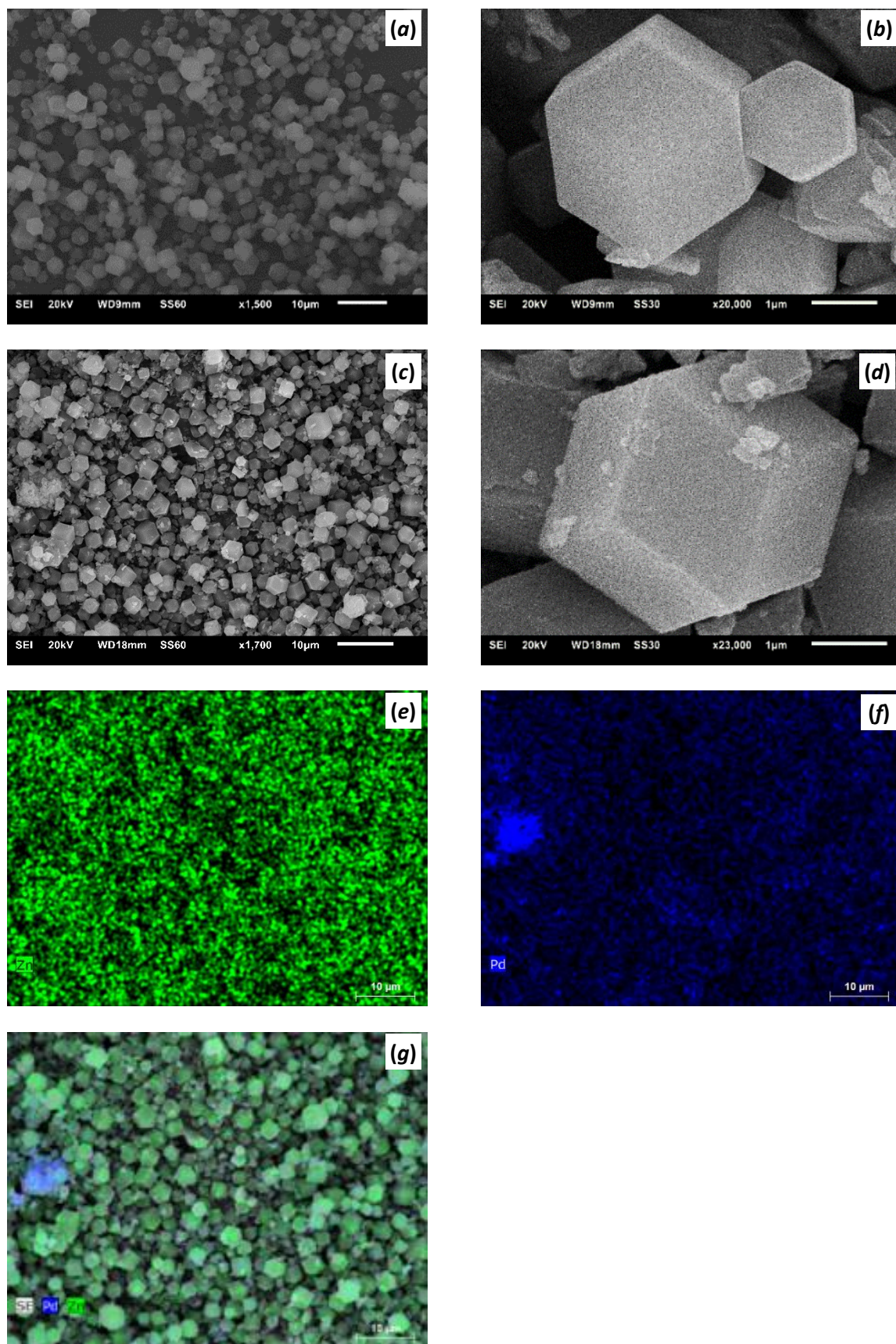


Fig. S34 SEM micrographs of: (a-b) ZIF90NH₂ and (c-d) Pd-on-ZIF90NH₂ materials. (e-g) EDX-Mapping of Pd-on-ZIF90NH₂. Zn:Pd ratio is 5.92.

Pd-on-ZIF90NH₂-NP

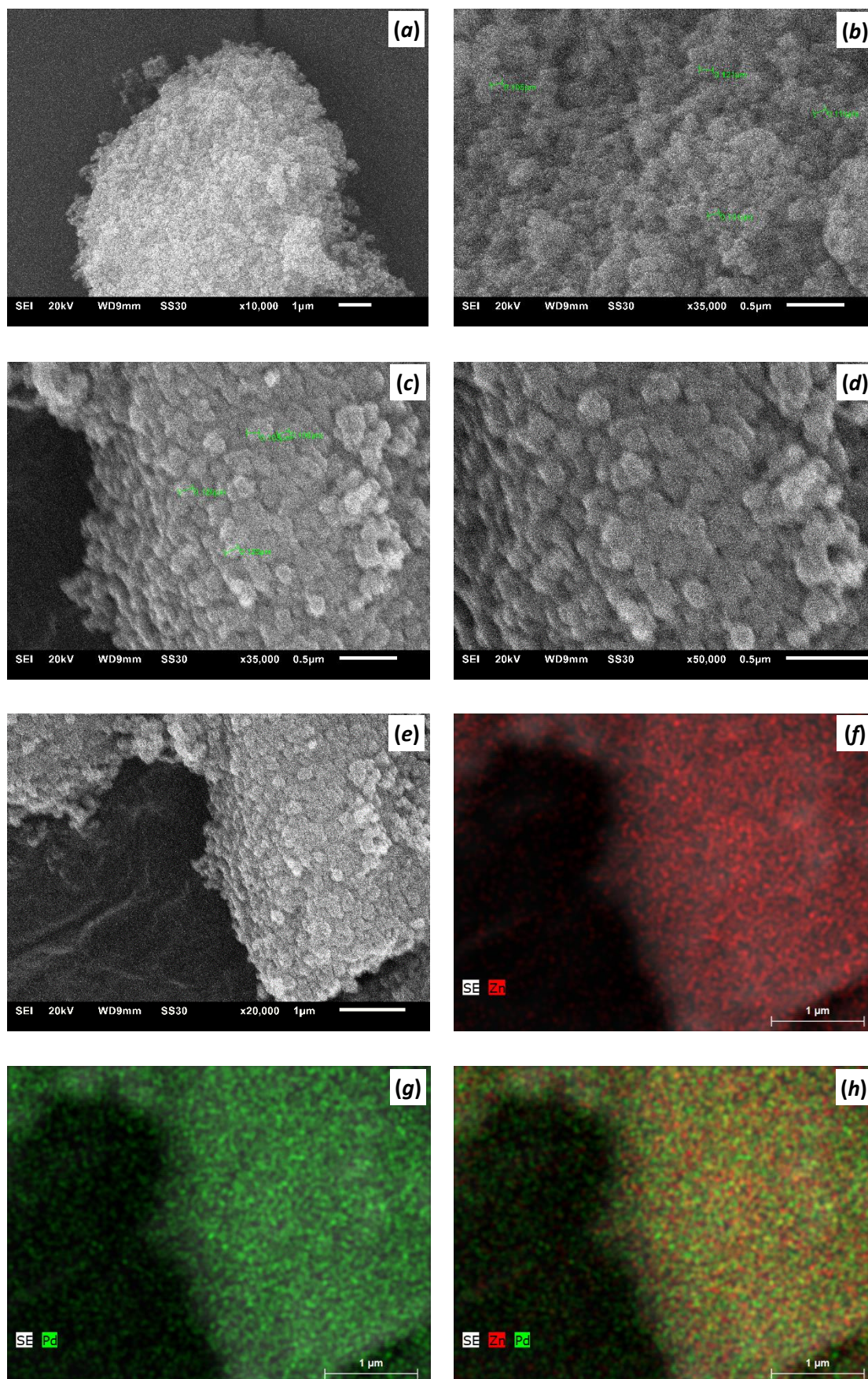


Fig. S35 SEM micrographs of: (a-b) ZIF90NH₂-NP and (c-e) Pd-on-ZIF90NH₂-NP materials. (f-h) EDX-Mapping of Pd-on-ZIF90NH₂-NP. Zn:Pd ratio is 8.26

Pd-on-MAF66

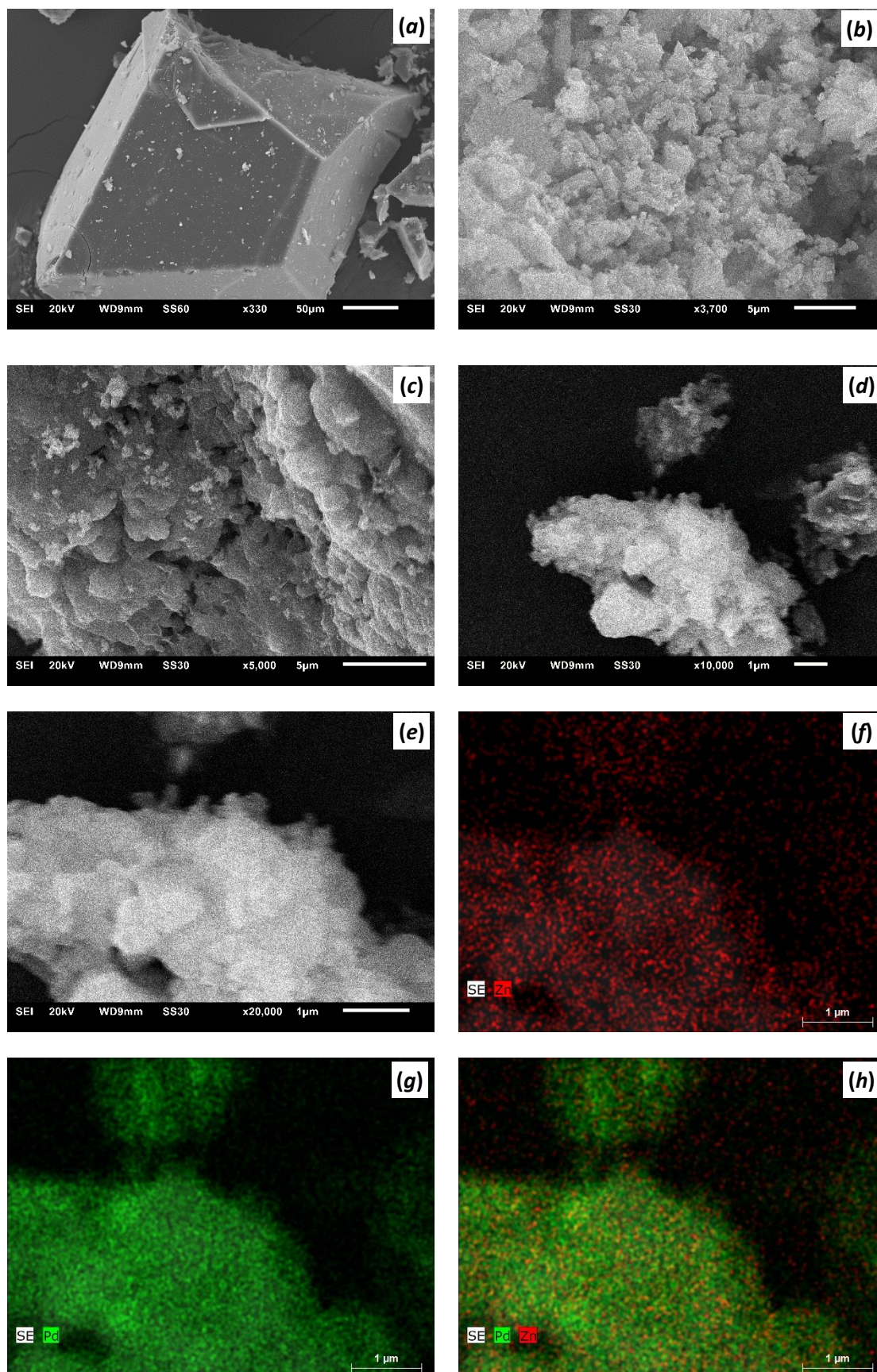


Fig. S36 SEM micrographs of: (a-b) MAF-66 and (c-e) Pd-on-MAF66 materials. (f-h) EDX-Mapping of Pd-on-MAF66. **Zn:Pd ratio is 0.20**; a possible artefact, the data was considered as an outlier.

AAS and SEM/EDX based Pd-content comparison

Sample	AAS Pd-content [% _{atom}]	SEM-EDX Pd-content [% _{atom}]
Pd-on-ZIF8-NP	15.85	15.45
Pd-on-ZIF90NH ₂	4.57	3.09
Pd-on-ZIF90NH ₂ -NP	12.36	7.52
Pd-on-MAF66	8.75	40.33

PXRD

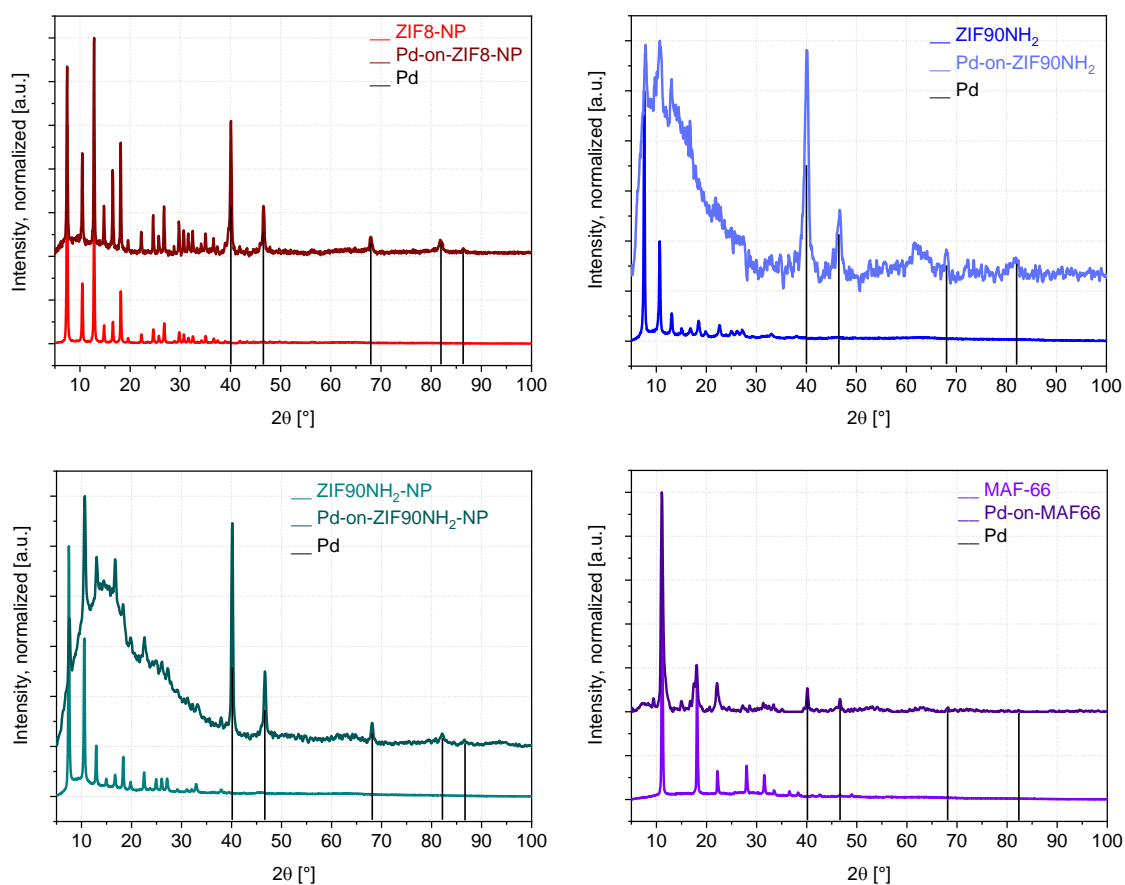


Fig. S37 Comparison of the PXRD patterns of Pd-on-ZIF-8, Pd-on-ZIF-90-NH₂, and Pd-on-ZIF-90-NH₂-NP materials with the patterns of the pristine MOF supports. The peak positions corresponding to Pd-metal are overlaid.

N₂ adsorption

The samples were activated at ~120-140 °C during ~12 h.

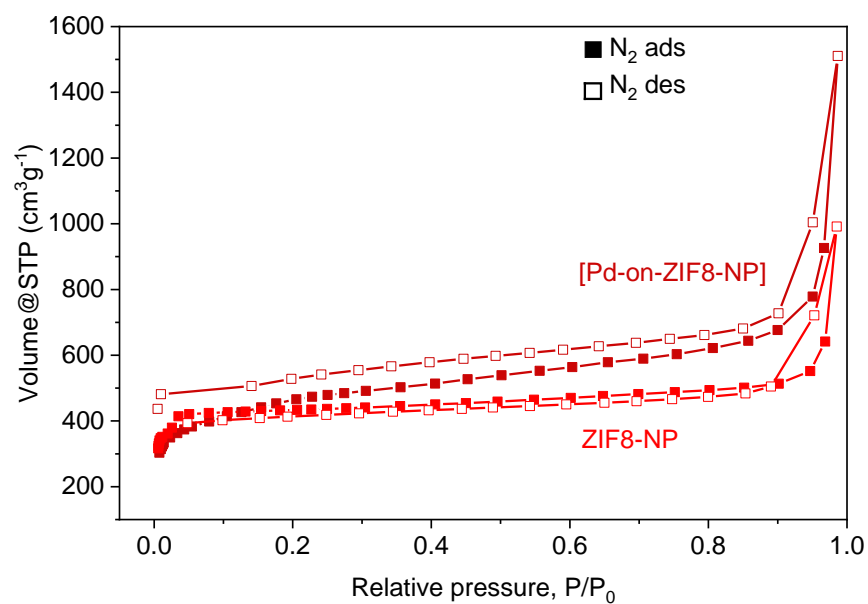


Fig. S38 N₂ adsorption isotherms for the Pd-on-ZIF8-NP composite ($S_{\text{BET}} = 1646 \text{ m}^2 \text{ g}^{-1}$) and the ZIF8-NP support ($S_{\text{BET}} = 1641 \text{ m}^2 \text{ g}^{-1}$).

6.2 Fe₃O₄-on-ZIF-8-NP, Fe₃O₄-on-ZIF90NH₂, and Fe₃O₄-on-ZIF90NH₂-NP

The MW tubes were charged by the precursors as described in the Methods section at the beginning of the chapter and the MW-heating assisted reaction was conducted for a specified time under standard conditions (the reaction parameters are summarized in Table S5). The workup was standard, 2 ml of CH₃CN was used for each washing.

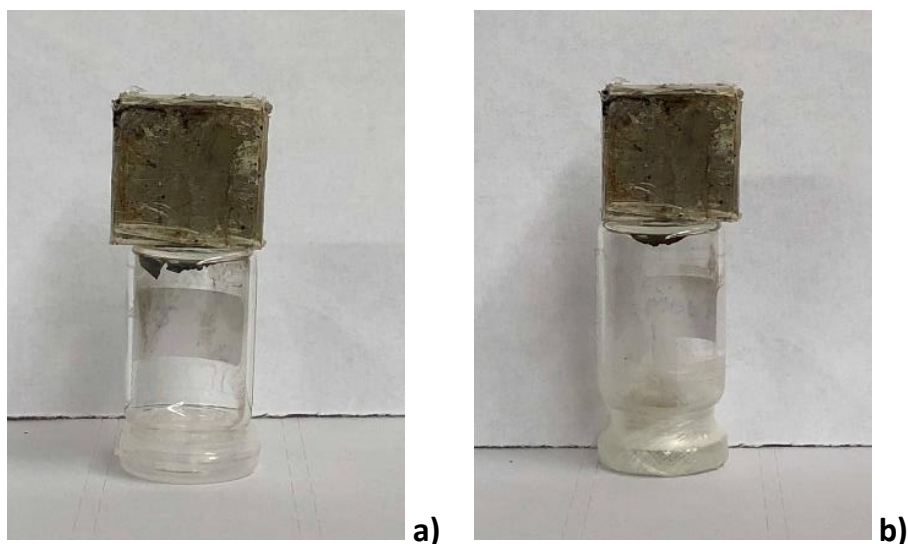


Fig. S39 Photos demonstrating the ferromagnetism of: (a) Fe₃O₄-on-ZIF8-NP and (b) Fe₃O₄-on-ZIF90NH₂. The samples, consisting of fine non-sticky powder fell immediately after the removal of the magnet on the top of the vials.

The ferromagnetism of the particles did not disappear after prolonged exposure of the particles to the air.

TEM

Fe₃O₄-on-ZIF8-NP

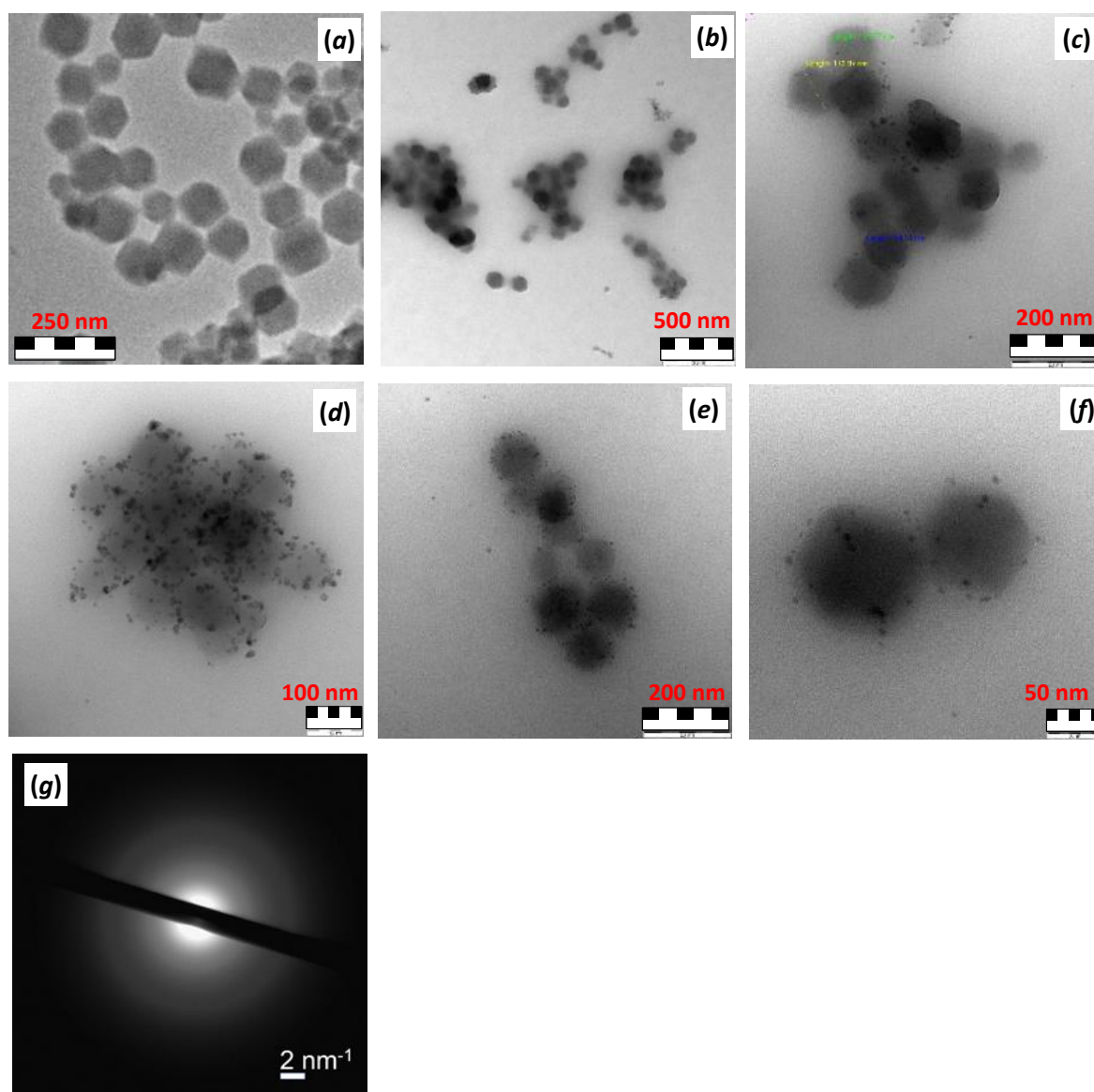


Fig. S40 Comparison of the TEM images of (a) ZIF8-NP [ZIF-8 prior to deposition: 83±12 nm] ; (b-f) Fe₃O₄-on-ZIF8-NP [Fe₃O₄: 5±2 nm; ZIF-8: 102±16 nm]; (g) SAED.

Fe_3O_4 -on-ZIF90NH₂

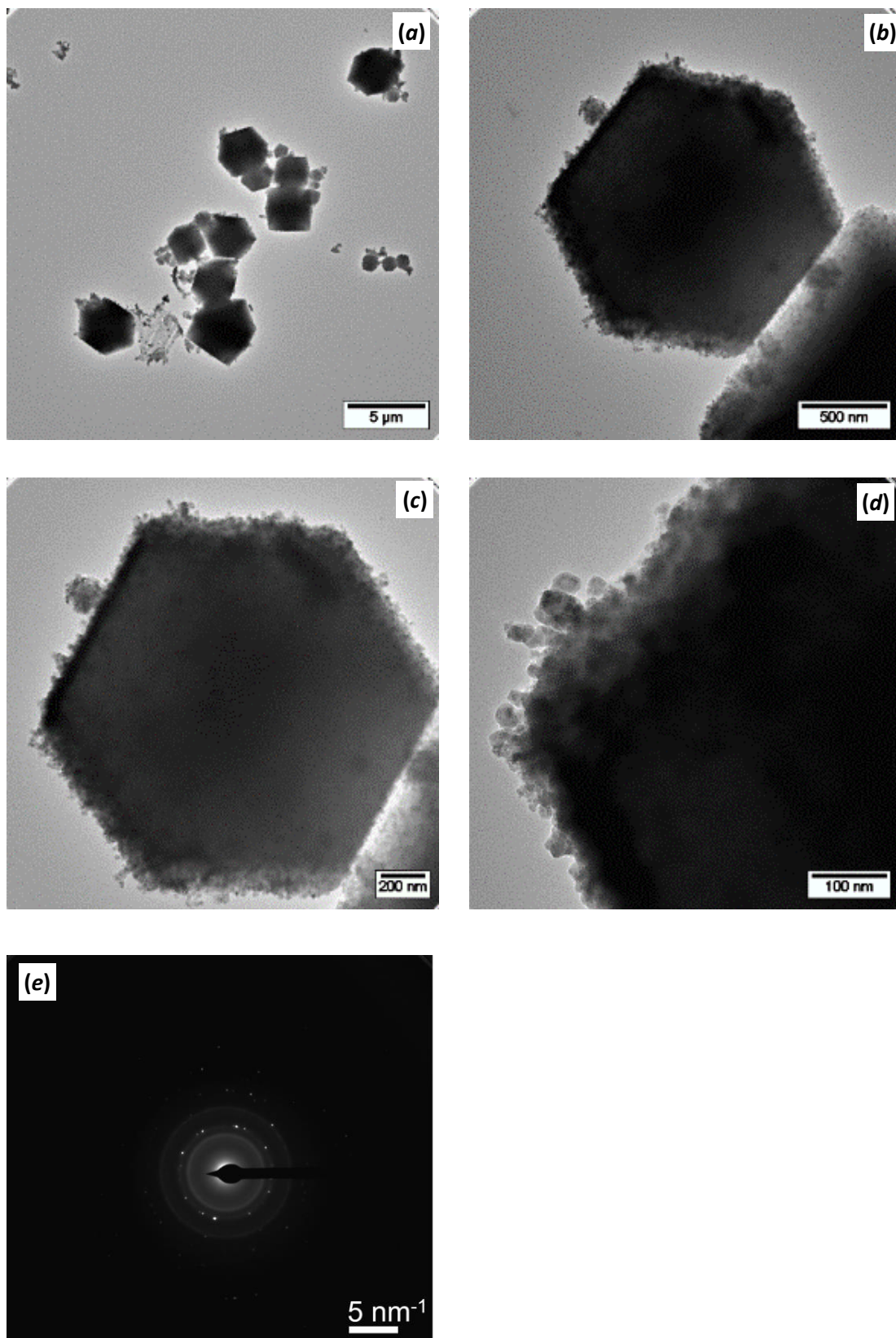


Fig. S41 (a-d) TEM images of Fe_3O_4 -on-ZIF90NH₂ [$2.5 \pm 1.0 \mu\text{m}$] and [Fe: $13 \pm 5 \text{ nm}$; ZIF-90-NH₂: $2.5 \pm 1.0 \mu\text{m}$]; (e) (SAED).

Fe_3O_4 -on-ZIF90NH₂-NP

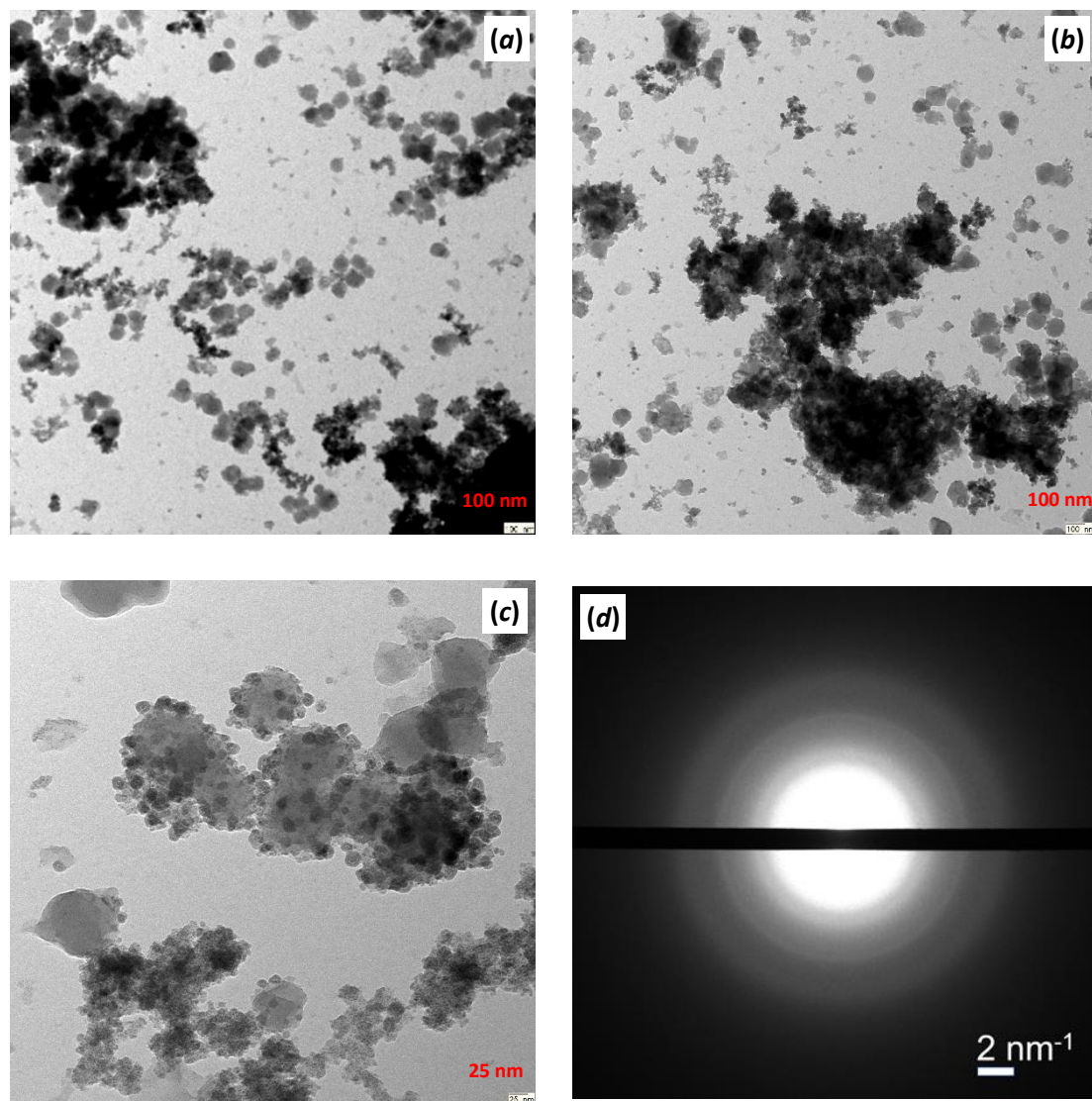


Fig. S42 (a-c) TEM images of Fe_3O_4 -on-ZIF90NH₂-NP [Fe: 11 ± 4 nm; ZIF-90NH₂-NP: 81 ± 14 nm]; (d) SAED.

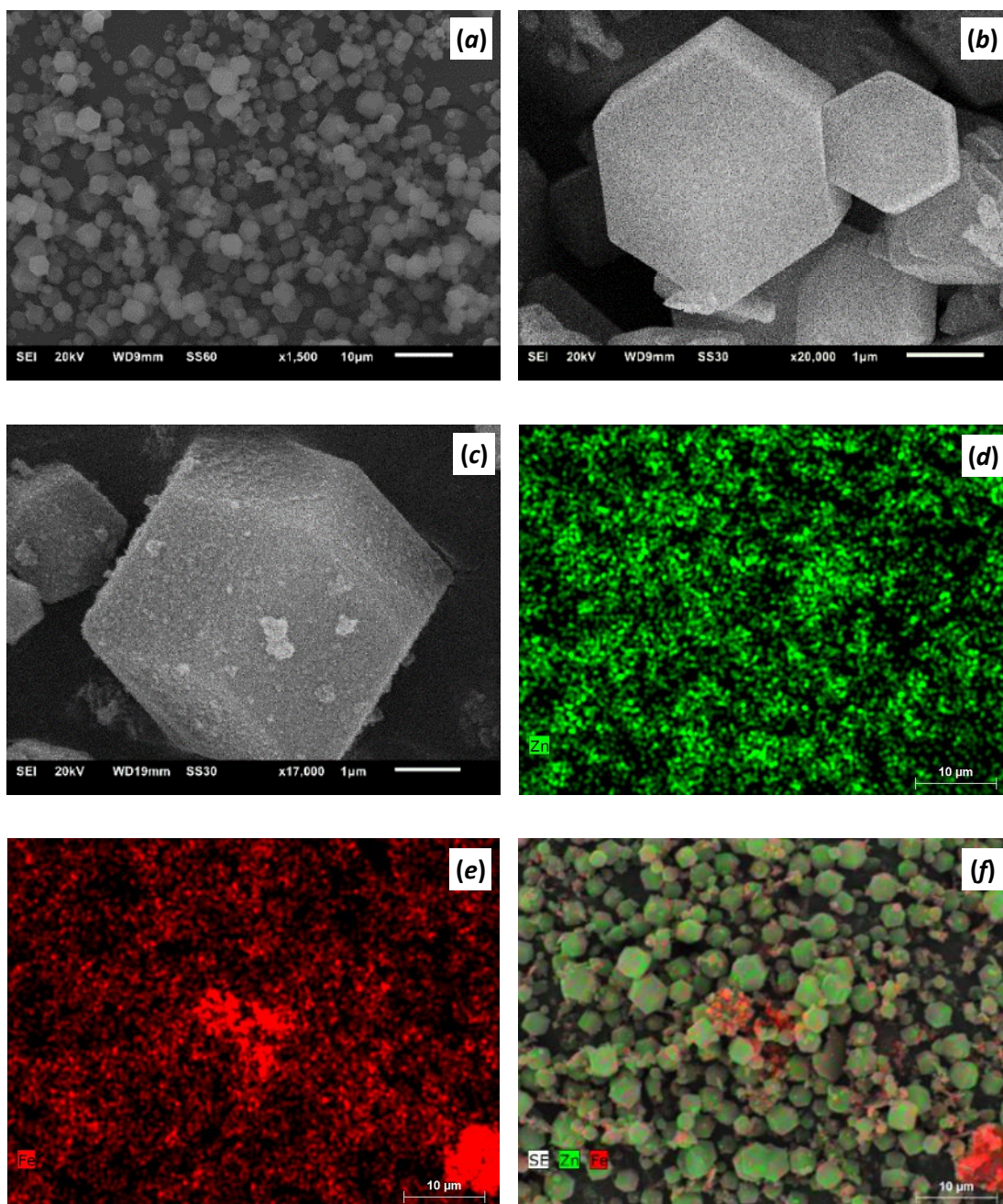


Fig. S44 SEM micrographs of (a,b) ZIF90NH₂ and (c) Fe₃O₄-on-ZIF90NH₂.(d-f) EDX element mapping for Fe₃O₄-on-ZIF-90NH₂. Note that while there are some places with locally concentrated deposition of iron, the general distribution is fairly uniform, which is well visible on the overlay, pane (f). **Zn:Pd ratio is 3.24.**

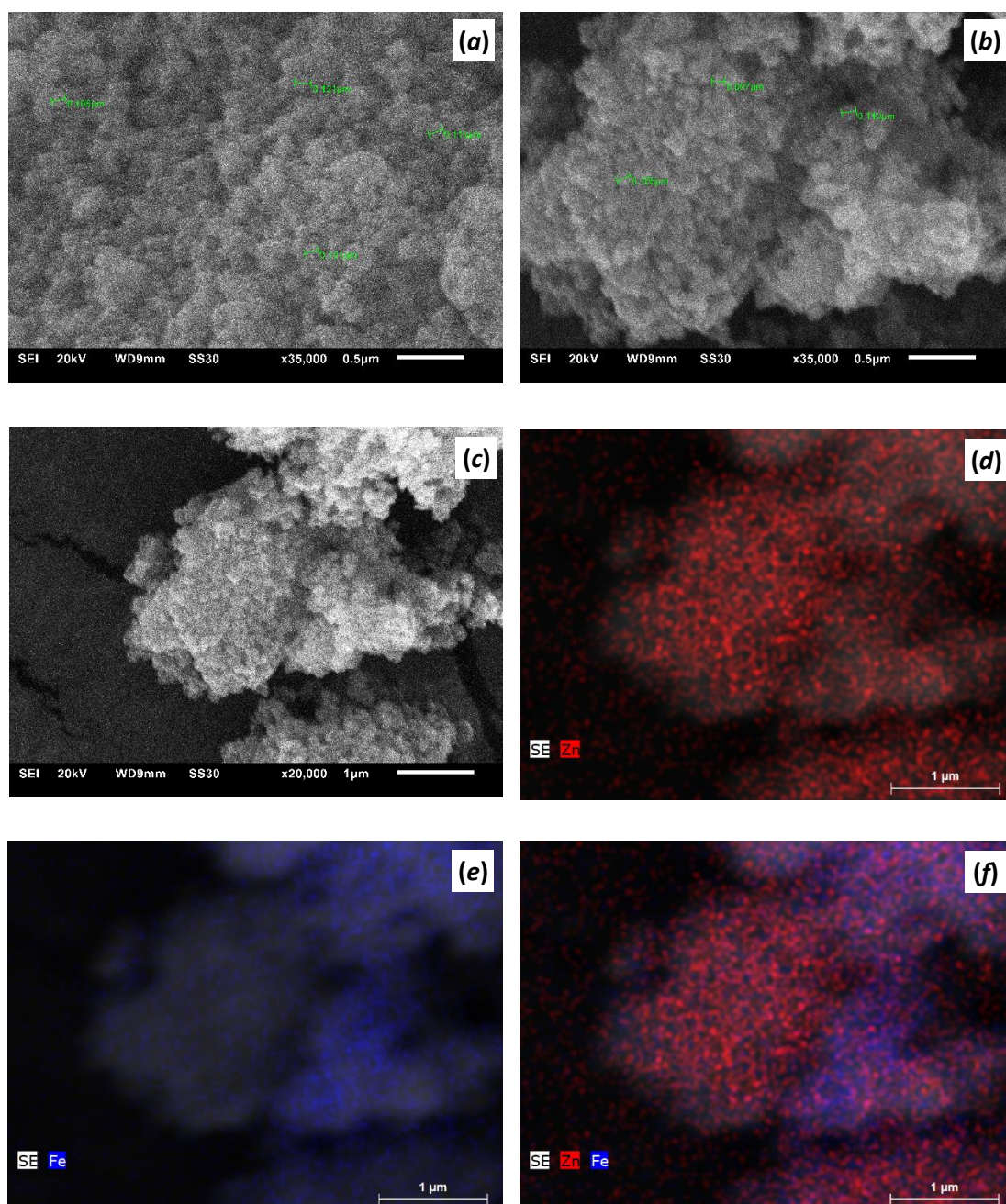


Fig. S45 SEM micrographs of: (a) ZIF90NH₂-NP; (b,c) Fe₃O₄-on-ZIF90NH₂-NP; (d-f) EDX element mapping for Fe₃O₄-on-ZIF-90NH₂-NP. Note the presence of Fe on all surface, even if certain variation is noticeable. **Zn:Fe ratio is 0.79.**

AAS and SEM/EDX based Fe-content comparison

Sample	AAS Fe-content [% _{atom}]	SEM-EDX Fe-content [% _{atom}]
Fe ₃ O ₄ -on-ZIF8-NP	11.86	16.71
Fe ₃ O ₄ -on-ZIF90NH ₂	21.54	1.38 (outlier)*
Fe ₃ O ₄ -on-ZIF90NH ₂ -NP	16.69	55.58 (outlier)*

*-outliers were sometimes observed for SEM and particularly TEM due to the limited amount of measurements (samplings). The problem is particularly typical for STEM with a very small sampling area (see also Table S6 for an example).

PXRD

The PXRD patterns of the Fe_3O_4 -on-MOFNP particles are nearly coinciding with the ones for the MOFs, suggesting the amorphicity of the iron-containing species. However, the presence of Fe_3O_4 is unambiguous due to the ferromagnetism of the samples, both before and after exposure to air. In a number of cases, the presence of Fe_3O_4 is evident from the SAED imaging.

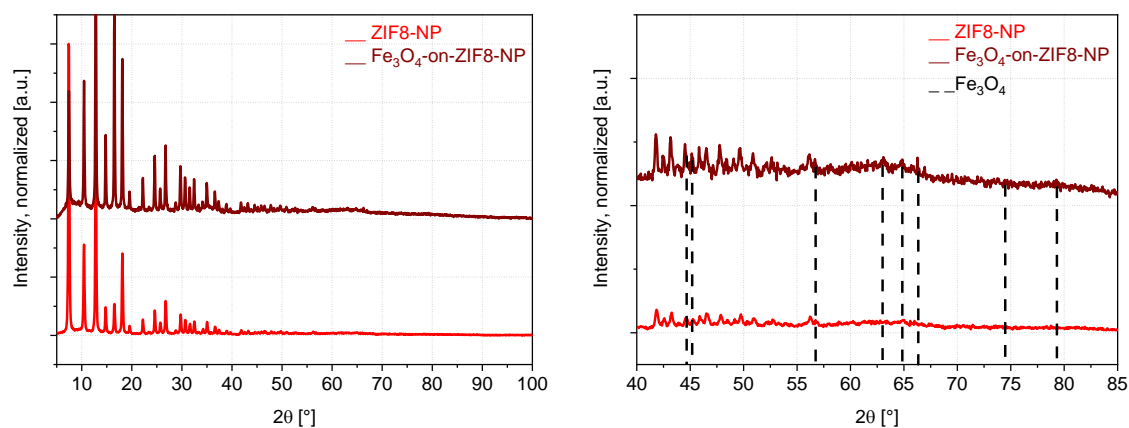


Fig. S46 Comparison of the PXRD patterns of Fe_3O_4 -on-ZIF8-NP and the ZIF-8 support. The peak positions corresponding to Fe_3O_4 are overlaid in the expansion (right).

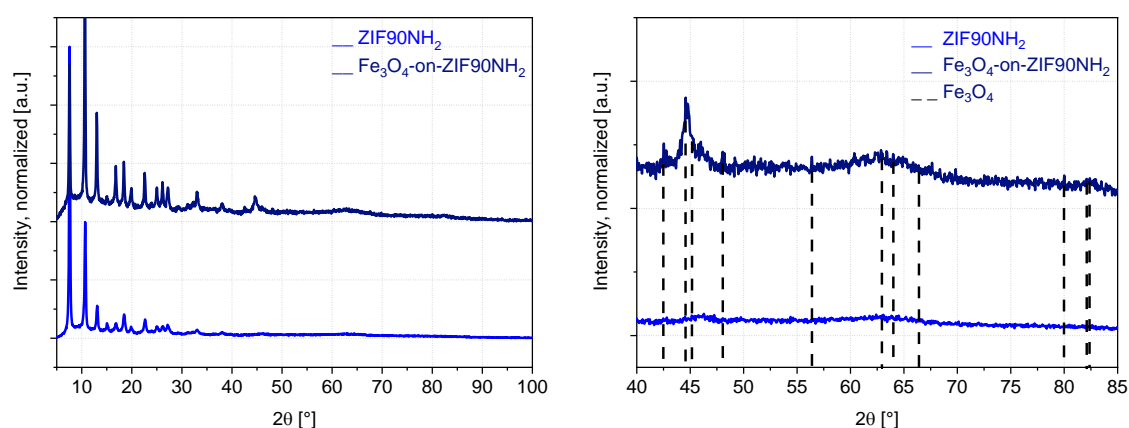


Fig. S47 Comparison of the PXRD patterns for the Fe_3O_4 -on-ZIF-90-NH₂ and the ZIF-90-NH₂ support. The peak positions corresponding to Fe_3O_4 are overlaid in the expansion (right).

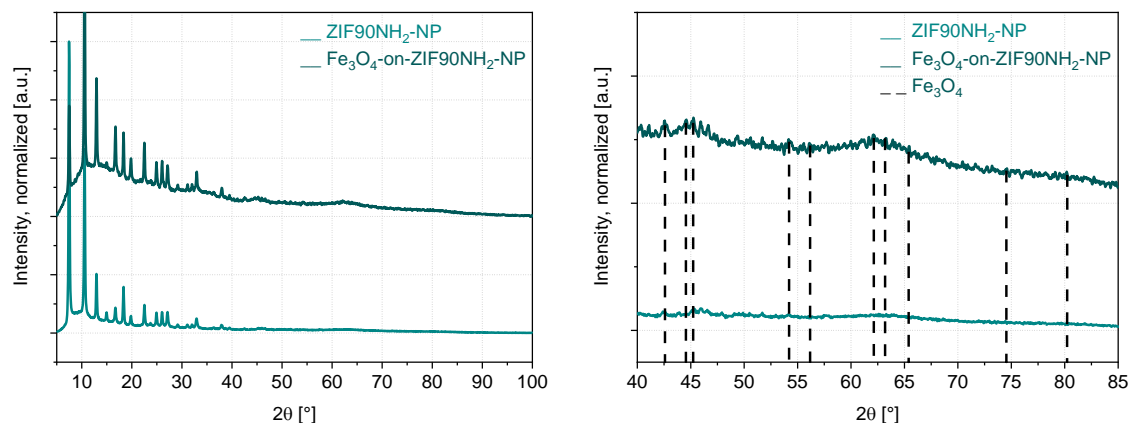


Fig. S48 Comparison of the PXRD patterns for the Fe_3O_4 -on-ZIF-90-NH₂-NP and the ZIF-90-NH₂-NP support. The peak positions corresponding to Fe_3O_4 are overlaid in the expansion (right).

N₂ adsorption

The samples were activated at ~120-140 °C during ~12 h. The strong decrease of the surface area of Fe₃O₄-on-ZIF8-NP compared to ZIF8-NP is believed to take place due to pore obturation.

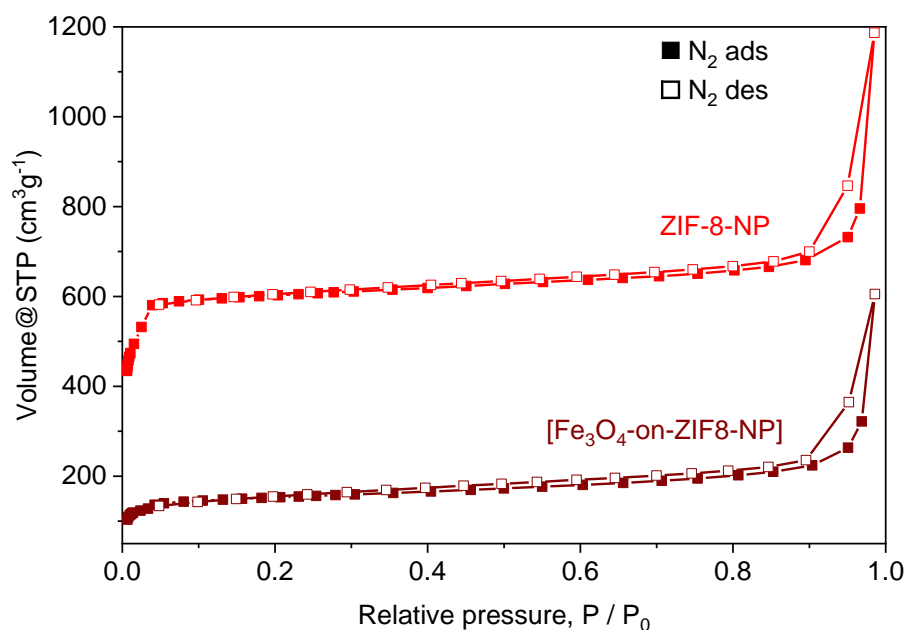


Fig. S49 N₂ adsorption isotherms for the Fe₃O₄-on-ZIF8-NP composite ($S_{\text{BET}} = 568 \text{ m}^2 \text{ g}^{-1}$) and the respective ZIF8-NP support ($S_{\text{BET}} = 2295 \text{ m}^2 \text{ g}^{-1}$ for this case; note that the supports were synthesized in different batches, hence the value is varied).

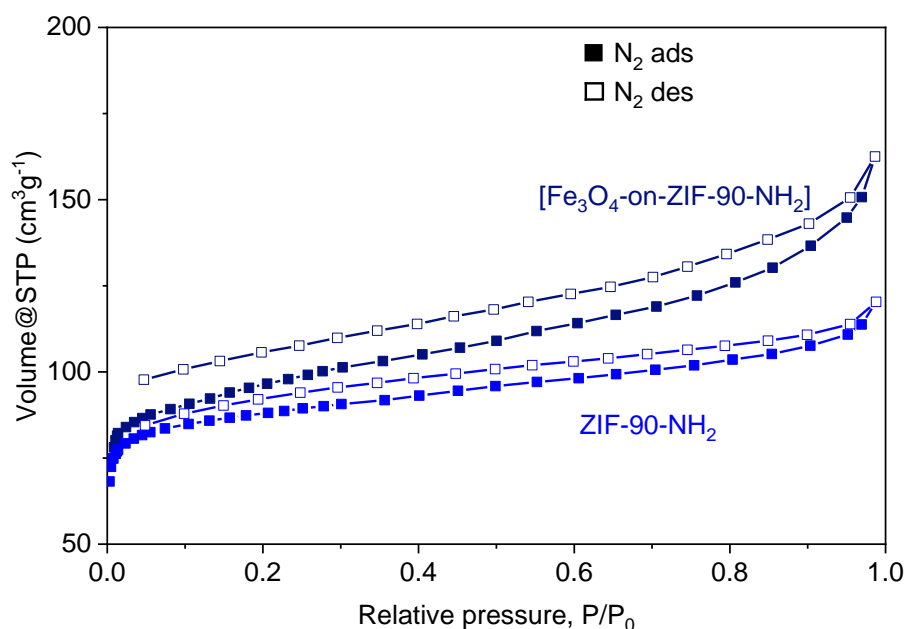


Fig. S50 N₂ adsorption isotherms for the Fe₃O₄-on-ZIF-90-NH₂ composite ($S_{\text{BET}} = 362 \text{ m}^2 \text{ g}^{-1}$) and the ZIF-90-NH₂ support ($S_{\text{BET}} = 344 \text{ m}^2 \text{ g}^{-1}$).

6.3 Pd/Fe₃O₄-on-ZIF8-NPs, Pd/Fe₃O₄-on-ZIF90NH₂, Pd/ Fe₃O₄-on-ZIF90NH₂-NP and Pd/Fe₃O₄-on-MAF-66

The MW tubes were charged by PdCl₂, MOF materials, and [BMIm]NTf₂ in a glovebox; the mixture was processed in the MW reactor (see the Methods section on p.33; the quantities of the reactants and the reaction parameters are summarized in Table S5). After the treatment and cooling, the tubes were returned to the glove box and Fe₂(CO)₉ was added. The MW-treatment was repeated, followed by a standard work up with 4 ml of CH₃CN used during each of the three washing cycles per 1 g of the initially used ionic liquid (Methods section).



Fig. S51 Photos demonstrating the ferromagnetism of the Pd/Fe₃O₄-on-ZIF8-NP after washing in the MW-tube via the action of the magnet (the black layer near the cube-shaped magnet is the sample with the magnetic stirring bar on top of it). The photo is taken on a sample under inert atmosphere, but the ferromagnetism is retained in the air for days at least (seemingly indefinite time).

Analytcs

TEM

Pd-on-ZIF8-NP (1-st stage towards Pd/Fe₃O₄-on-ZIF-8-NP)

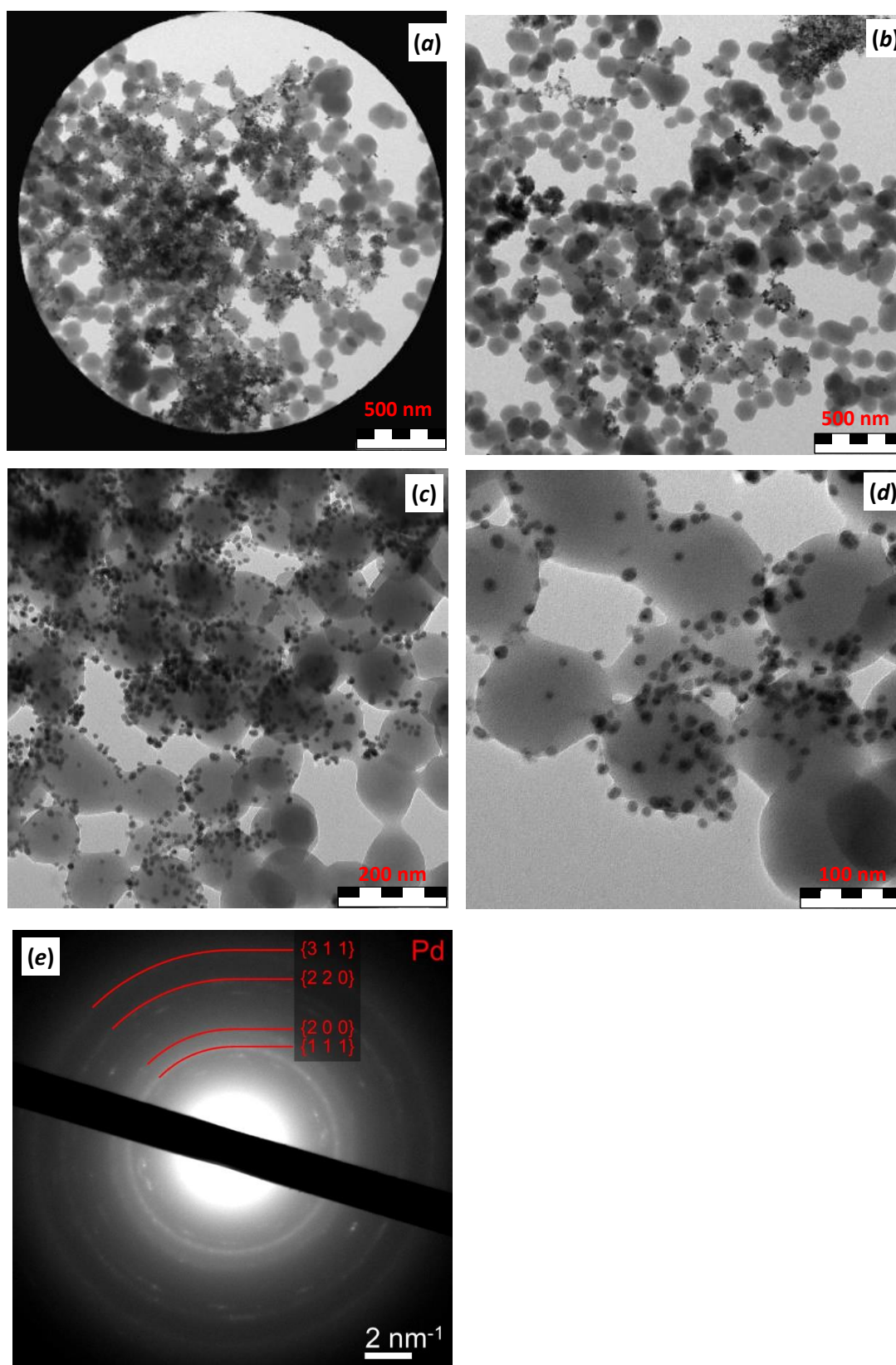


Fig. S52 (a-d) TEM images of Pd-on-ZIF8-NP [Pd: $11\pm 2\ \text{nm}$; ZIF-8: $113\pm 17\ \text{nm}$]; SAED.

Pd/Fe₃O₄-on-ZIF8-NP

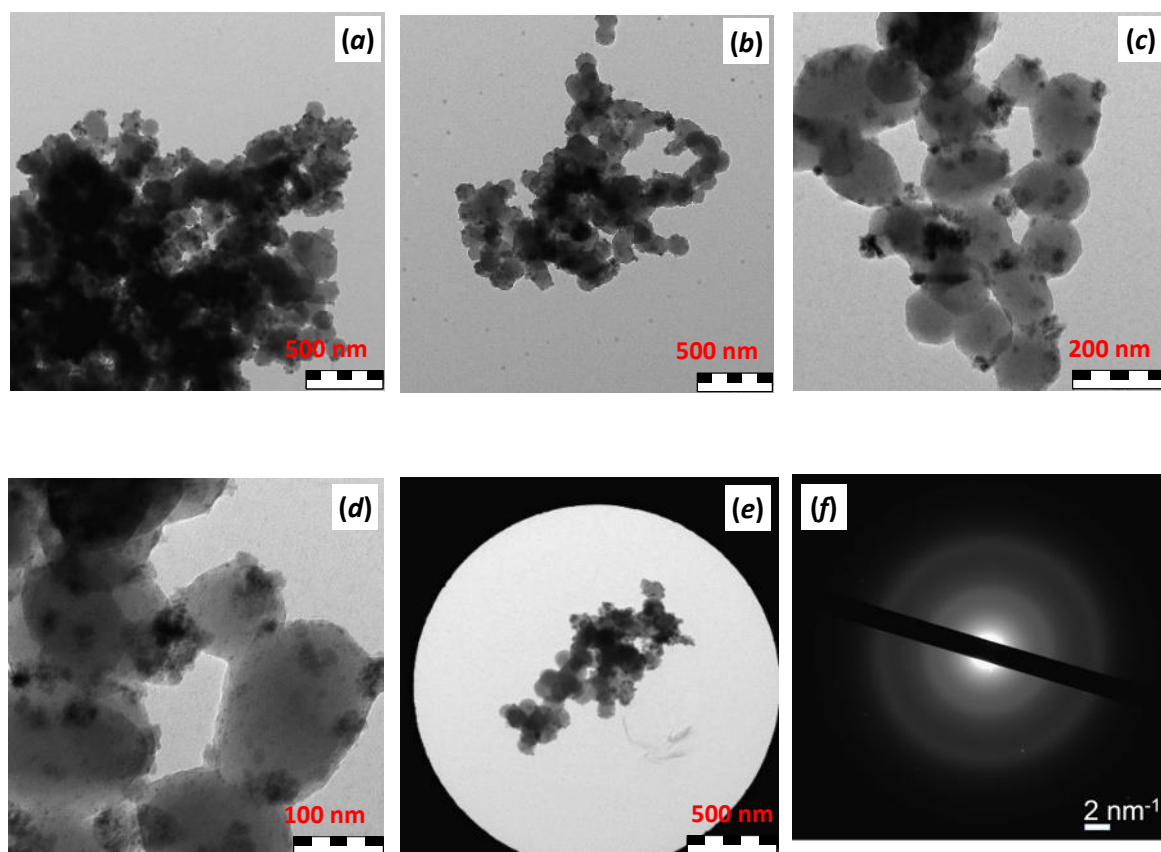


Fig. S53 (a-d) TEM images of Pd/Fe₃O₄-on-ZIF8-NP [Pd: 11±2 nm; Fe: could not be reliably determined due to low contrast; ZIF-8: 113±17 nm]; (f) SAED.

Pd-on-ZIF-90-NH₂ (1-st stage towards Pd/Fe₃O₄-on-ZIF-90-NH₂)

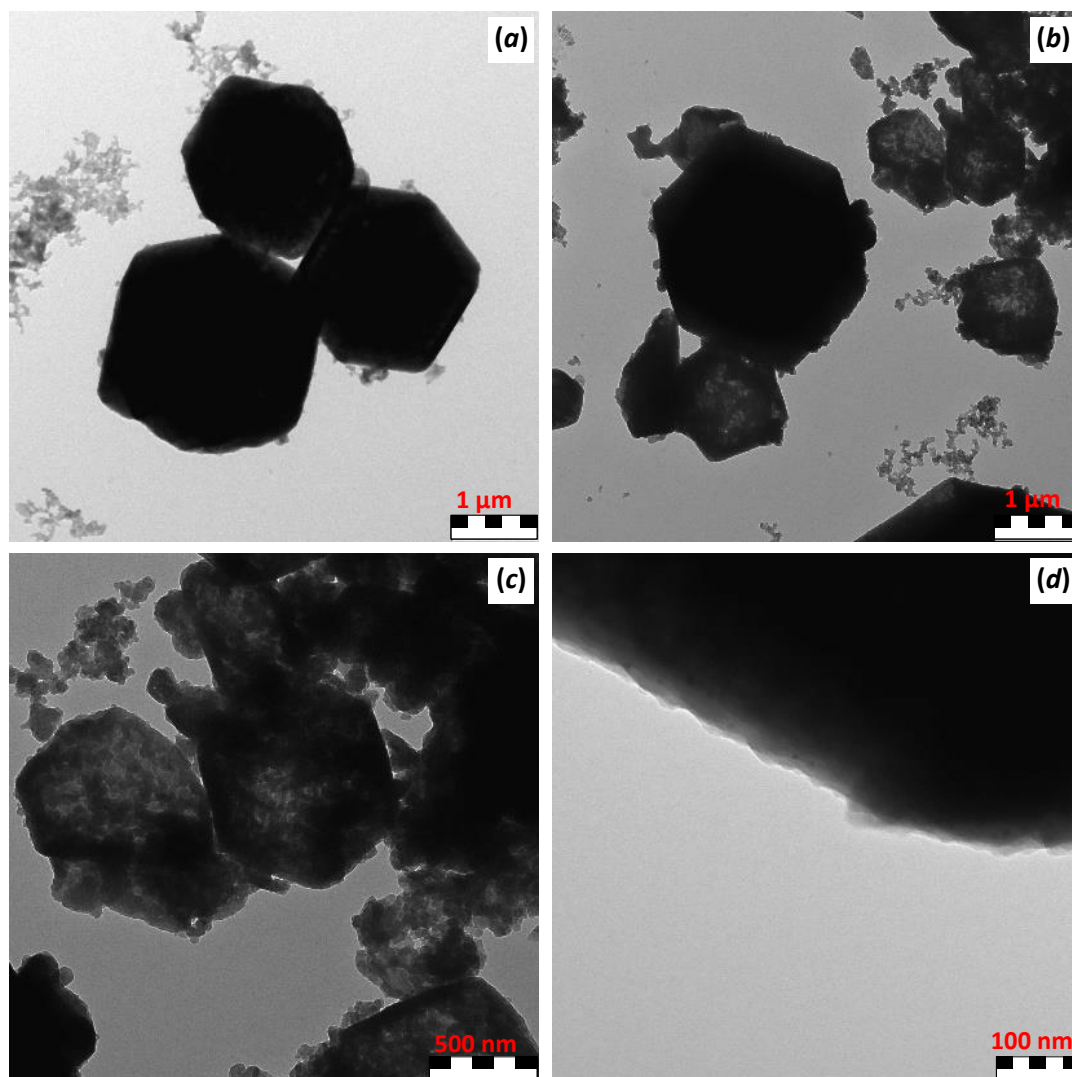


Fig. S54 (a-d) TEM images of Pd-on-ZIF-90-NH₂ [Pd: 6 ± 1 nm; ZIF-90-NH₂: 2.4 ± 0.6 μm].

Pd/Fe₃O₄-on-ZIF-90-NH₂

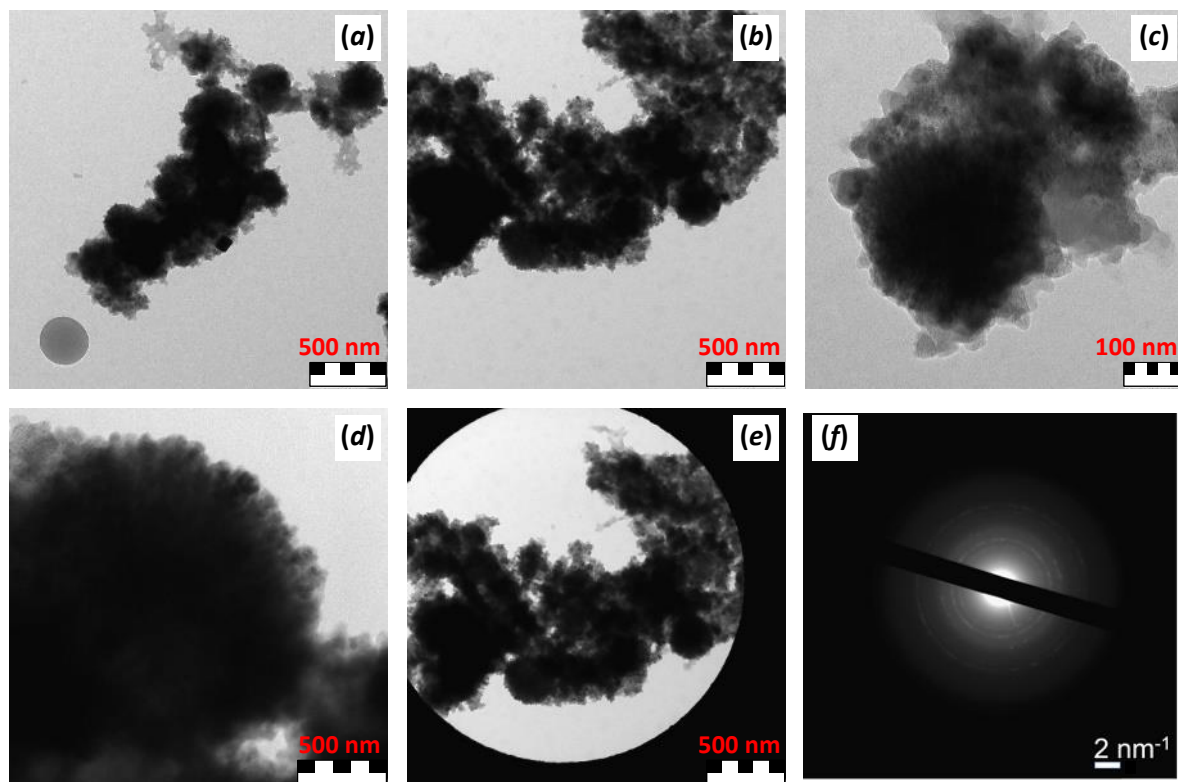


Fig. S55 (a-e) TEM images of Pd/Fe₃O₄-on-ZIF90NH₂ [Pd: 6±1 nm; Fe: could not be reliably determined due to low contrast; ZIF-90-NH₂: 2.4±0.6 μm]; (f) SAED.

Pd-on-ZIF90NH₂-NP (1-stage towards Pd/Fe₃O₄-on-ZIF90NH₂-NP)

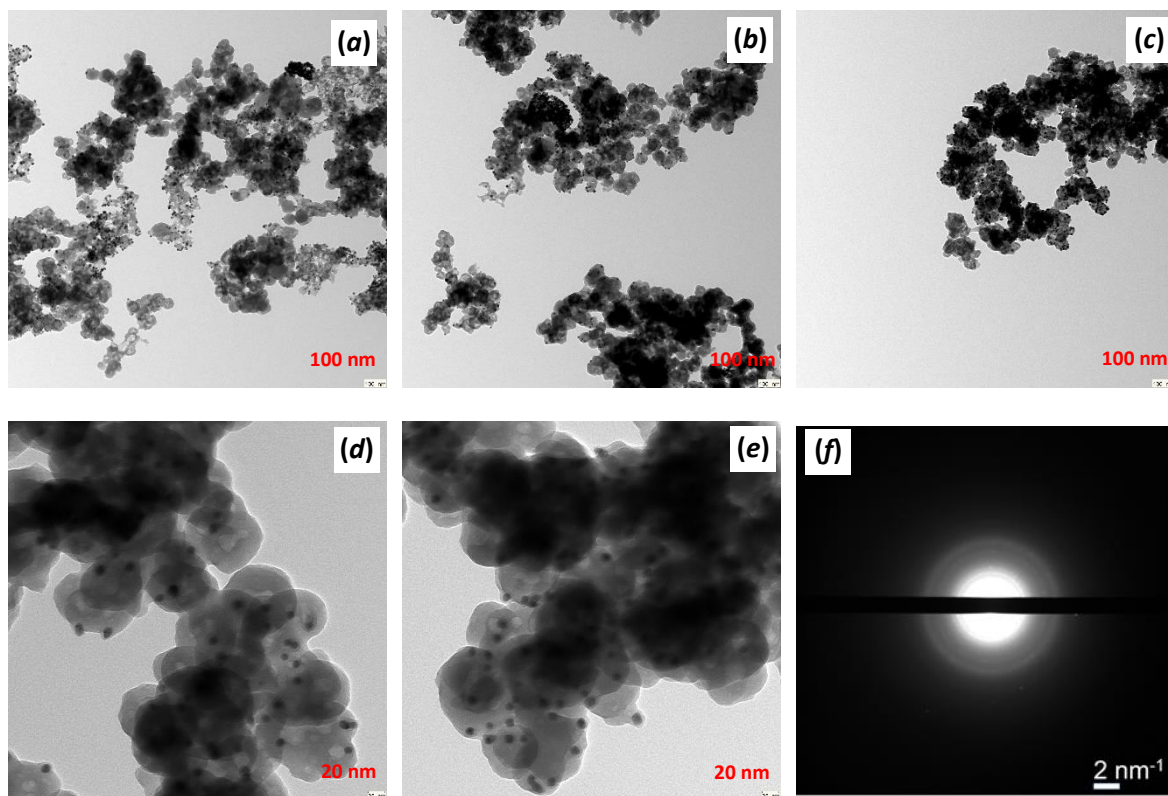


Fig. S56 (a-e) TEM images of Pd-on-ZIF90NH₂-NP [Pd: 10±3 nm; ZIF-90-NH₂-NP: 74±12 nm]; (f) SAED

Pd/Fe₃O₄-on-ZIF90NH₂-NP (2-stage towards Pd/Fe₃O₄-onZIF90NH₂-NP)

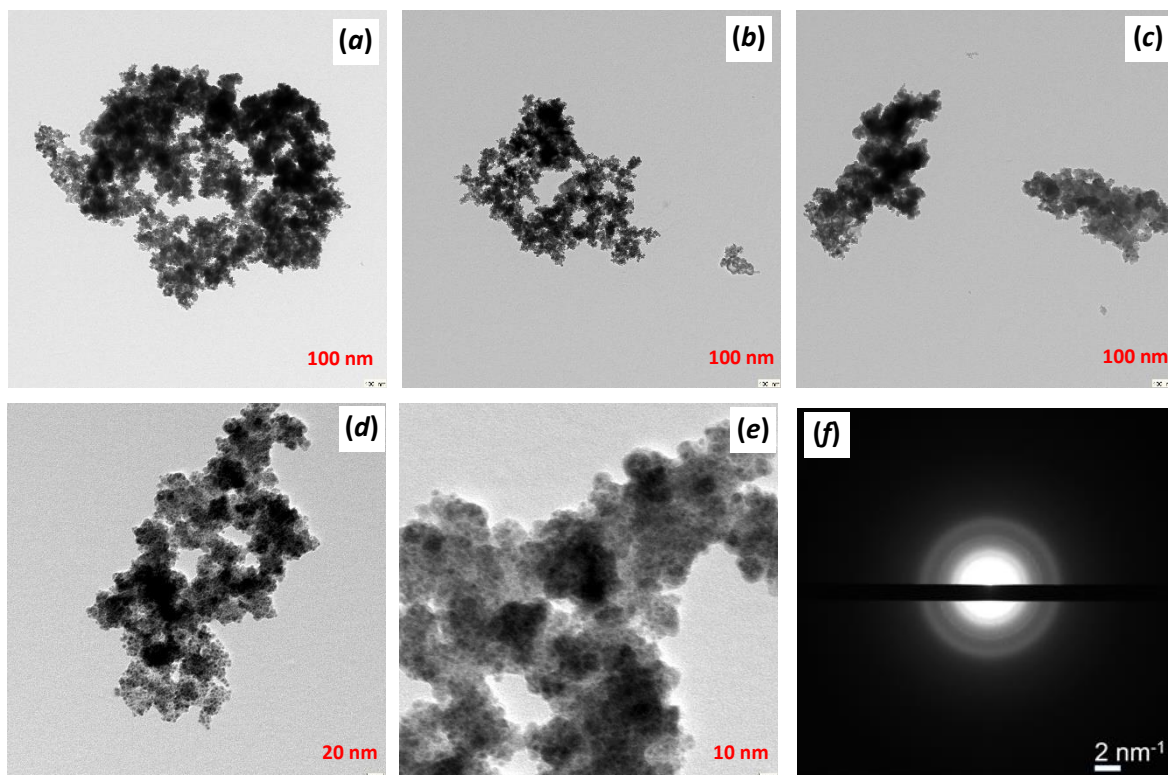


Fig. S57 (a-e) TEM images of Pd-Fe-on-ZIF90NH₂-NP [Pd: 10±3 nm; Fe: cannot be reliably determined due to low contrast; ZIF-90-NH₂-NP: 70±22 nm]; (f) SAED.

Pd-on-MAF-66 (1-st stage towards Pd/Fe₃O₄-on-MAF-66)

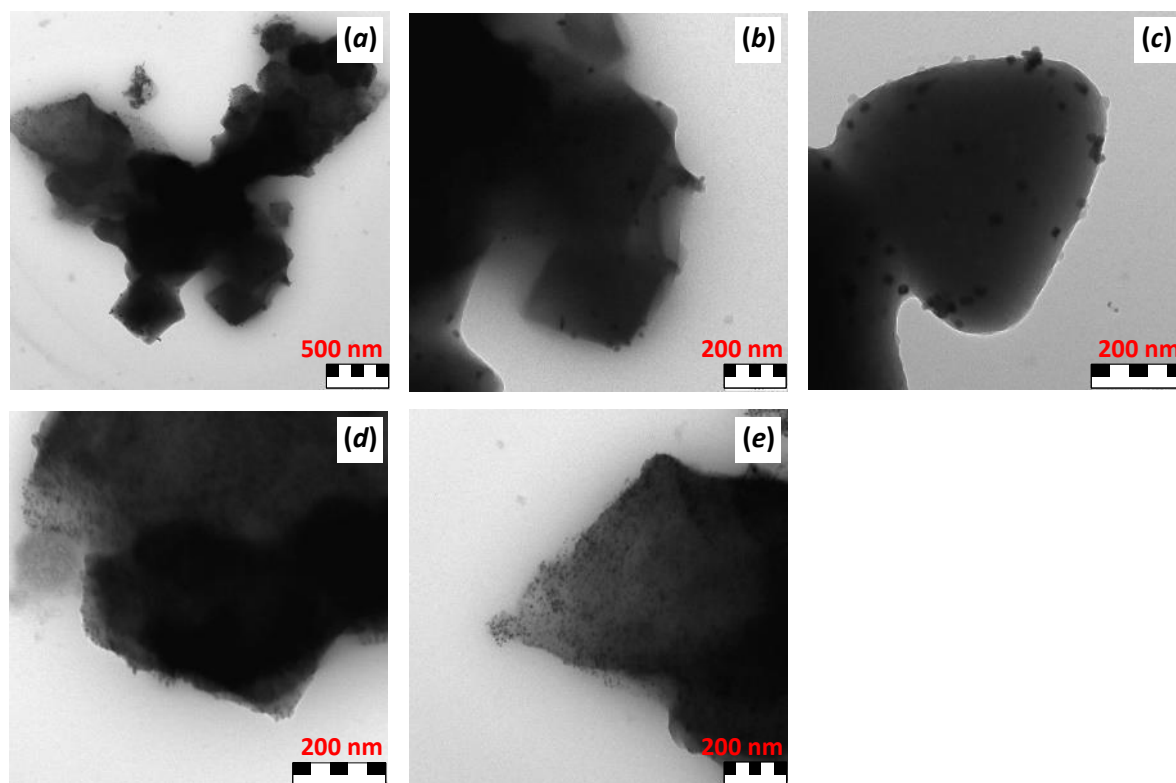


Fig. S58 (a-e) TEM images of Pd-on-MAF66 [Pd: 8 ± 5 nm; MAF-66: 430 ± 180 nm]; f) SAED.

Pd/Fe₃O₄-on-MAF-66

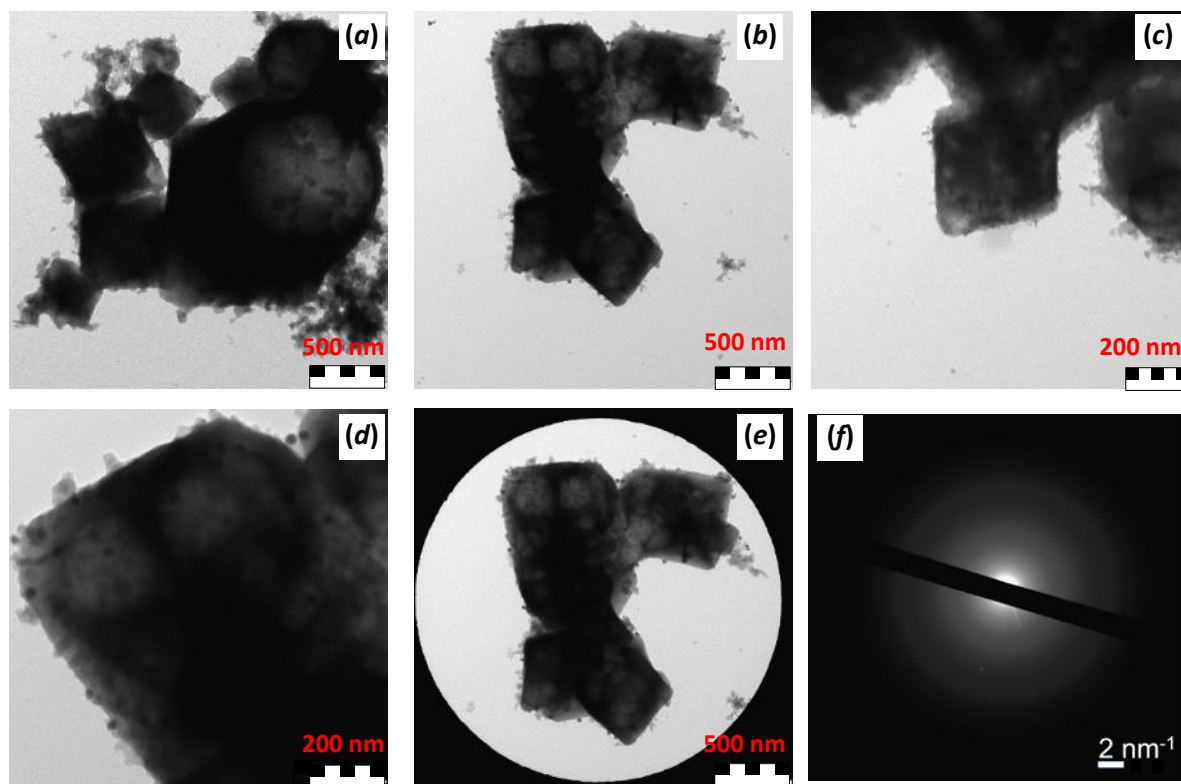


Fig. S59 (a-e) TEM images of Pd/Fe₃O₄-on-MAF-66 [Pd: 8±5 nm; Fe: could not be reliably determined due to low contrast; MAF-66: 430±180 nm]; (f) SAED.

STEM and EDX element mapping

Pd/Fe₃O₄-on-ZIF8-NP

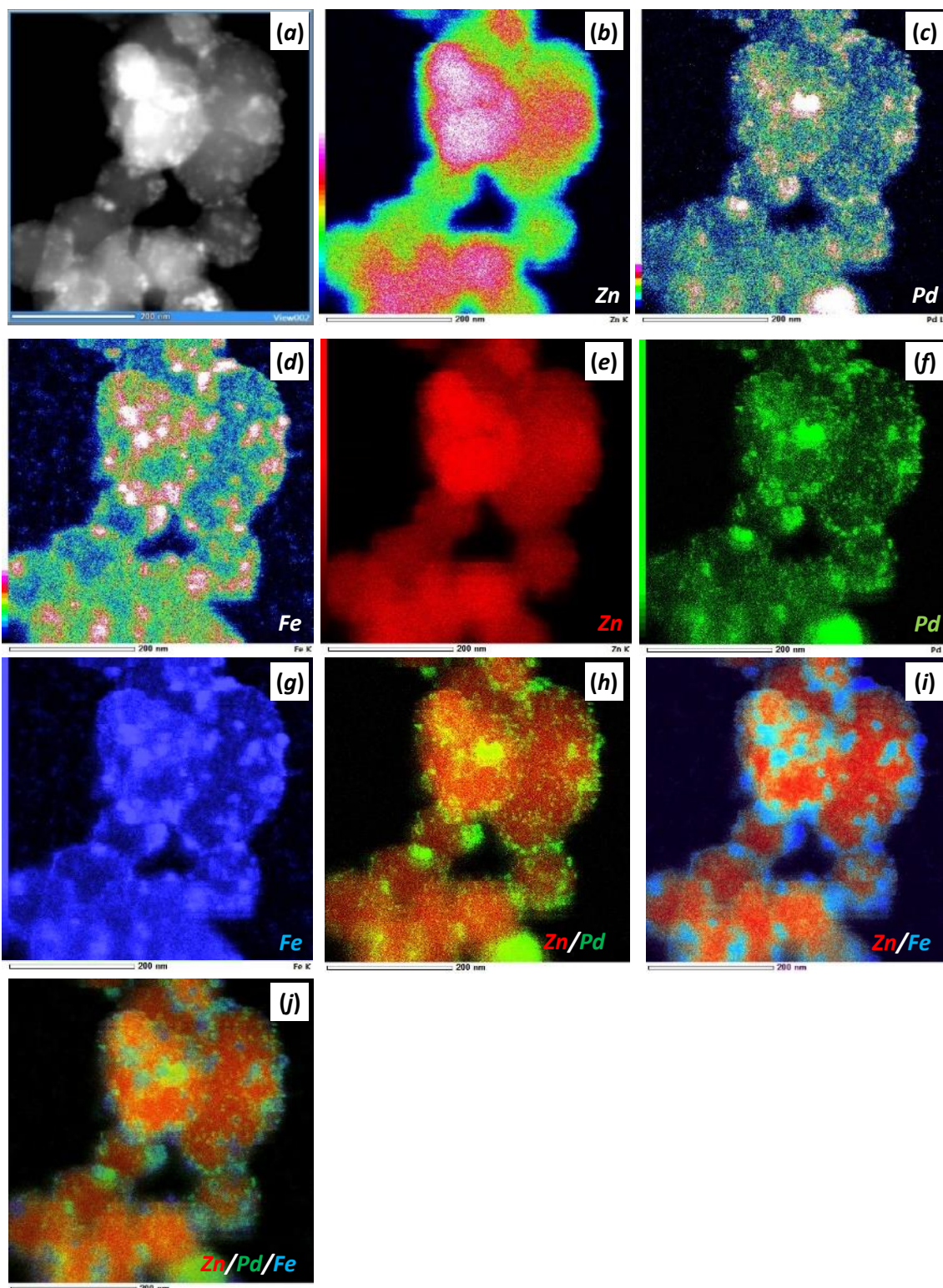


Fig. S60 (a) STEM image Pd/Fe₃O₄-on-ZIF8-NP; (b-k) TEM-EDX element mappings for Zn, Pd and Fe and their combinations using different approaches (200 nm scalebar): (b-d) the color-based mapping, where the concentration is represented by the color's wavelengths: [black = minimum]-blue-...-red-[white = maximum]]; (e-j) the color saturation based mapping, where the concentration is represented by the color's saturation, with black and white corresponding to the minimum and maximum concentrations.

Pd/Fe₃O₄-on-ZIF90-NP

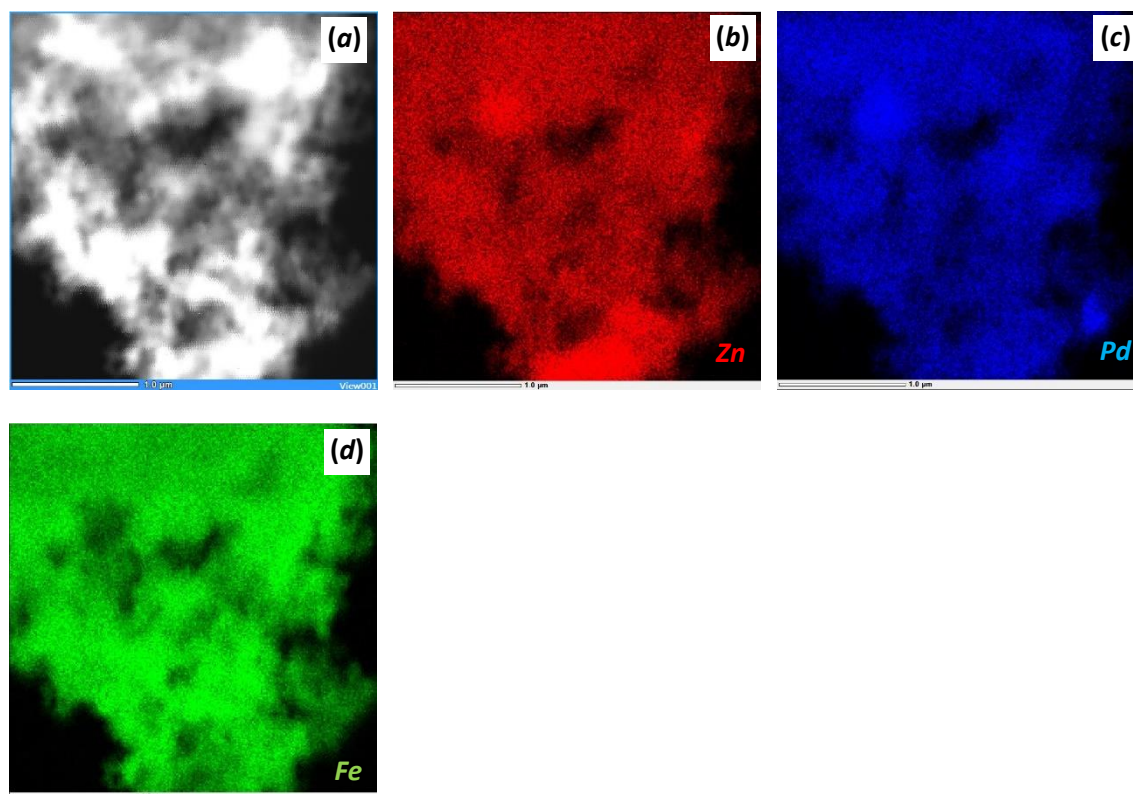


Fig. S61 (a) STEM image Pd/Fe₃O₄-on-ZIF90-NH₂-NP with black and white corresponding to the minimum and maximum concentrations, followed by (b-d) TEM-EDX element mappings for Zn, Pd, and Fe (1.0 μm scalebar) with color saturation increasing with concentration (pure color corresponds to maximum and black to minimum concentrations).

SEM and EDX element mapping/composition

Pd-on-ZIF8-NP (1-st stage towards Pd/Fe₃O₄-on-ZIF8-NP)

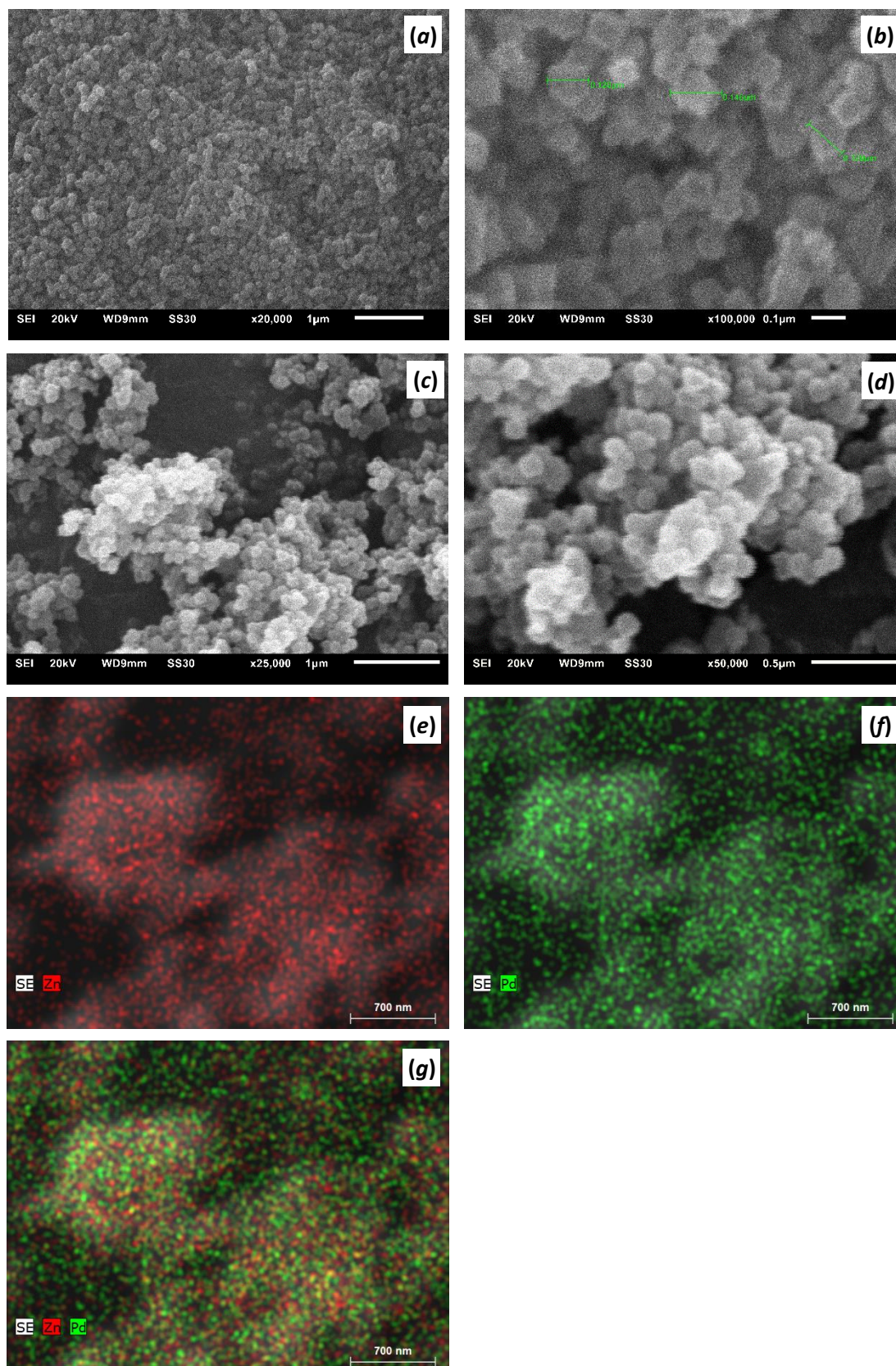


Fig. S62 SEM micrographs of (a,b) the ZIF8-NPs prior to synthesis and (c,d) the resultant Pd-on-ZIF8-NP (first stage towards Pd/Fe₃O₄-on-ZIF8-NP). (e-g) EDX element mapping for Pd/Fe₃O₄-on-ZIF8-NP. **Zn:Pd ratio is 34.3** (outlier, see Table S6 for more explanations).

Pd/Fe₃O₄-on-ZIF8-NP (2-stage towards Pd/Fe₃O₄-on-ZIF8-NP)

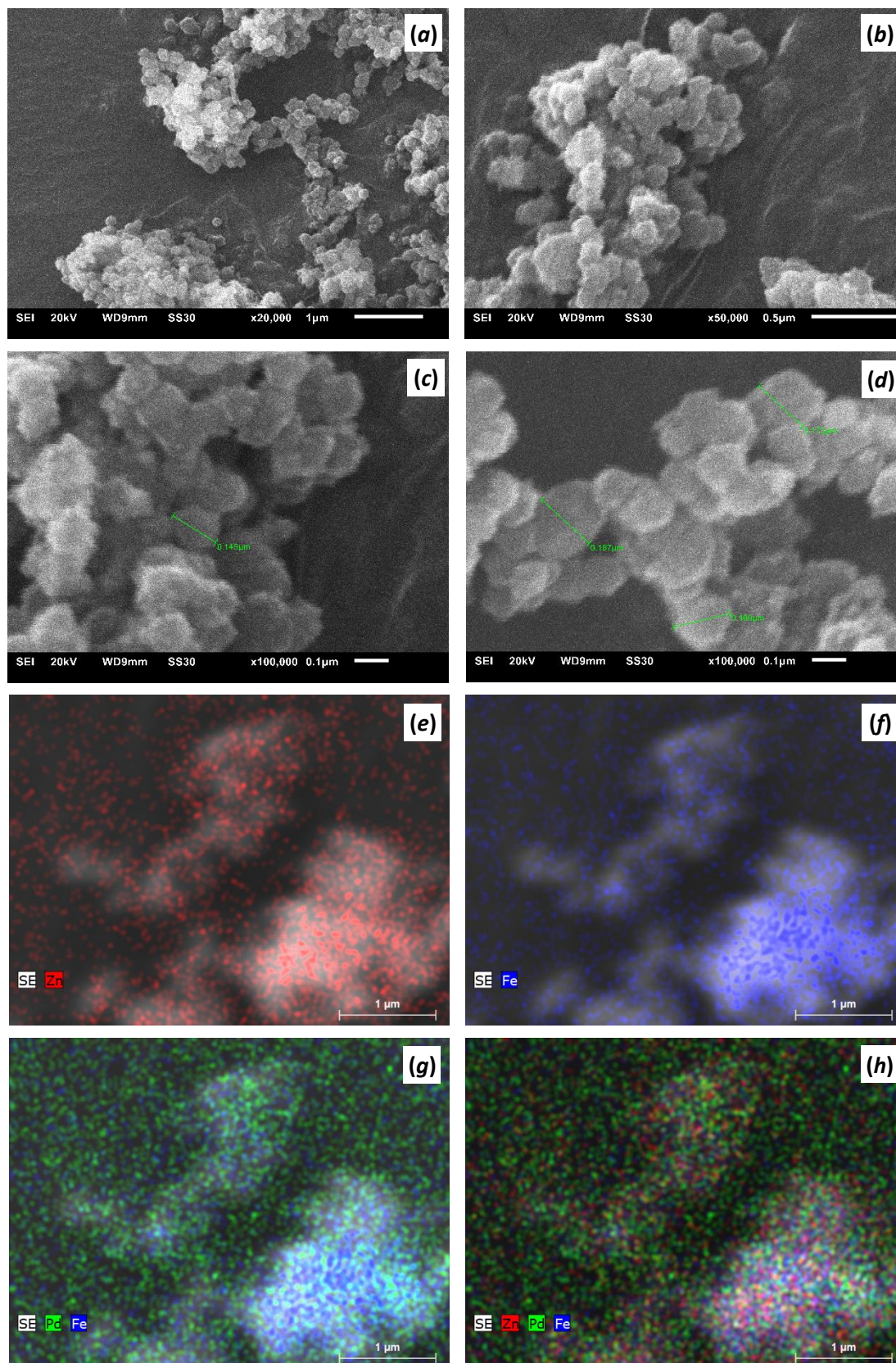


Fig. S63 (a-d) SEM micrographs of Pd/Fe₃O₄-on-ZIF8-NP; (e-h) Zn/Pd/Fe₃O₄-EDX element mapping for Pd/Fe₃O₄-on-ZIF8-NP material; note the uniform distribution on overlay, pane (h). Zn:Pd:Fe ratio is 5.34:6.93:1.

Pd-on-ZIF90-NH₂ (1-st stage towards Pd/Fe₃O₄-on-ZIF90-NH₂)

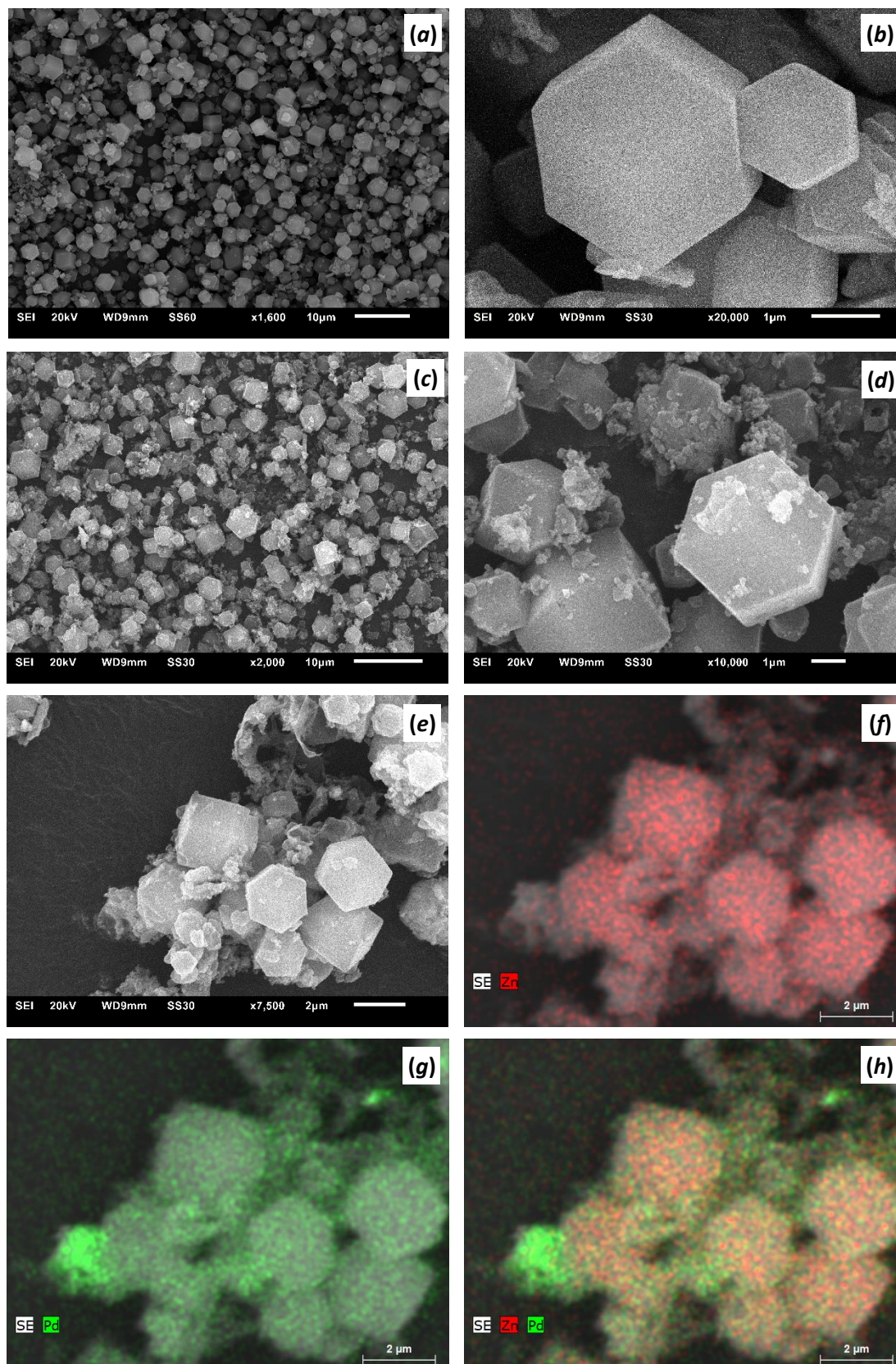


Fig. S64 (a-b) SEM micrographs of ZIF90NH₂; (c-e) SEM micrographs of Pd-on-ZIF90NH₂; (f-h) Zn/Pd-EDX element mapping for Pd-on-ZIF90NH₂ material. **Zn:Pd ratio is 5.22** (outlier, see Table S6 for more explanations).

Pd/Fe₃O₄-on-ZIF90NH₂ (2-nd stage towards Pd/Fe₃O₄-on-ZIF90NH₂)

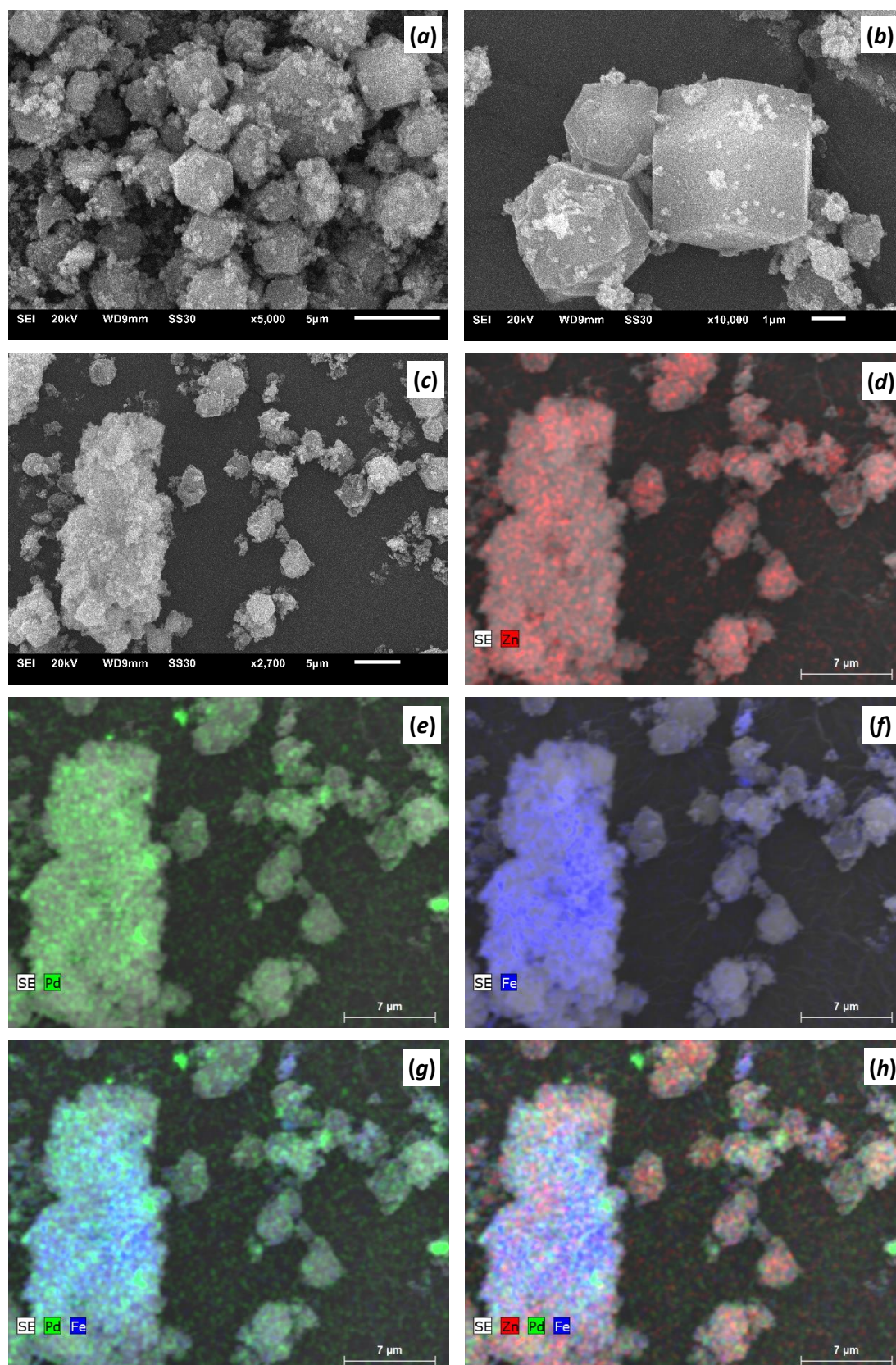


Fig. S65 (a-c) SEM micrographs of Pd/Fe₃O₄-on-ZIF90NH₂; (d-h) Zn/Pd/Fe₃O₄-EDX element mapping for Pd/Fe₃O₄-on-ZIF90NH₂ material. Note the generally even elemental distribution with some spots of locally increased concentration of Pd and Fe, overlay pane (h) (taken from a representative average fragment). The irregularities are more typical for large particles, with lower surface area and hence lesser possibilities for uniform deposition. **Zn:Pd:Fe ratio is 2.43:1:6.87.**

Pd-on-ZIF90NH₂-NP (1-st stage towards Pd/Fe₃O₄-on-ZIF90NH₂-NP)

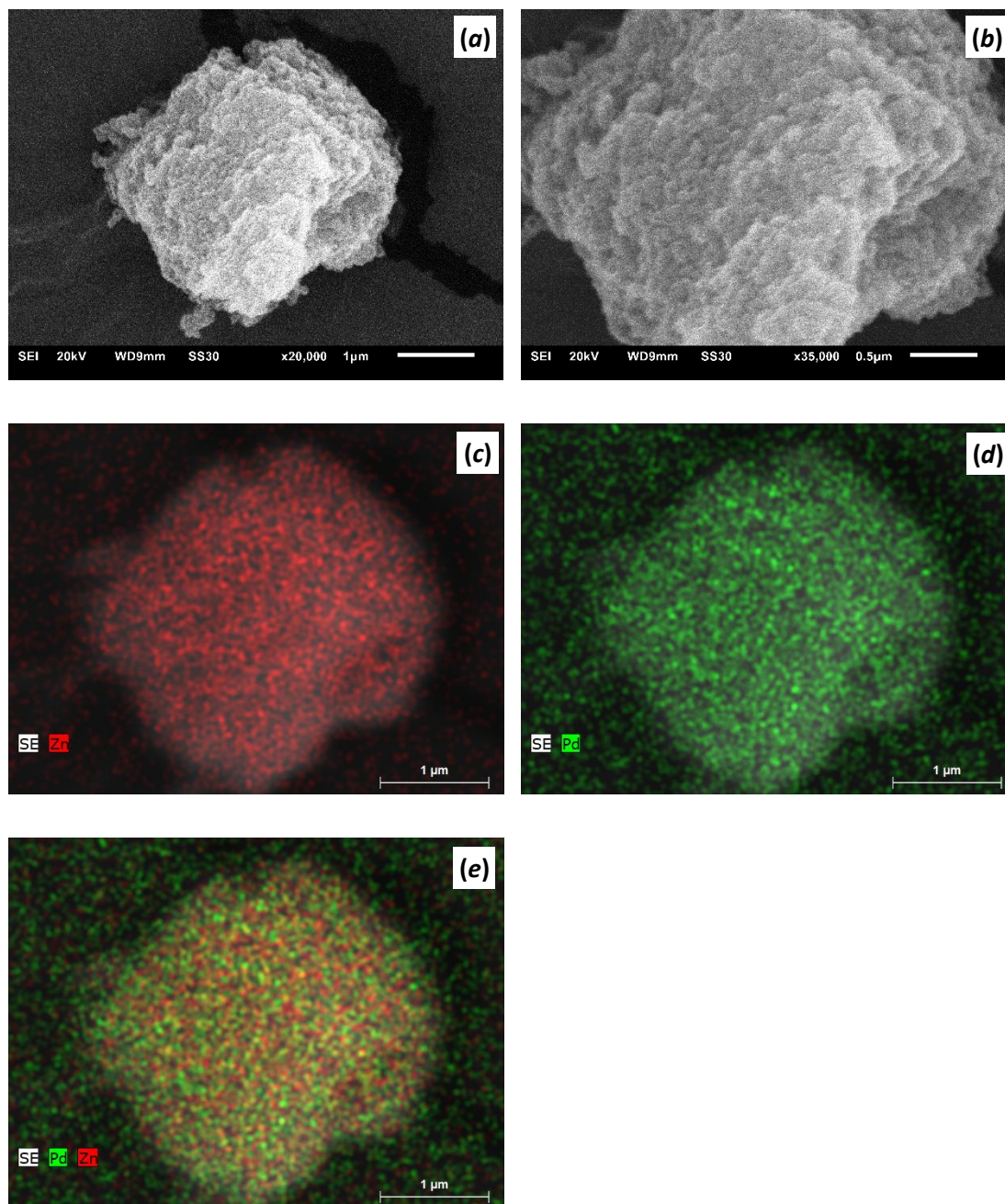


Fig. S66 (a-b) SEM micrographs of Pd-on-ZIF90NH₂-NP (first stage of Pd/Fe₃O₄-on-ZIF90NH₂-NP); (c-e) Zn/Pd-EDX element mapping for Pd/Zn-on-ZIF90NH₂-NP material. **Zn:Pd ratio is 17.1.**

Pd/Fe₃O₄-on-ZIF90NH₂-NP (2-nd stage towards Pd/Fe₃O₄-on-ZIF90NH₂-NP)

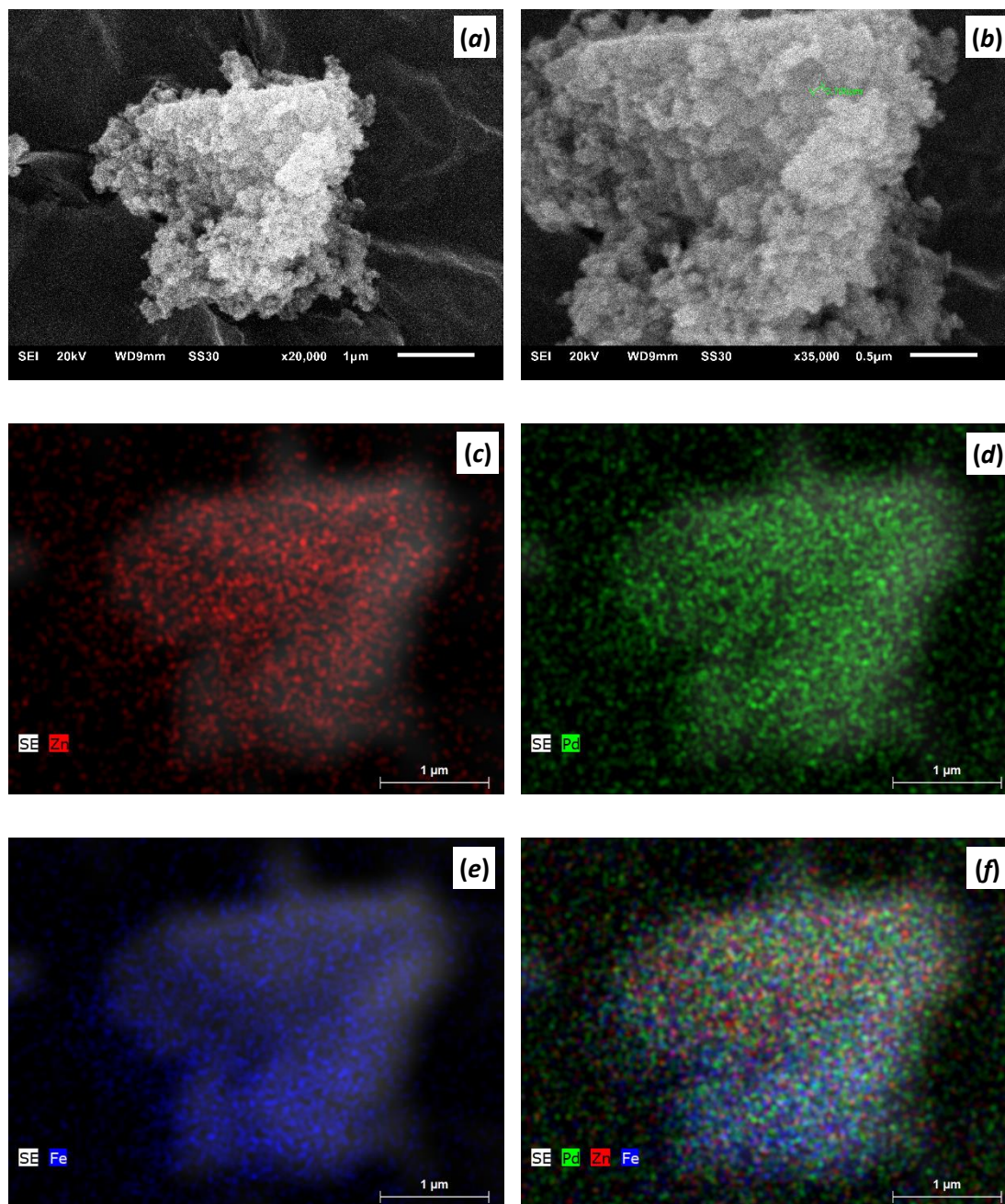


Fig. S67 (a-b) SEM micrographs of Pd/Fe₃O₄-on-ZIF90NH₂-NP; (c-f) Zn/Pd/Fe₃O₄-EDX element mapping for Pd/Fe₃O₄-on-ZIF90NH₂-NP material; note the even elemental distribution on the overlay, pane f. **Zn:Pd:Fe ratio is 4.49:1:6.11.**

Pd-on-MAF66 (1-st stage towards Pd/Fe₃O₄-on-MAF66)

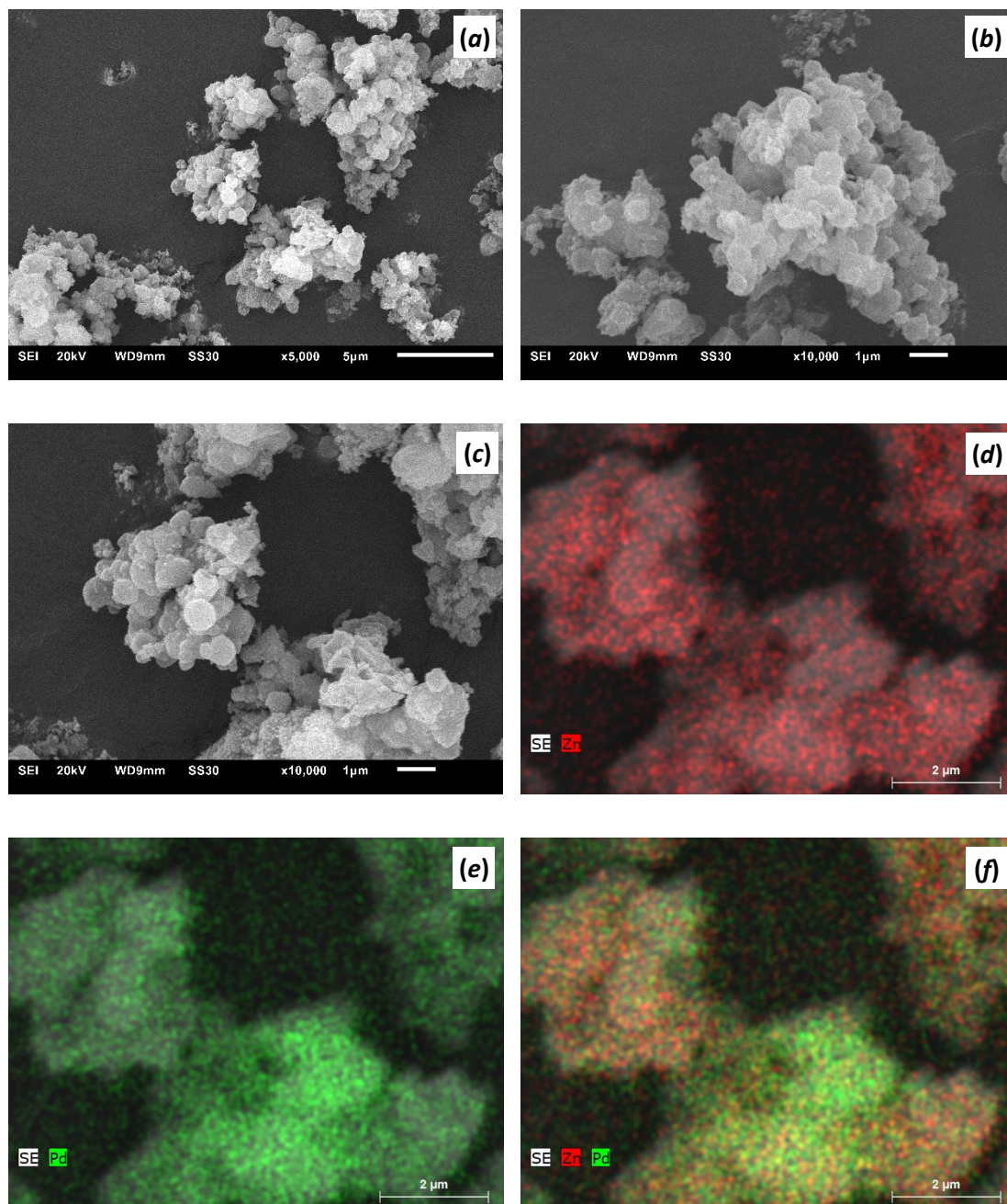


Fig. S68 (a-c) SEM micrographs of Pd-on-MAF66; (d-f) Zn/Pd-EDX element mapping for Pd-on-MAF66. **Zn:Pd ratio is 3.04.**

Pd/Fe₃O₄-on-MAF66 (2-nd stage towards Pd/Fe₃O₄-on-MAF66)

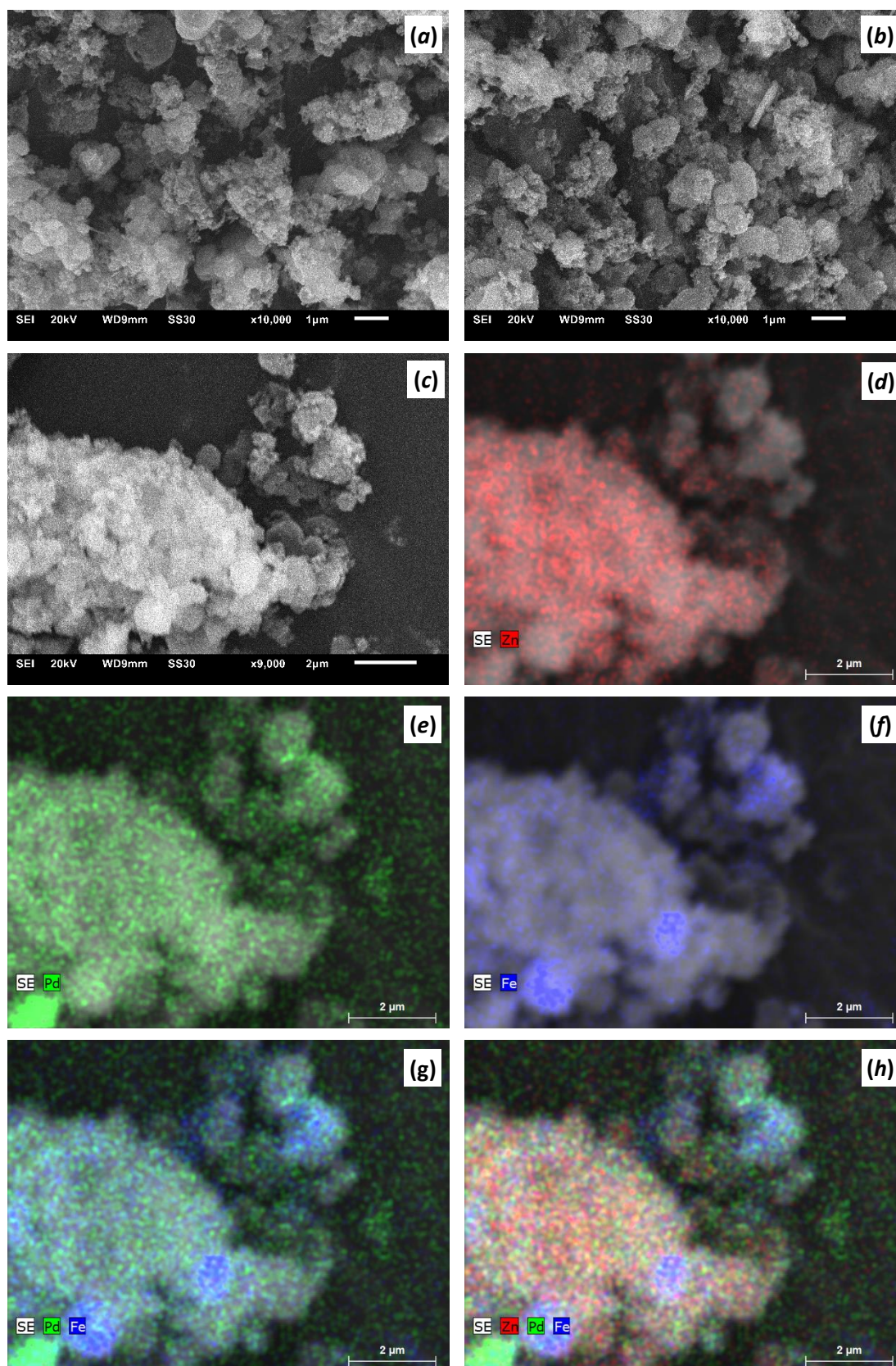


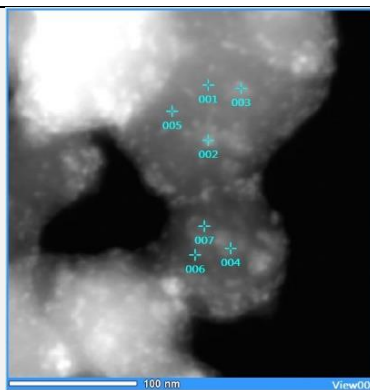
Fig. S69 (a-c) SEM micrographs of Pd/Fe₃O₄-on-MAF66-NP; (c-h) Zn/Pd/Fe₃O₄-EDX element mapping for Pd/Fe₃O₄-on-MAF66-NP. Note the generally even elemental distribution with some spots of locally increased concentration of Pd and Fe, overlay pane h (taken from a representative average fragment). The irregularities are more typical for large particles, with lower surface area and hence lesser possibilities for uniform deposition. **Zn:Pd:Fe ratio is 8.35:1:3.61.**

AAS and S(T)EM/EDX based Pd and Fe content comparison

Sample	AAS Pd-content [% _{atom}]	AAS Fe-content [% _{atom}]	SEM-EDX Pd-content [% _{atom}]	SEM-EDX Fe-content [% _{atom}]	SEM-EDX Zn-content [% _{atom}]
Pd/Fe ₃ O ₄ -on-ZIF8-NP	14.65	9.39	5.74	39.78	30.64
Pd/Fe ₃ O ₄ -on-ZIF90NH ₂	9.47	10.58	8.13	55.88	19.81
Pd/Fe ₃ O ₄ -on-ZIF90NH ₂ -NP	5.08	18.68	7.24	44.21	32.52
Pd/Fe ₃ O ₄ -on-MAF66	8.79	11.13	5.26	19.00	43.94

Tab. S6 Sampling problem on the example of STEM result for Pd/Fe₃O₄-on-ZIF8-NP: the local variation could be relatively high (sometimes evident outliers were found due to small amount of measured points; this situation is noted explicitly in the image captions). Accordingly, AAS-data were used for the evaluation of the catalytic results.

STEM-EDX results on Pd/Fe₃O₄-on-ZIF8-NP



Point-Nr.	Pd-content [% _{atom}]	Fe ₃ O ₄ -content [% _{atom}]	Zn-content [% _{atom}]
1	1.27	5.27	40.69
2	15.36	15.05	30.17
3	2.93	6.32	41.12
4	6.90	10.33	36.81
5	6.37	4.35	44.13
6	5.91	9.34	40.91
7	6.33	13.01	40.49
∅ (average)	6.44	9.09	39.19

PXRD

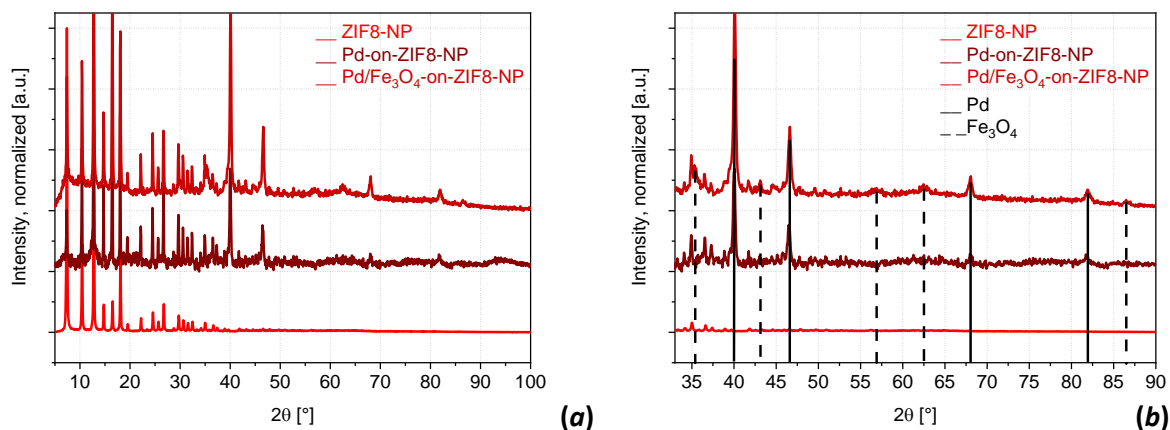


Fig. S70 Comparison of the PXRD patterns for the Pd/Fe₃O₄-on-ZIF8-NP and Pd-on-ZIF8-NP with the ZIF8-NP support material and the simulated PXRDs for Pd-metal and Fe₃O₄ crystalline phases: (a) full pattern, (b) expansion. Note the evident crystallinity of the Pd- and near-complete amorphicity of the Fe₃O₄ constituents (the peaks corresponding to the latter could be, however, discerned as very weak and broad peaks).

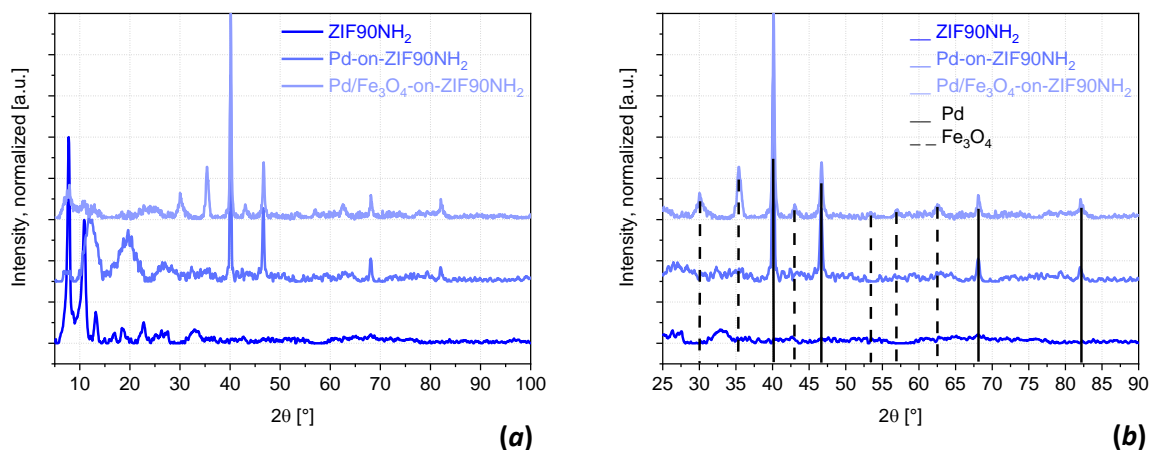


Fig. S71 Comparison of the PXRD patterns for the Pd/Fe₃O₄-on-ZIF90NH₂ material: (a) full pattern, (b) expansion. Note the evident crystallinity of the Pd- and the near-complete amorphicity of the Fe₃O₄ constituents (the peaks corresponding to the latter could be, however, discerned as a very weak and broad peaks).

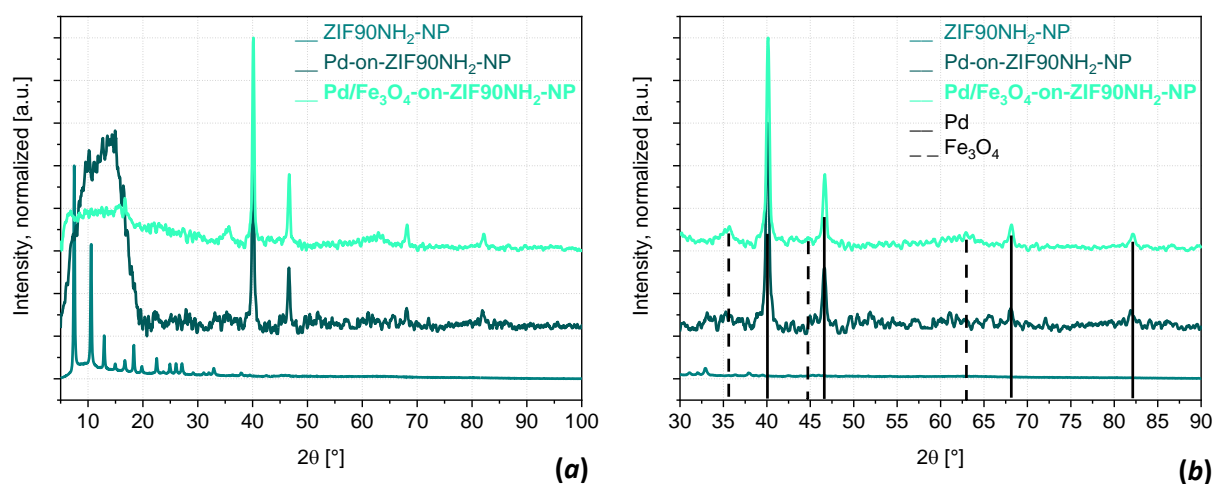


Fig. S72 Comparison of the PXRD patterns for the Pd/Fe₃O₄-on-ZIF90NH₂-NP and Pd-on-ZIF90NH₂-NPs: (a) full pattern, (b) expansion. Note the loss of crystallinity by the support, very weak crystallinity of the Pd- and amorphicity of the Fe₃O₄ constituents.

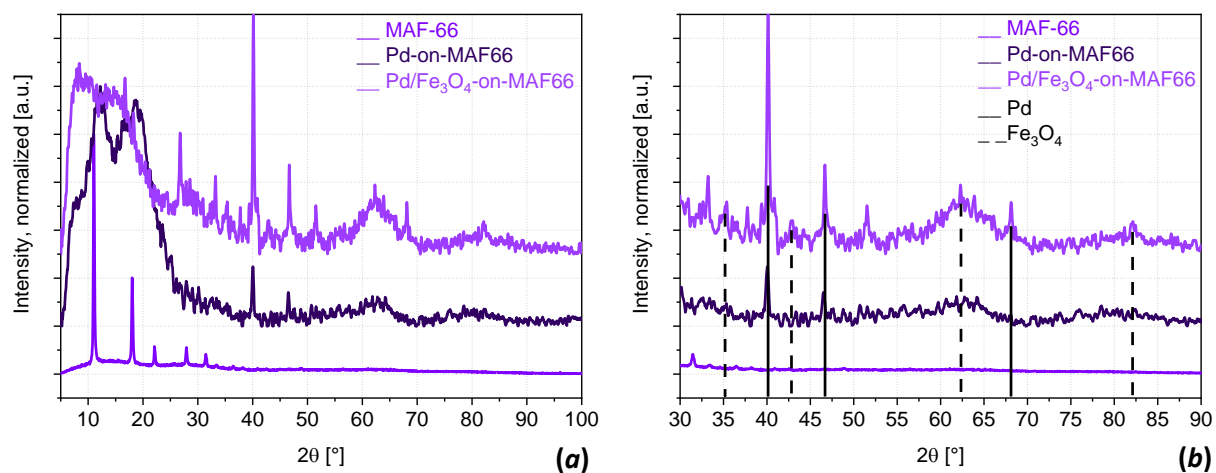


Fig. S73 Comparison of the PXRD patterns for the Pd/Fe₃O₄-on-MAF66-NP and Fe₃O₄-on-MAF66-NPs: (a) full pattern, (b) expansion. Note loss of the crystallinity by the support, very weak crystallinity of the Pd- and amorphicity of the Fe₃O₄ constituents.

6.4 Fe₃O₄-/Pd-on-ZIF8-NPs and Fe₃O₄-/Pd-on-ZIF-90-NH₂-NP

General method (analogous to the synthesis of Pd/Fe₃O₄-on-MOF materials, but the stages are reversed): the MW-tubes were charged by [BMIm][NTf₂] (liquid at room temperature) and Fe₂(CO)₉ in a glovebox; the mixture was processed in the MW reactor (see the Methods section on p.33; the quantities of the reactants and the reaction parameters are summarized in Table S5). After the treatment and cooling, the tubes were returned to the glove box and the PdCl₂ was added. The MW-treatment was repeated, followed by a standard workup with 4 ml of CH₃CN used during each of the three washing cycles per 1 g of the initially used ionic liquid (Methods section).

SEM and EDX element mapping/composition

Fe_3O_4 -on-ZIF8-NP (firststage towards Fe_3O_4 /Pd-on-ZIF8-NP)

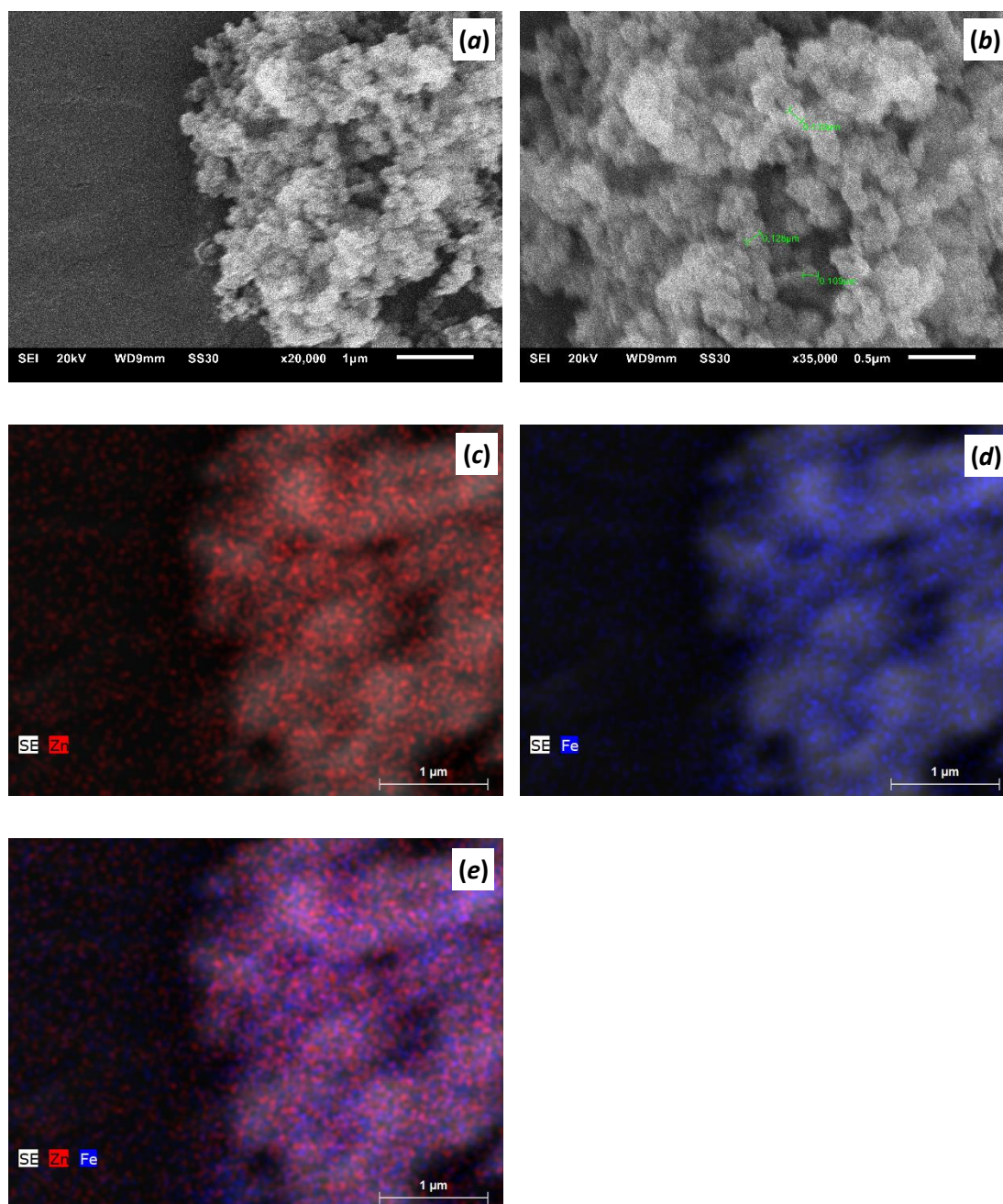


Fig. S74 SEM micrographs of (a,b) Fe_3O_4 -on-ZIF8-NP (1-st stage towards Fe_3O_4 /Pd-on-ZIF8-NP). (c-e) EDX element mapping for Fe_3O_4 -on-ZIF8-NP. Zn:Fe ratio is 1.09.

$\text{Fe}_3\text{O}_4/\text{Pd-on-ZIF8-NP}$ (2-nd stage towards $\text{Fe}_3\text{O}_4/\text{Pd-on-ZIF8-NP}$)

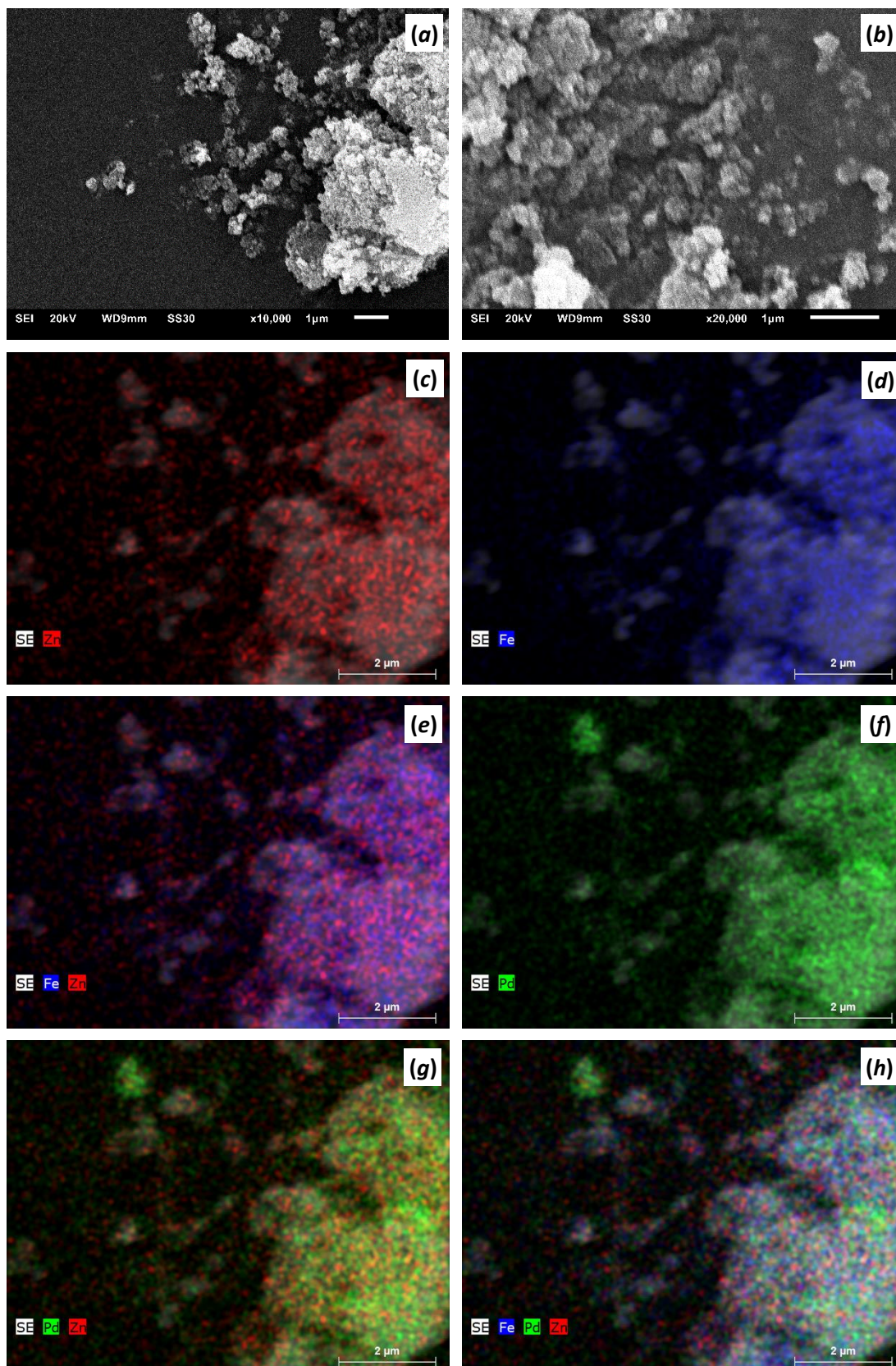


Fig. S75 SEM micrographs of (a,b) $\text{Fe}_3\text{O}_4/\text{Pd-on-ZIF8-NP}$. (c-h) EDX element mapping for $\text{Fe}_3\text{O}_4/\text{Pd-on-ZIF8-NP}$. Zn:Fe:Pd ratio is 1.29:3.61:1.

Fe_3O_4 -on-ZIF90NH₂-NP (1-st stage towards Fe_3O_4 /Pd-on-ZIF90NH₂-NP)

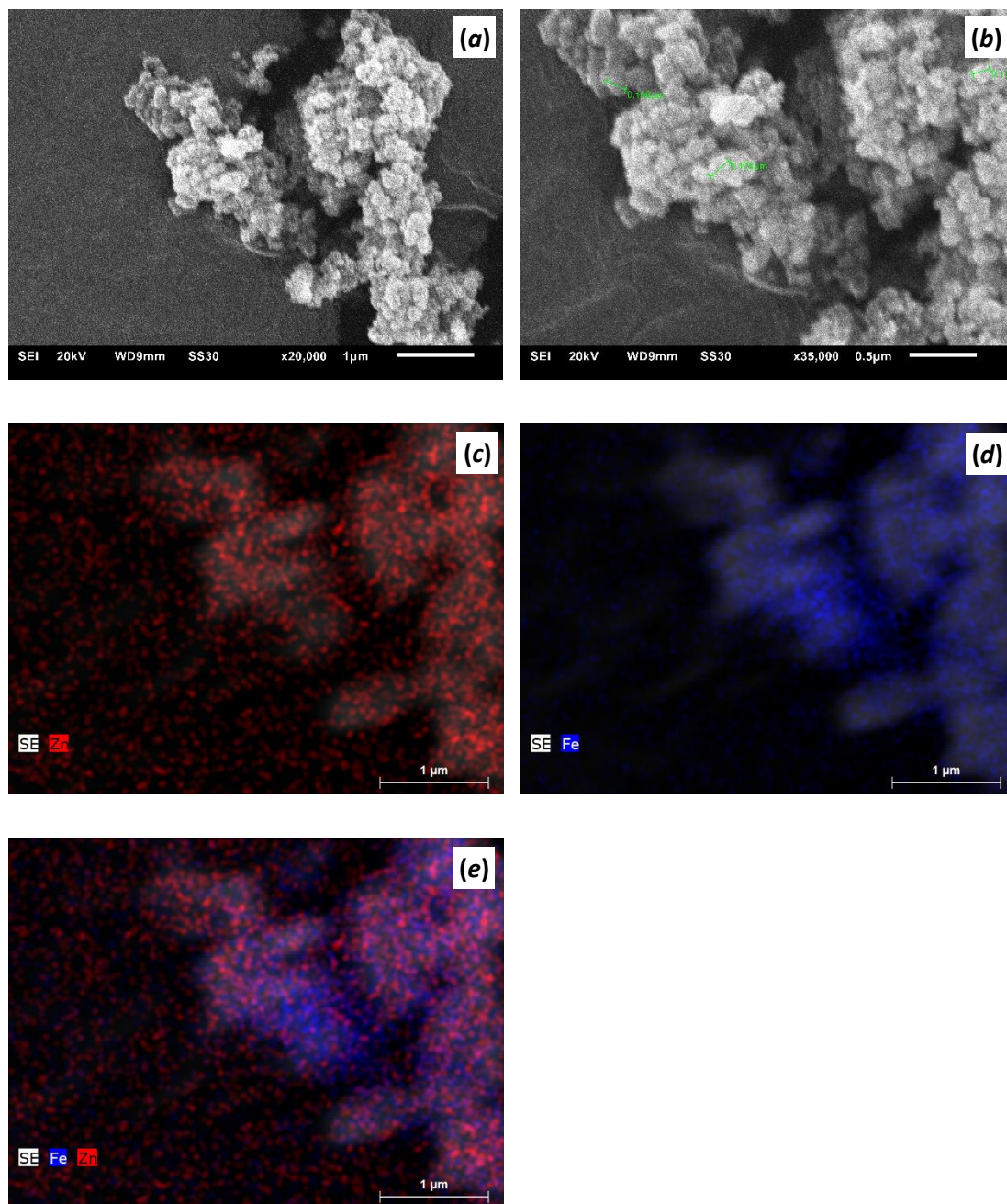


Fig. S76 SEM micrographs of (a,b) Fe_3O_4 -on-ZIF90NH₂-NP. (c-e) EDX element mapping for Fe_3O_4 -on-ZIF90NH₂-NP. Zn:Fe ratio is 0.35 (outlier).

$\text{Fe}_3\text{O}_4/\text{Pd-on-ZIF90NH}_2\text{-NP}$ (2-nd stage towards $\text{Fe}_3\text{O}_4/\text{Pd-on-ZIF90NH}_2\text{-NP}$)

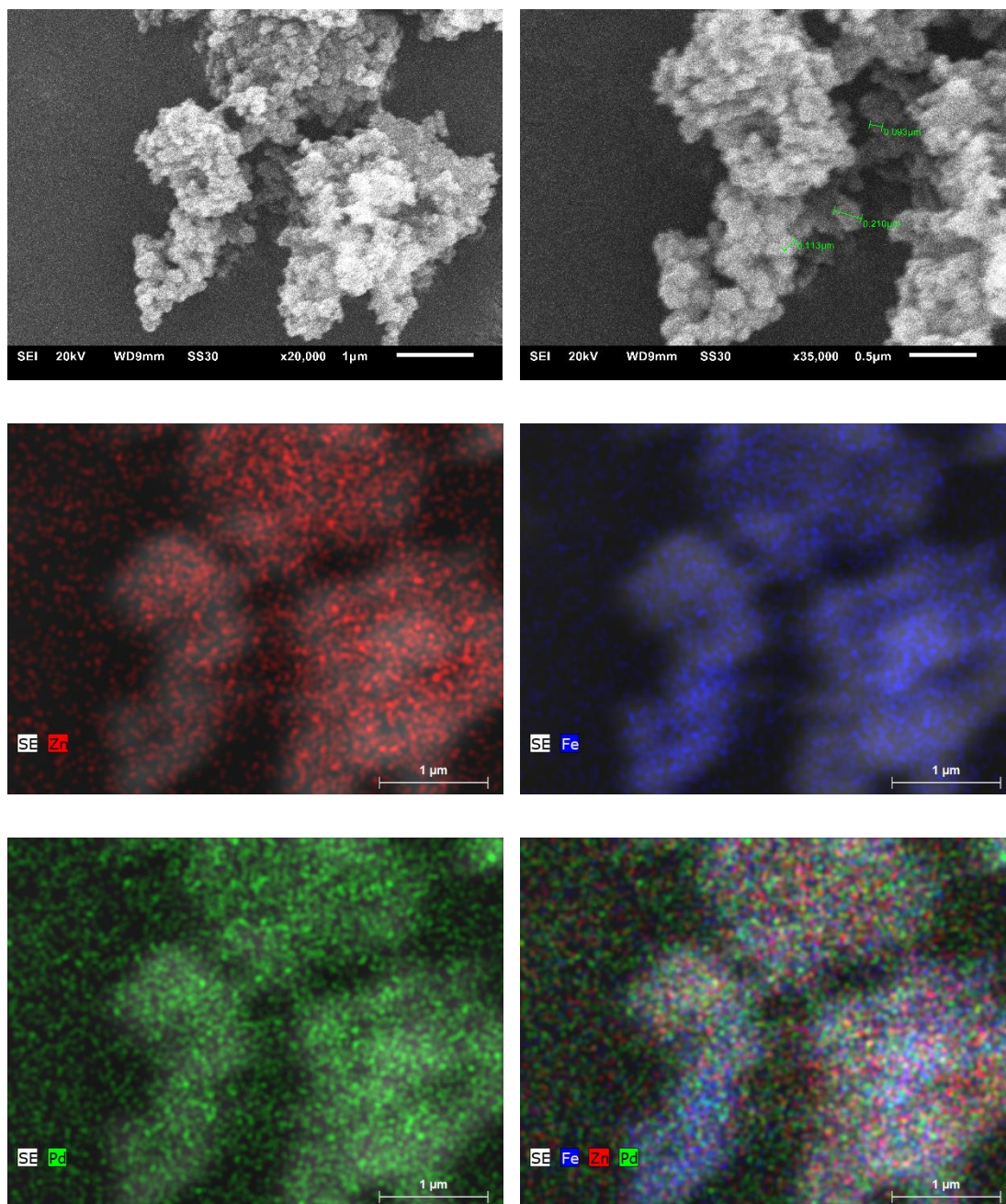


Fig. S77 SEM micrographs of (a,b) $\text{Fe}_3\text{O}_4/\text{Pd-on-ZIF90NH}_2\text{-NP}$. (c-h) EDX element mapping for $\text{Fe}_3\text{O}_4/\text{Pd-on-ZIF90NH}_2\text{-NP}$. **Zn:Fe:Pd ratio is 7.69:10.37:1.**

TEM

Fe_3O_4 -on-ZIF8-NP (1-st stage toward Fe_3O_4 /Pd-on-ZIF8-NP)

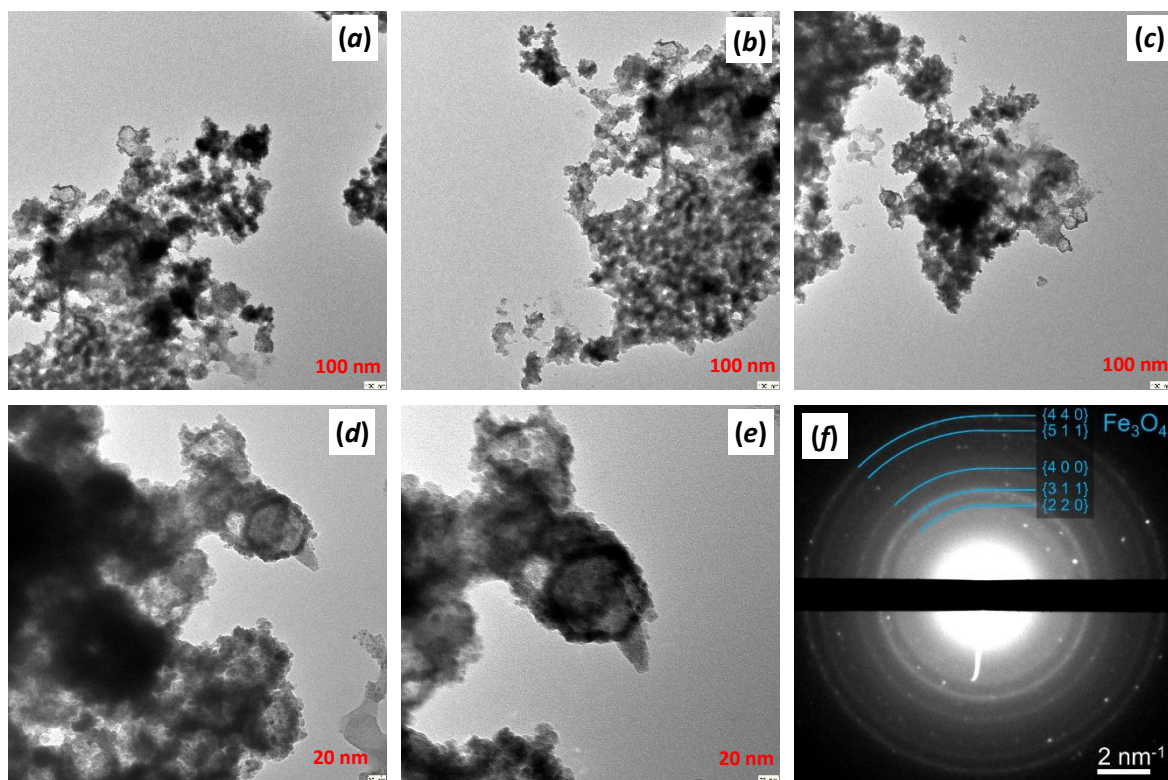


Fig. S78 (a-e) TEM images of Fe_3O_4 -on-ZIF8-NP [Fe: 5 ± 2 or $3?$ nm; ZIF-8: 103.9 ± 16.6 nm]; (f) SAED

$\text{Fe}_3\text{O}_4/\text{Pd-on-ZIF8-NP}$ (2-nd stage toward $\text{Fe}_3\text{O}_4/\text{Pd-on-ZIF8-NP}$)

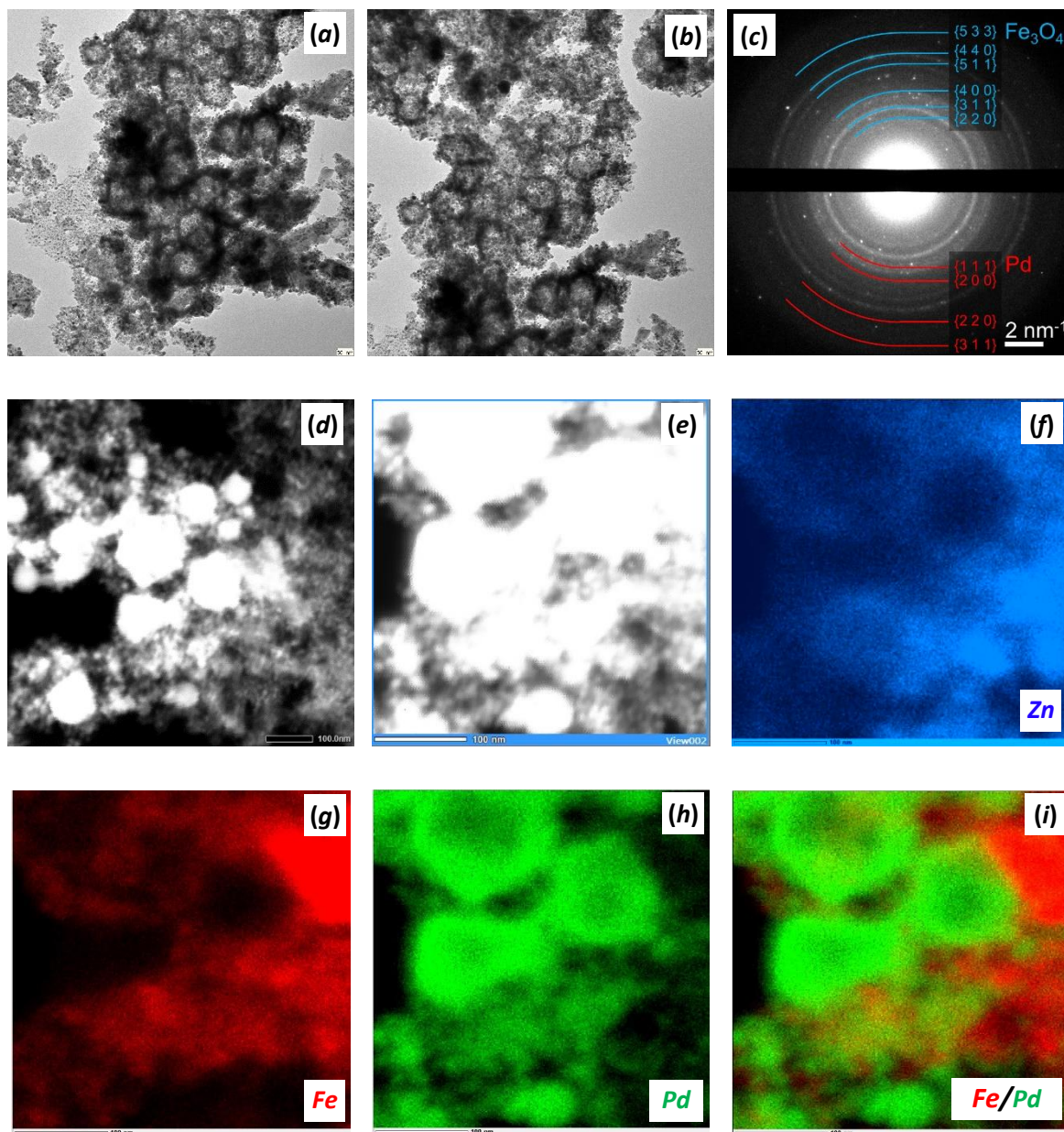


Fig. S79 (a-b) TEM images of $\text{Fe}_3\text{O}_4/\text{Pd-on-ZIF8-NP}$ [Fe: 5 ± 2 or 3 nm; Pd: - (no reliable sizes could be derived); ZIF-8: 104 ± 17 nm]; (c) SAED (d-e) STEM image $\text{Fe}_3\text{O}_4/\text{Pd-on-ZIF8-NP}$ followed by (f-i) TEM-EDX element mappings for Zn, Fe, Pd and Fe/Pd combination (100 nm scale bar).

Fe_3O_4 -on-ZIF90NH₂-NP (1-stage toward Fe_3O_4 /Pd-on-ZIF90NH₂-NP)

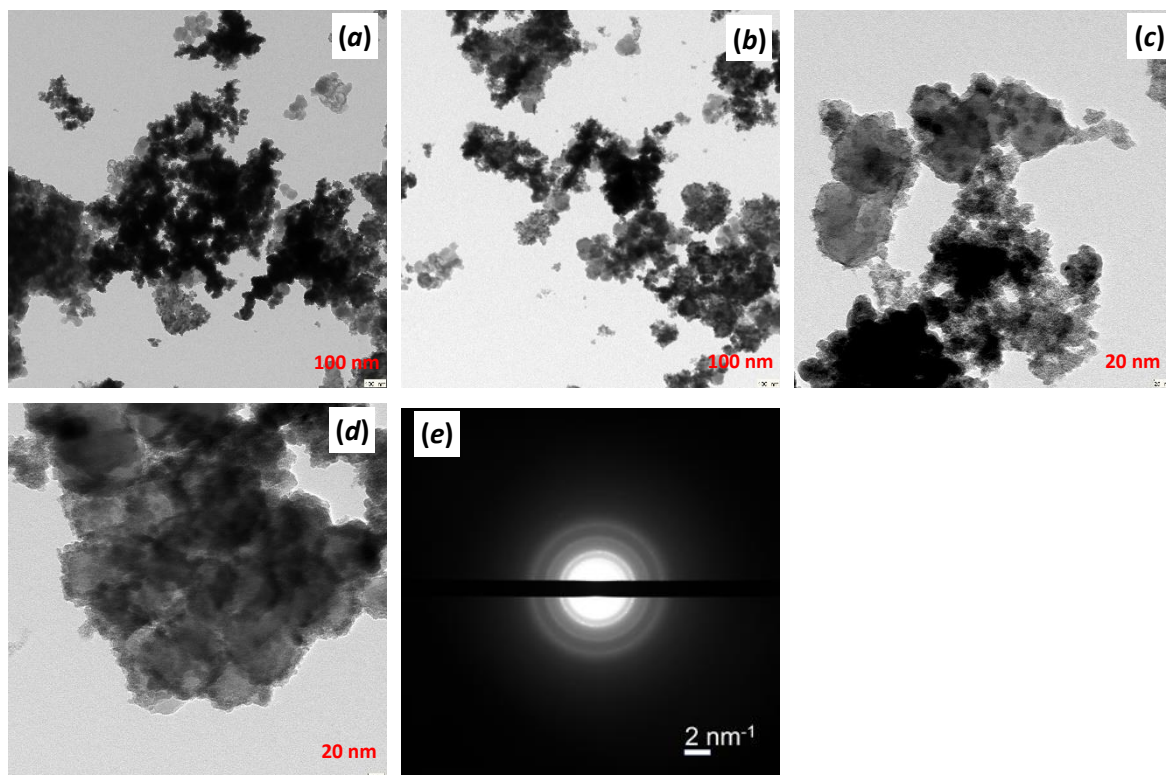


Fig. S80 (a-d) TEM images of Fe_3O_4 -on-ZIF90NH₂-NP [Fe_3O_4 : 13 ± 4 nm; ZIF-90NH₂-NP: 83 ± 16 nm]; (e) SAED.

$\text{Fe}_3\text{O}_4/\text{Pd-on-ZIF90NH}_2\text{-NP}$ (2-stage toward $\text{Fe}_3\text{O}_4/\text{Pd-on-ZIF90NH}_2\text{-NP}$)

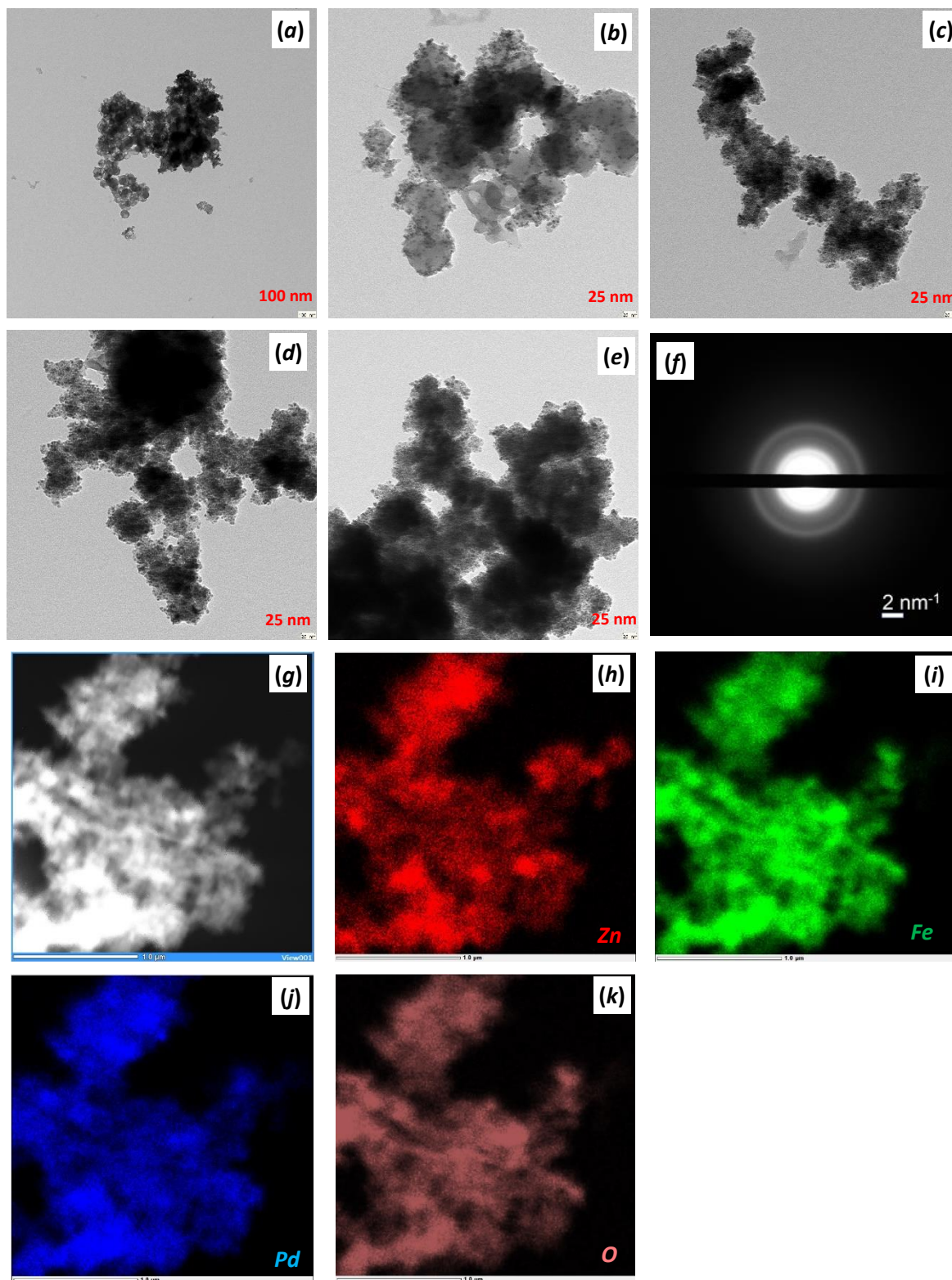


Fig. S81 (a-e) TEM images of $\text{Fe}_3\text{O}_4/\text{Pd-on-ZIF90NH}_2\text{-NP}$ [Fe_3O_4 : 13 ± 4 nm; Pd: - nm; ZIF-90NH₂-NP: 71 ± 13 nm]; (f) SAED; (g) STEM image $\text{Fe}_3\text{O}_4/\text{Pd-on-ZIF90NH}_2\text{-NP}$ with black and white corresponding to the minimum and maximum concentrations, followed by (h-k) TEM-EDX element mappings for Zn, Fe, Pd and O (1.0 μm scalebar): (h-k) the color saturation based mapping, where the concentration is represented by the color's saturation, with black and colored corresponding to the minimum and maximum concentrations.

AAS, SEM-EDX and STEM-EDX results of Fe₃O₄/Pd-on-ZIF8-NP and Fe₃O₄/Pd-on-ZIF90NH₂-NP:

Sample	AAS Fe ₃ O ₄ -content [% _{atom}]	AAS Pd-content [% _{atom}]	SEM-EDX Fe ₃ O ₄ -content [% _{atom}]	SEM-EDX Pd-content [% _{atom}]
Fe ₃ O ₄ /Pd-on-ZIF8-NP	5.05	5.20	49.36	13.64
Fe ₃ O ₄ /Pd-on-ZIF90NH ₂ -NP	20.36	16.71	45.45	4.38

STEM-EDX results on Pd/Fe₃O₄-on-ZIF8-NP (given as an example to show the high variation):

Point-Nr.	Pd-content [% _{atom}]	Fe ₃ O ₄ -content [% _{atom}]	Zn-content [% _{atom}]
1	1.27	5.27	40.69
2	15.36	15.05	30.17
3	2.93	6.32	41.12
4	6.90	10.33	36.81
5	6.37	4.35	44.13
6	5.91	9.34	40.91
7	6.33	13.01	40.49

STEM-EDX results on Fe₃O₄/Pd-on-ZIF8-NP (given as an example to show the high variation):

Point-Nr.	Pd-content [% _{atom}]	Fe ₃ O ₄ -content [% _{atom}]	Zn-content [% _{atom}]
1	6.43	17.33	3.40
2	26.98	1.58	0.80
3	16.57	6.52	3.94

PXRD

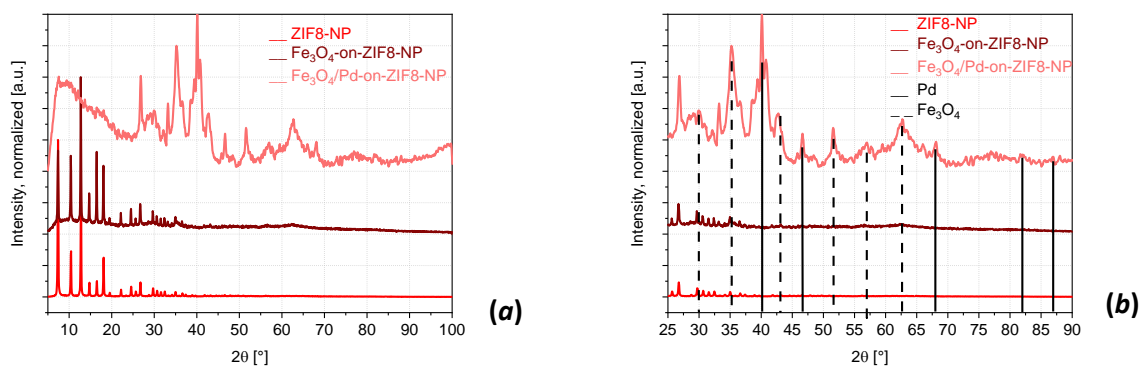


Fig. S82 Comparison of the PXRD patterns for the Fe_3O_4 -/Pd-on-ZIF8-NP and Pd-on-ZIF8-NP with the ZIF8-NP support material and the simulated PXRDs for Pd-metal and Fe_3O_4 crystalline phases: (a) full pattern, (b) expansion. Note the evident crystallinity of the Pd- and near-complete amorphicity of the Fe_3O_4 constituents (the peaks corresponding to the latter are practically absent).

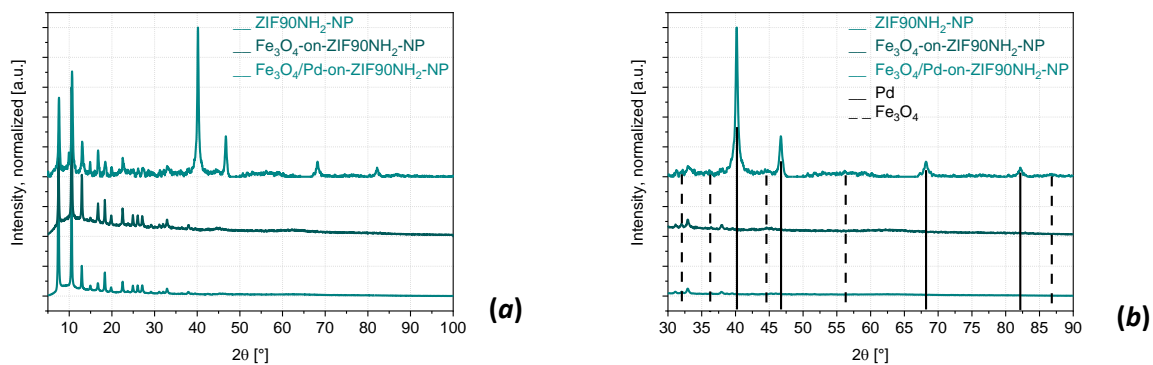
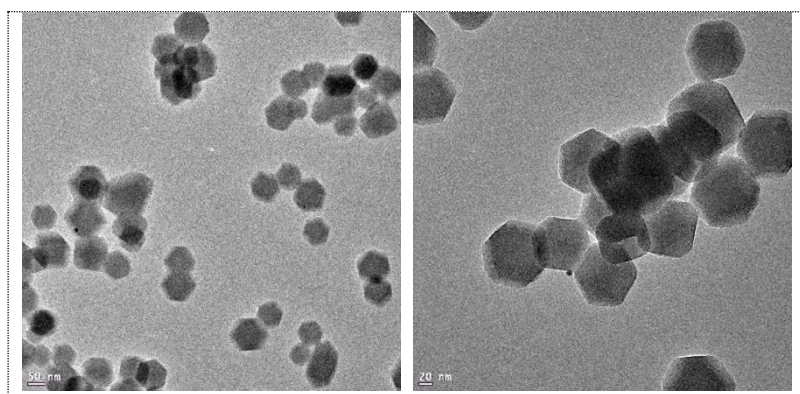
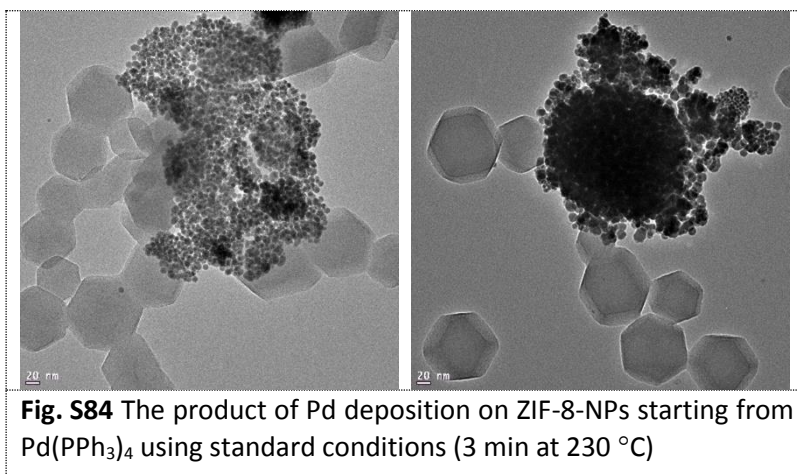


Fig. S83 Comparison of the PXRD patterns for the Fe_3O_4 -/Pd-on-ZIF90NH₂-NP and Fe_3O_4 -on-ZIF90NH₂-NP with the ZIF90NH₂-NP support material and the simulated PXRDs for Pd-metal and Fe_3O_4 crystalline phases: (a) full pattern, (b) expansion. Note the evident crystallinity of the Pd- and near-complete amorphicity of the Fe_3O_4 constituents (the peaks corresponding to the latter are practically absent).

6.5 $\text{Pd}(\text{PPh}_3)_4$ as a precursor in the attempted synthesis of Pd-on-ZIF-8





When Pd(PPh₃)₄ is used as a precursor instead of PdCl₂ with ZIF-8-NP as a support (3 min at 230 °C in [BMIm][NTf₂]); the molar concentration of Pd was kept the same, see Table S5 for Pd-ZIF-8-NP), the formed nanoparticles (~1-5 nm) are not distributed uniformly, but mostly agglomerated, even if showing good adhesion to ZIF-8 particles (Fig. S84). Non-agglomerated deposited Pd particles are also observable, but rare.

It is possible that the presence of PPh₃ provided in this case additional sterical stabilization during the growth of the NPs and prevented an efficient uniform deposition. The use of PdCl₂ was found to be the most consistent regarding composite quality. The chlorido-ligand, present only in small concentration, might play a minor role in 'etching' the surface of the ZIF-NPs at high temperatures as it is more nucleophilic compared to NTf₂⁻.

6.6 Rh deposition on ZIF-8-NP and ZIF-90-NH₂

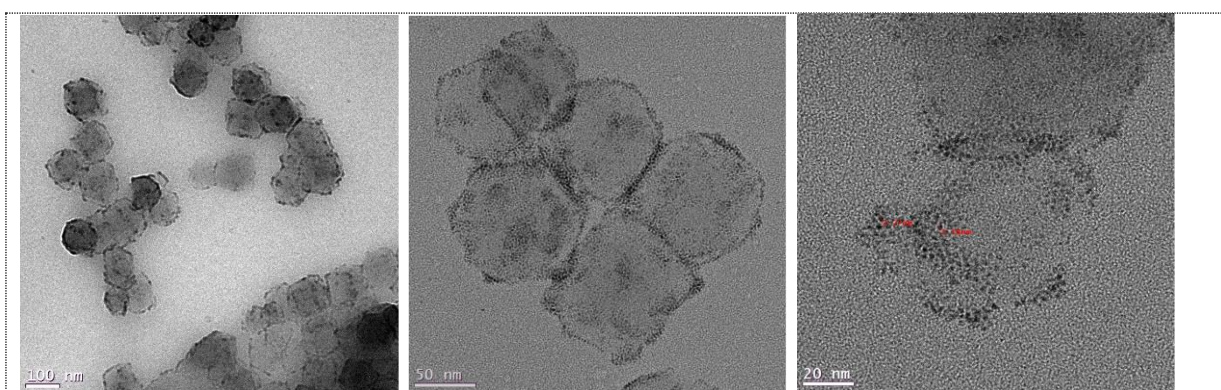


Fig. S85. The product of Rh-NP deposition (1-3 nm) on ZIF-8-NPs (50-100 nm) starting from Rh₆(CO)₁₆ as a precursor (3 min 230 °C; standard conditions).

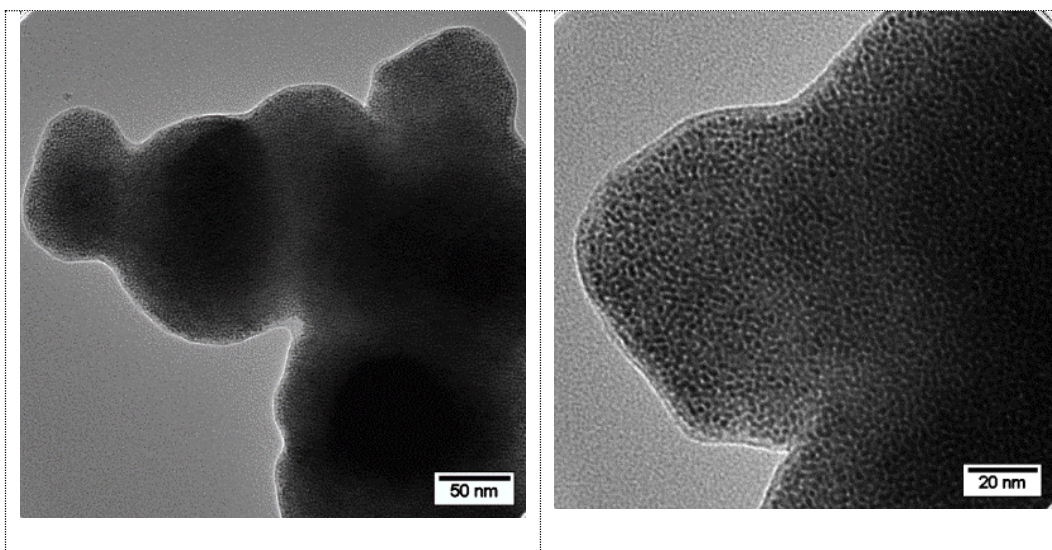


Fig. S86. The product of Rh-NP deposition (1-3 nm) on microcrystals of ZIF-90-NH₂ starting from Rh₆(CO)₁₆ as a precursor (3 min 230 °C; standard conditions).

The standard synthesis conditions (incl. the same molar concentrations), used for deposition of Pd were suitable for some other noble metals, but particularly well for rhodium, when Rh₆(CO)₁₆ was used as a precursor. The Rh-NPs with a size of 1-3 nm were very well formed, though some non-attached 'loose' particles were also observed.

7 Pd-on-MOF nanocomposites as catalysts

Syringe filters with cellulose acetate filtration layer having a porosity of 0.2 μ m (supplied by VWR) were used for the filtration of the reaction medium aiming the separation of the major part of the heterogeneous catalyst (see the discussion regarding the filter pore-size in the context of the experiment in the Methodology section below, p. 91). The spectra in the range of 200-600 nm were collected; polystyrene cuvettes 10 x 4 x 45 mm, with light beam path length of $l = 10$ mm, were used.

7.1 Reduction of 4-nitrophenol to 4-aminophenol

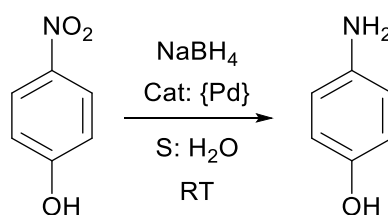


Fig. S87 The reduction of 4-nitrophenol to 4-aminophenol in an aqueous solution of sodium borohydride.

Motivation

The reduction of 4-nitrophenol to 4-aminophenol was selected as an interesting model reaction allowing efficient UV-VIS spectroscopic monitoring. While the possibility of a convenient kinetic study was primary, the catalysis of the nitro-group reduction, as well as the particular reagent/reactant pair, poses a general interest.

4-aminophenol is an industrially viable intermediate in the production of pharmaceuticals, primarily of the analgesic/antipyretic paracetamol (previously also the considerably toxic phenacetin of the same drug group), as well in the production of dyes (primarily diazo-dyes, like the “fast yellow” histological dye, while 4-aminophenol it is itself a wood stain, imparting to a wood a rose-like coloration) [8] and corrosion inhibitor formulations (see also [9]).

4-Nitrophenol is the simplest synthetic precursor to 4-aminophenol. The former has significant toxicity and is recognized as a “priority pollutant” by U.S. EPA, [10] calling for developments of removal/deactivation methods (see [11] and references therein). Hence, the maximally complete reduction of 4-nitrophenol and analogous nitroarenes is significant in the industrial context.

The catalytic reduction of nitro- to amino-group by NaBH₄ is a classical topic and a variety of catalysts, including Pd, Ru, Fe compounds, are known (see [12] and references therein). The reaction

is very slow without a catalyst, while not enough catalyst efficiency combined with special conditions might lead to products of partial reduction (the latter by-product might include the azoxy-, azo- and hydrazo- compounds similar to the intermediaries of the classical Zinin's reduction of nitroarenes by ammonium sulfide or Zn/HCl in aqueous medium). Pd, particularly often used for this reaction in a form of Pd/C with H₂ as a reductant, is one of the best catalysts known, while NaBH₄ is a milder, but more conveniently handled reagent compared to H₂. Overall, the reduction of nitroarenes with NaBH₄ represents a good model reaction for Pd-on-MOF due to convenient rates (typical time scale from minutes to hours) and easy spectrophotometric detection.

Methodology

The used method is inspired by the recent publication on the catalytic reduction of nitrophenols by NaBH₄ using Pd@MIL-100(Fe) as a catalyst [13].

4-Nitrophenol was dissolved in 26.6 ml of precisely "Millipore water" in a 100 ml flask with a tight stopper. The addition of a weighted amount of a large excess of NaBH₄, app. 260 mg (Table S7) was followed (all operations were performed in air); the latter was dissolved within ~2 minutes (the reaction progress without the added catalyst was negligible for tens of minutes, as by a blank reaction). A UV-Vis measurement was taken from the 'initial' state ($\tau = 0$). The addition of a specified amount of the catalyst followed and the content of the round flask was continuously stirred (small elongated magnets, with relatively low magnetization, were used at medium-to-high rotation speeds, which ensured minor capture of the magnetic NPs and rapid exchange of medium in the vicinity of the magnet. From the purist's point of view, shaking might have been a better approach for the magnetic nanoparticles, but magnetic stirring was chosen for uniformity of the procedure and in favor of accurate sampling under continuous mixing). ~0.5 ml of the reaction mixture was taken by a syringe equipped by a syringe filter (0.2 μm), which ensured the removal of the majority of the catalyst in certain intervals depending on the evident reaction rate perceptible from the change of color. For the UV-Vis measurements, 25 μl of the filtered sample was transferred to a UV-Vis cuvette *via* a precision syringe, prefilled with 2 ml of "Millipore water". After a thorough mixing, the measurement was taken. (Fig. S88)

Notes:

- The addition of NaBH₄ was performed immediately after 4-nitrophenol and the dissolution was performed in less than 2 minutes. Blank tests confirmed that the reaction progress without the added catalyst was negligible within experimental error for tens of minutes).

- The catalyst was added at once, simultaneously with the start of the timer. Too rapid stirring (> 1000 rpm) was avoided to preclude possible mechanical stress and release of the Pd-NPs from the surface of the composite).
- The filtration of the sample for the spectrophotometric determination did not remove all the catalytic particles, but the majority of them (it is known from our experience that for example, the ZIF-8 nanoparticles in methanol are existing in a form of both separate particles and aggregates, detectable using DLS as peaks corresponding to ~50-100 nm and ~1-2 nm particles).
- The UV-Vis measurements were performed as soon as possible (within 1-2 h) after the sample was collected. Repeated measurements of selected samples showed that the concentration did not change significantly after a few hours, which proved that the approach is viable (however, the storage for one day or more had a significant influence).



Fig. S88 An example sequence ($n \times 1$ min) of spectrophotometric cuvettes with the diluted reaction medium. The yellow coloration, gradually disappearing in the course of the reaction, is conditioned by 4-nitrophenol.

Assessment of the spectroscopic data. The NaBH_4 reductant was taken in ~50 molar excess compared to 4-nitrophenol, which allows postulating a pseudo 1-st order kinetics, i.e. $\ln[c_0 / c(\tau)] = k\tau$ is assumed, where c_0 and $c(\tau)$ is the initial and current (corresponding to time τ) concentration of 4-nitrophenol. $c(\tau)$ was calculated as $c(\tau) = c_0(I(\tau)/I_0)$, where I_0 and $I(\tau)$ are the signal intensities at ν_{\max} at the beginning of the experiment and after time τ (the maximum of absorbance, ν_{\max} , for 4-nitrophenol in water is 317 nm, while for the 4-aminophenol is 298 nm). The reaction rate constant, k , was obtained as a linear regression of the $\ln(c_0/c(\tau))$ vs τ dependence.

TOF_τ , is the nominal turnover frequency (rate), $\text{TOF} [\text{s}^{-1}]$, at time τ . For the reaction, where the amount of reacted substrate is equal to the amount of the product, the TOF, i.e. the number of reacted molecules to the number of catalyst molecules for a unit of time is, by definition:

$$\text{TOF}_\tau = \lim_{\Delta t \rightarrow 0} \left(\frac{[c(\tau + \Delta t) - c(\tau)] / \Delta t * V}{\{(m_{\text{cat}} * X_{\text{Pd}}) / (M_{\text{Pd}})\}} \right) = \left. \left\{ -\left(\frac{dc}{dt}\right)_{t=\tau} * V \right\} / \{(m_{\text{cat}} * X_{\text{Pd}}) / (M_{\text{Pd}})\} \right. \quad (\text{Eq. 7.1})$$

where c_0 , $c(\tau)$ the initial and actual molar concentrations of the substrate (4-nitrophenol); V is the volume of the solution; m_{cat} is the weight of the catalyst composite; x_{Pd} is the palladium weight share (0-1); M is the molecular weight of palladium.

For a pseudo-first order reaction, $c(\tau) = C_0 \cdot \exp(-k \cdot \tau)$, hence $(dc/dt)|_{t=\tau} = -kc_0 e(-k \cdot \tau)$

$$\text{TOF}_0 = k \cdot c_0 \cdot V \cdot M_{\text{Pd}} / m_{\text{cat}} \cdot x_{\text{Pd}} \quad (\text{Eq. 7.2})$$

While the fitting of the data with an exponential function was not always good, the linear approximation of the TOF_0 was also calculated as a linear approximation:

$$\text{TOF}_0, \text{ l.a.} \sim \{[(c_0 - c_{t_1})/t_1] \cdot V \cdot M_{\text{Pd}}\} / \{m_{\text{cat}} \cdot x_{\text{Pd}}\} \quad (\text{Eq. 7.3})$$

Where c_0 is the initial concentration and c_{t_1} is the concentration of the first measured sample after the start of the reaction at time t_1 .

The TOF approximations above follow a formal approach, which allows comparing the catalysts without analyzing the nature of the active sites. The catalytic activity of Pd is assumed to be approximately proportional to the surface area of the Pd-particles (approximately, because the specific influence of the surface part, blocked by the support is somewhat dependent on the particle size). Accordingly, a $\text{TOF}_{\tau, S}$ [$\text{s}^{-1} \text{m}^{-2}$] value was also computed for surface-specific comparison, with the surface area calculated as a

$$\text{TOF}_{\tau, S} \sim \text{TOF}_{\tau} / S_{1/2, \text{Pd}} \equiv \text{TOF} / (3 \cdot m_{\text{cat}} \cdot x_{\text{Pd}} / \rho \cdot d) \quad (\text{Eq. 7.4})$$

Where d is the diameter of the particles found from TEM and ρ is their density. The surface area in this case is formally approximated as consisting of isolated geometrical hemispheres – while the other hemisphere is blocked by the surface of the support -- with a total accessible surface area of $S_{1/2, \text{Pd}} = [(m_{\text{Pd}}/\rho_{\text{Pd}})/V_{\text{particle}}] \cdot (0.5 \cdot S_{\text{particle}}) = [(m_{\text{Pd}}/\rho)/(4\pi \cdot r^3/3)] \cdot 2\pi r^2 = (3/2) \cdot m_{\text{Pd}}/(\rho \cdot r) = 3 \cdot m_{\text{cat}} \cdot x_{\text{Pd}}/(\rho \cdot d)$.

Limitations of the experimental method. It is necessary to mention the inherent limitations of the used simple methodology, which intends an express testing rather than a precise physicochemical study. The important point is that most of the errors are systematic in nature and distort the perception of the catalyst's relative performance much less compared to absolute kinetics estimates (the later were of secondary importance in this preliminary report):

- During the filtration some of the nanoparticles could go through the filter, because the filter pore-size (~200 nm) is relatively large. In any case, we did not observe significant turbidity in the filtrated sample, and evidently, most of the black-colored nanoparticles were filtered off due to their moderate tendency to agglomerate, particularly in aqueous conditions. Moreover, the complete re-dispersion was avoided (contrary to

the possible application of strong stirring or ultrasonication). The incomplete redispersion and hence the lower surface area might have affected the results, giving a lower, or more “conservative” estimate of the catalytic activity.

The filtration procedure was chosen instead of centrifugation because the former is faster: a rapid decrease in the concentration of the nanoparticles in the sample was targeted instead of complete removal. The near freeze of the reaction progress is sufficient for assessment experiments with the expected significant experimental error level. In order to decrease the experimental error, the UV measurements on the samples were taken in parallel with their harvesting of the samples. The maximal delay was around 30 minutes, which is at the same order of magnitude as the time between the sampling.

The experimental error, associated with the nanoparticle leakage through the filter, is $< \sim 10\%$ at an arbitrary 95% retention and a typical 15 min period. While the latter estimate seems large, this error is systematic and affects all the experiments. Hence, the relative values are much more precise; the error, in this case, could be held equivalent with a systematic time measurement error for all the measurements.

The volume, 0.5 ml (26.6 ml of total initial volume), removed for each sample is substantial (such volume is dictated by the necessity of convenient filtration). The removal of a large volume could have enriched the reaction medium by the partially coagulated catalyst. The influence of this effect was neglected.

- The concentration determination through the intensity of the absorption peak at ν_{\max} , $c(\tau) = c_0 I(\tau)/I_0$, is satisfactory at relatively low concentration difference from C_0 , but decreases at significant differences (two and more times).
- The concentration of the product, 4-aminophenol, $C_p(\tau)$ is taken to be $c_0 - c(\tau)$, where c_0 and $c(\tau)$ are the initial concentration and the concentration at time τ of the substrate, 4-nitrophenol, respectively. It is a reasonably good approximation taking into account that the conversion is nearly complete. However, it is still an approximation, which is evident in the “smearing” of the isosbestic point on some of the UV-Vis temporal development graphs.

Results

The results are summarized in Tables S6,7. The temporal development of the UV-Vis spectra is shown on Fig. 100-116, while the HPLC-based raw data (also used for the calculation of $TOF_{0,l.a.}$ for cross-checking) is also listed in selected cases.

Table S6 Overview of the selected catalysts, their performance and kinetics in the reduction of 4-nitrophenol by NaBH₄ in water (minimum dataset).

Catalyst	4-Nitro-phenol weight, [mg]	Catalyst weight [mg]	c ₀ substrate [mmol L ⁻¹]	c(t1), relative conc. substrate, [mmol L ⁻¹]	t ₁ , [s]	k _{raw} , log(c/c ₀) - t regression, [min ⁻¹]	k, ln(c/c ₀) - t regression, [s ⁻¹]	x _{Pd} , AAS	<d> _{Pd} particles, [nm]	S _{1/2,Pd} , [m ²]	TOF ₀ , I.a. HPLC [s ⁻¹]	TOF ₀ , UV-Vis [s ⁻¹]	TOF _{0,5} [s ⁻¹ m ⁻²]
Pd-on-ZIF8-NP	18.6	3.0	5.027	0.103	60	-0.0270	0.00104	0.15	6	0.0189	0.473	0.033	1.73
Pd-on-ZIF90NH ₂ _1	18.6	3.0	5.027	0.867	60	-0.0959	0.00368	0.0457	11	0.0031	0.230	0.38	122
Pd-on-ZIF90NH ₂ -NP_1	18.6	3.1	5.027	0.594	60	-0.1989	0.00763	0.1236	12	0.0080	0.251	0.28	35.2
Pd-on-ZIF90NH ₂ _2	18.5	3.1	5.000	0.867	60	-0.0829	0.00318	0.0457	11	0.0032	0.221	0.32	97.9
Pd-on-ZIF90NH ₂ -NP_2	18.7	3.2	5.054	0.273	60	-0.2167	0.00832	0.1236	12	0.0083	0.438	0.30	36.2
Pd-on-MAF66	18.5	3.0	5.000	0.0738	60	-0.5182	0.01989	0.0875	8	0.0083	0.832	1.07	130
Fe ₃ O ₄ -on-ZIF8-NP	18.7	2.9	5.054					-	-	-	-	low	-
Fe ₃ O ₄ -on-ZIF90NH ₂	18	2.3	4.864					-	-	-	-	low	-
Fe ₃ O ₄ -on-ZIF90NH ₂ -NP	18.5	3.1	5.000					-	-	-	-	low	-
Pd/Fe ₃ O ₄ -on-ZIF8-NP	18.5	3.5	5.000	0.644	600	-0.0134	0.00051	0.1465	11	0.0118	0.016	0.014	1.21
Pd/Fe ₃ O ₄ -on-ZIF90NH ₂	18.5	3.0	5.000	0.054	15	-1.9480	0.07476	0.0947	6	0.0119	3.142	3.72	312
Pd/Fe ₃ O ₄ -on-ZIF90NH ₂ -NP	18.5	3.0	5.000	0.264	30	-0.3470	0.01332	0.0508	10	0.0038	2.278	1.24	322
Pd/Fe ₃ O ₄ -on-MAF66	18.4	4.0	4.973	0.0603	20	-2.6690	0.10243	0.0879	8	0.0111	1.881	4.10	370
Fe ₃ O ₄ /Pd-on-ZIF8-NP	18.5	3.0	5.000	0.819	60	-0.2632	0.01010	0.052	?	-	0.274	0.92	?
Fe ₃ O ₄ /Pd-on-ZIF90NH ₂ -NP	18.7	3.0	5.054	0.094	20	-2.4920	0.09564	0.1671	?	-	1.293	2.73	?
Pd/C, 10%	18.5	3.0	5.000			-0.0485	0.00186	0.1		?	-	0.088	-
Blank	18.5	-	5.000				0.00000	-		?	-	low	-
ZIF-8-NP	18.7	3.3	5.054				0.00000	-		-	-	low	-
ZIF-90NH ₂	18.7	3.4	5.054				0.00000	-		-	-	low	-
ZIF-90NH ₂ -NP	18.5	3.3	5.000				0.00000	-		-	-	low	-
MAF-66	18.5	3.3	5.000				0.00000	-		-	-	low	-

Color codes:

- input data headers for the calculation of the kinetics, - output data headers of the TOF values, - poor fit of the k-value.

Explanations on the headers:

4-nitrophenol weight is the precise weight of the substrate dissolved in 26.6 ml of distilled water.

c₀ is the calculated initial concentration of the substrate; **c_{t1}** and **t1** are the concentration for the first measured point (both HPLC-based, unlike the other UV-Vis data), used for cross-checking and calculation of the linear-approximation **TOF_{0, l.a.}**.

k-raw is the fitting of the $\log(c/c_0)$ -t[min] dependence.

k is the reaction rate for the assumed pseudo first-order reaction, corresponding to $\ln(C/C_0)$ -t[s], and converted from **k-raw**; **x_{Pd}** is the weight content of Pd in the catalyst; $\langle d \rangle_{Pd}$ size of the Pd nanoparticles in the composites as determined by TEM based statistics.

S_{1/2, Pd} is the half-surface area of the Pd-nanoparticles calculated from the known content and their size, while assuming a spherical shape.

TOF_{0, l.a.} is the **TOF₀** estimation using the $c(0)$ and $c(1)$ values corresponding to the initial concentration of the substrate and the first measured point. The **TOF_{0, l.a.}** is HPLC-based, unlike the other UV-Vis spectroscopy-based kinetic data, and serves the purpose of comparison with **TOF₀** (see below). If the discrepancy is large, there is a poor fit of the data by pseudo-first-order kinetics (marked by color), of a discrepancy between the UV-Vis and HPLC data. In this work, the latter discrepancy is not large in nearly all cases and the major source of the disagreement is the poor fit. For a poor fit of the **k** the **TOF_{0, l.a.}** gives somewhat more meaningful approximation, but otherwise, **TOF₀** is preferred.

TOF₀ is the turnover frequency calculated from the fitted **k**-value

TOF_{0,s} equals $TOF_0 / S_{1/2, Pd}$, i.e. it is the surface area-specific TOF related to the half-surface (\sim accessible surface) of the Pd-nanoparticles.

Table S7 Overview of the kinetics of the reduction of 4-nitrophenol by NaBH₄ by selected catalysts together with parameters of indirect influence, primarily Fe-content and surface areas).

Catalyst	4-Nitrophenol weight, [mg]	Catalyst weight [mg]	NaBH ₄ weight, [mg]	k, ln(c/c ₀) - t regression, [s ⁻¹]	x _{Pd} , AAS	<d> Pd particles, [nm]	x _{Fe} , AAS [nm]	<d>Fe ₃ O ₄ particles, [nm]	<d>, MOF-particles, [nm]	S _{surf} , exp. [m ² g ⁻¹]	S _{1/2,Pd} rel. [m ² g ⁻¹]	S _{1/2,Pd} abs. [m ²]	TOF ₀ , UV-Vis [s ⁻¹]	TOF _{0.5} [s ⁻¹ m ⁻²]
Pd-on-ZIF8-NP	18.6	3.0	266.8	0.00104	0.15	6	-	-	85	1646	42.0	0.0189	0.033	1.73
Pd-on-ZIF90NH ₂ _1	18.6	3.0	265.8	0.00368	0.0457	11	-	-	1200	362	22.9	0.0031	0.38	122
Pd-on-ZIF90NH ₂ -NP_1	18.6	3.1	266.8	0.00763	0.1236	12	-	-	88		21.0	0.0080	0.28	35.2
Pd-on-ZIF90NH ₂ _2	18.5	3.1	265.2	0.00318	0.0457	11	-	-	1200	362	22.9	0.0032	0.32	97.9
Pd-on-ZIF90NH ₂ -NP_2	18.7	3.2	265.2	0.00832	0.1236	12	-	-	88		21.0	0.0083	0.30	36.2
Pd-on-MAF66	18.5	3.0	265.8	0.01989	0.0875	8	-	-	426	362	31.5	0.0083	1.07	130
Fe ₃ O ₄ -on-ZIF8-NP	18.7	2.9	265.7	-	-	-	0.1186	5	83	568	-	-	low	-
Fe ₃ O ₄ -on-ZIF90NH ₂	18	2.3	256.5	-	-	-	0.2154	13	2500		-	-	low	-
Fe ₃ O ₄ -on-ZIF90NH ₂ -NP	18.5	3.1	266.2	-	-	-	0.1669	11	81		-	-	low	-
Pd/Fe ₃ O ₄ -on-ZIF8-NP	18.5	3.5	265.8	0.00051	0.1465	11	0.0939	?	117		22.9	0.0118	0.014	1.21
Pd/Fe ₃ O ₄ -on-ZIF90NH ₂	18.5	3.0	265.6	0.07476	0.0947	6	0.1058	?	2400		42.0	0.0119	3.72	312
Pd/Fe ₃ O ₄ -on-ZIF90NH ₂ -NP	18.5	3.0	265.4	0.01332	0.0508	10	0.1868	?	70		25.2	0.0038	1.24	322
Pd/Fe ₃ O ₄ -on-MAF66	18.4	4.0	266.7	0.10243	0.0879	8	0.1113	?	420		31.5	0.0111	4.10	370
Fe ₃ O ₄ /Pd-on-ZIF8-NP	18.5	3.0	265.2	0.01010	0.052	?	0.0505	4.7			-	-	0.92	?
Fe ₃ O ₄ /Pd-on-ZIF90NH ₂ -NP	18.7	3.0	265.5	0.09564	0.1671	?	0.2036	?	-		-	-	2.73	?
Pd/C, 10%	18.5	3.0	257.4	0.00186	0.1		-	-		900 (as given)	?	?	0.088	-
Blank	18.5	-	265.5	-	-	-	-	-			?	?	low	-
ZIF-8-NP	18.7	3.3	265.9	-	-	-	-	-	114	1641	-	-	low	-
ZIF-90NH ₂	18.7	3.4	265.6	-	-	-	-	-		344	-	-	low	-
ZIF-90NH ₂ -NP	18.5	3.3	266.8	-	-	-	-	-	107		-	-	low	-
MAF-66	18.5	3.3	266.5	-	-	-	-	-	800		-	-	low	-

Color codes:

■ - data headers that represent fundamental information about the materials, which are not directly influencing the kinetics within the used model ■ - output data headers of the TOF values.

Explanations on the headers (only for cases, which are not given for the previous table):

NaBH₄ weight is the used amount of sodium borohydride. As a large excess was used it is considered to be a value that does not affect the kinetics.

x_{Fe}, AAS is the weight-based iron content (0-1) according to the AAS.

<d> Fe₃O₄ particles is the average TEM-based size of the Fe₃O₄ (in some cases it was not possible to determine reliably due to low contrast).

<d> MOF particles are the sizes of the MOF particles (individual or within the composite), which is roughly similar to the particle size of the composite.

S_{surf exp.} is the experimental BET surface area based on N₂ adsorption data for all cases except the Pd/C commercial catalyst, where the surface area from the specification is given.

S_{1/2,Pd} is the half-surface area of spherical Pd-nanoparticles per gram for the given TEM-based particle size.

Calibration curves (proof of linear response regarding the concentration of the analyte via UV-Vis spectroscopy and instrumental HPLC)

4-Nitrophenol

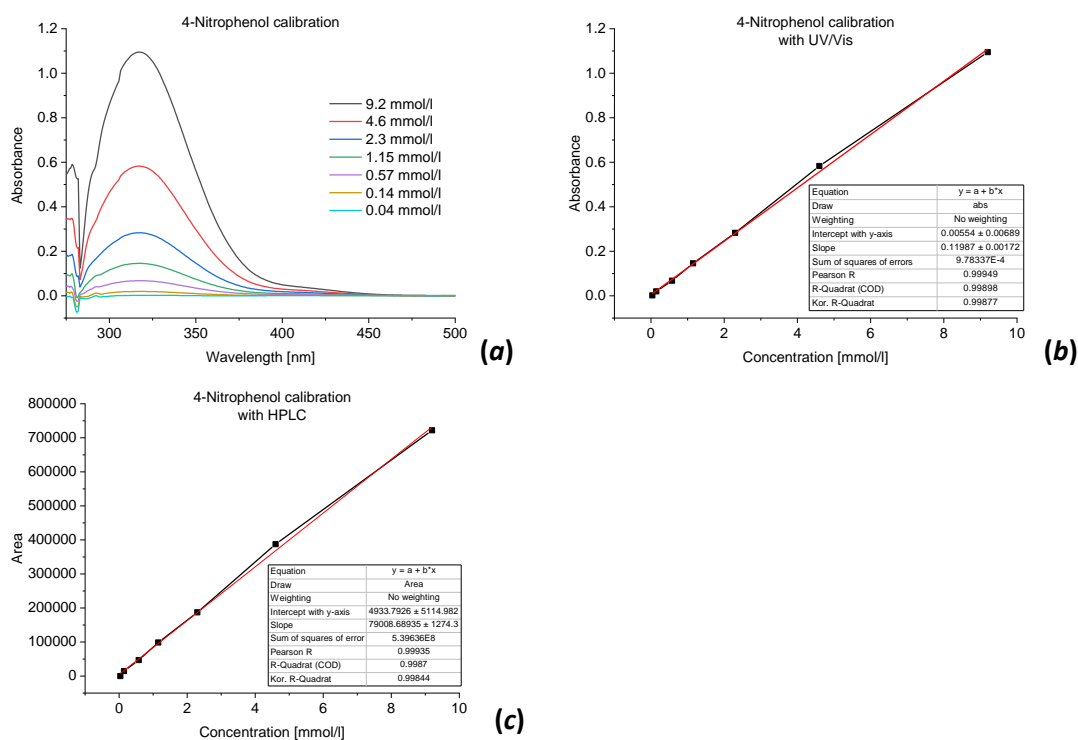


Fig. S89 (a) UV-Vis spectra for the calibration of 4-nitrophenol in water; (b) The concentration change of 4-nitrophenol. (c) HPLC measurement for a calibration experiment with 4-nitrophenol in water.

4-Aminophenol

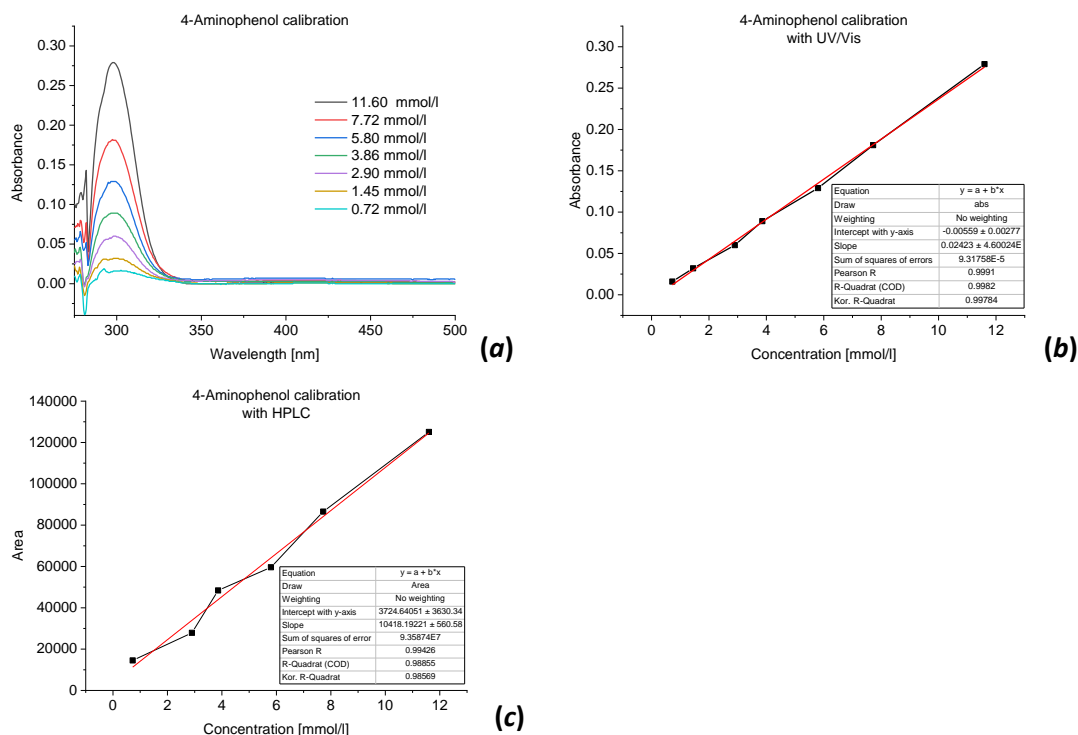


Fig. S90 (a) UV-Vis spectra for the calibration of 4-aminophenol in water; (b) The concentration change of 4-aminophenol. (c) HPLC measurement for a calibration experiment with 4-aminophenol in water.

Note: UV-Vis spectroscopic determination of 4-aminophenol was not performed in practice, because the extinction coefficient is much lower, compared to 4-nitrophenol and the relative closeness of the peaks might have influenced the precision of the determination.

Blank experiments with compounds containing no palladium

NP+NaBH₄

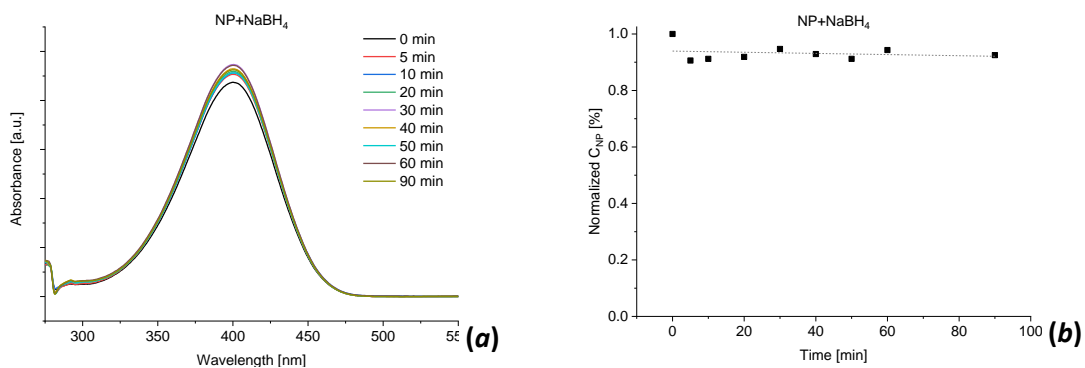


Fig. S91 Temporal development of UV-Vis spectra for a blank experiment, with an aqueous solution of 4-nitrophenol and sodium borohydride.

ZIF8-NP

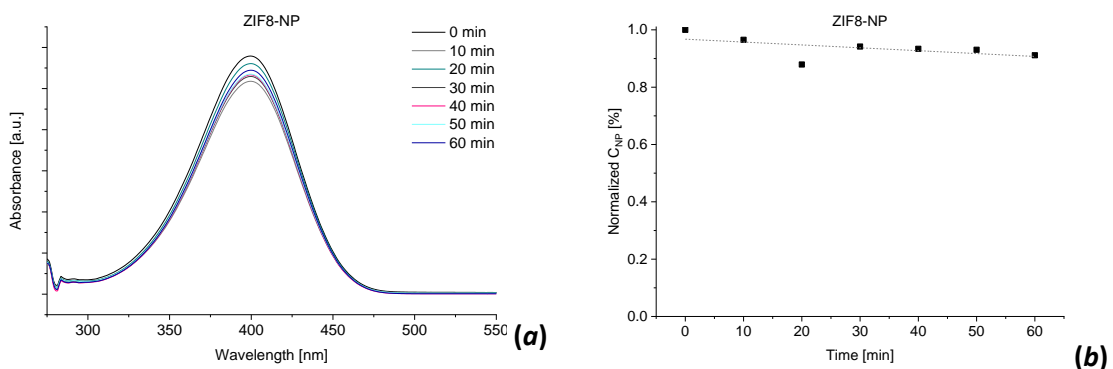


Fig. S92 (a) Temporal development of UV-Vis spectra for a blank experiment with the added ZIF-8-NP support and sodium borohydride; (b) The concentration change of 4-nitrophenol with time.

ZIF90NH₂

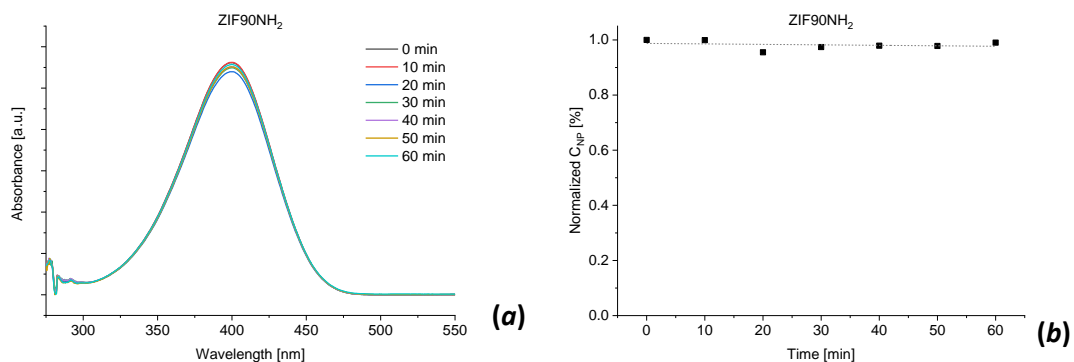


Fig. S93 (a) Temporal development of UV-Vis spectra for a blank experiment with the added ZIF90NH₂ catalyst and sodium borohydride; (b) the concentration change of 4-nitrophenol with time.

ZIF90NH₂-NP

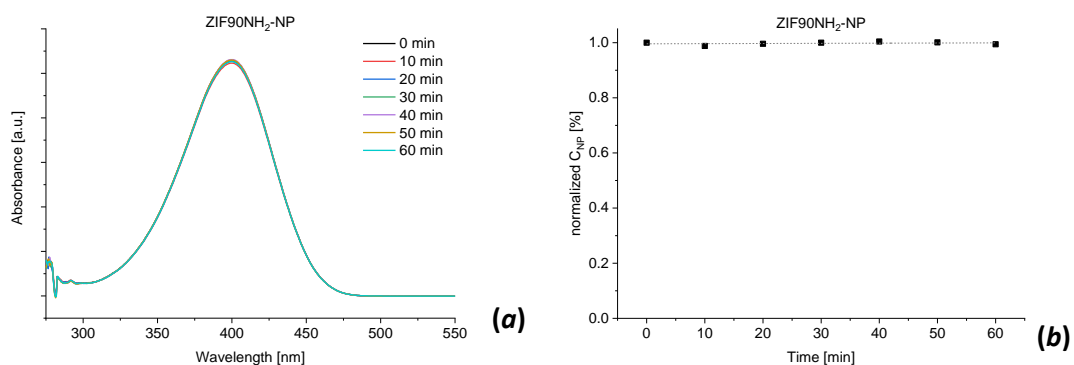


Fig. S94 (a) Temporal development of UV-Vis spectra for a blank experiment with the added ZIF90NH₂-NP catalyst and sodium borohydride; (b) the concentration change of 4-nitrophenol with time.

MAF-66

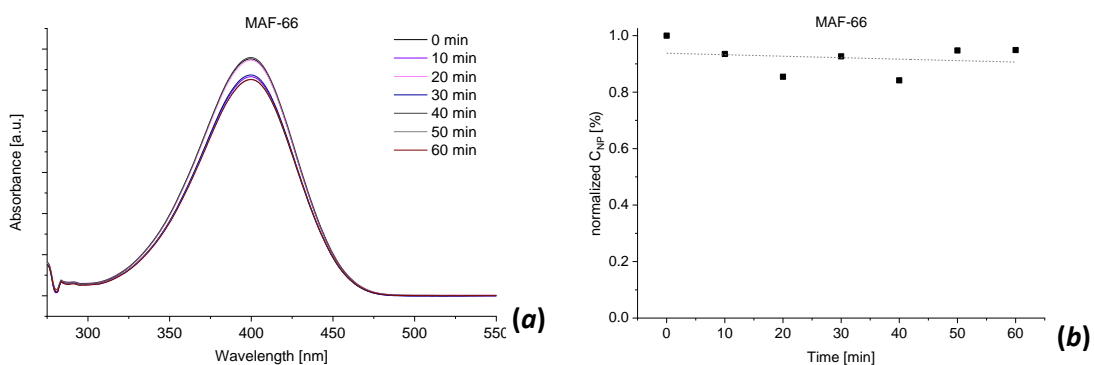


Fig. S95 (a) Temporal development of UV-Vis spectra for a blank experiment with the added MAF-66 catalyst and sodium borohydride; (b) the concentration change of 4-nitrophenol with time.

Fe₃O₄-on-MOF “supports”

Fe₃O₄-on-ZIF8-NP

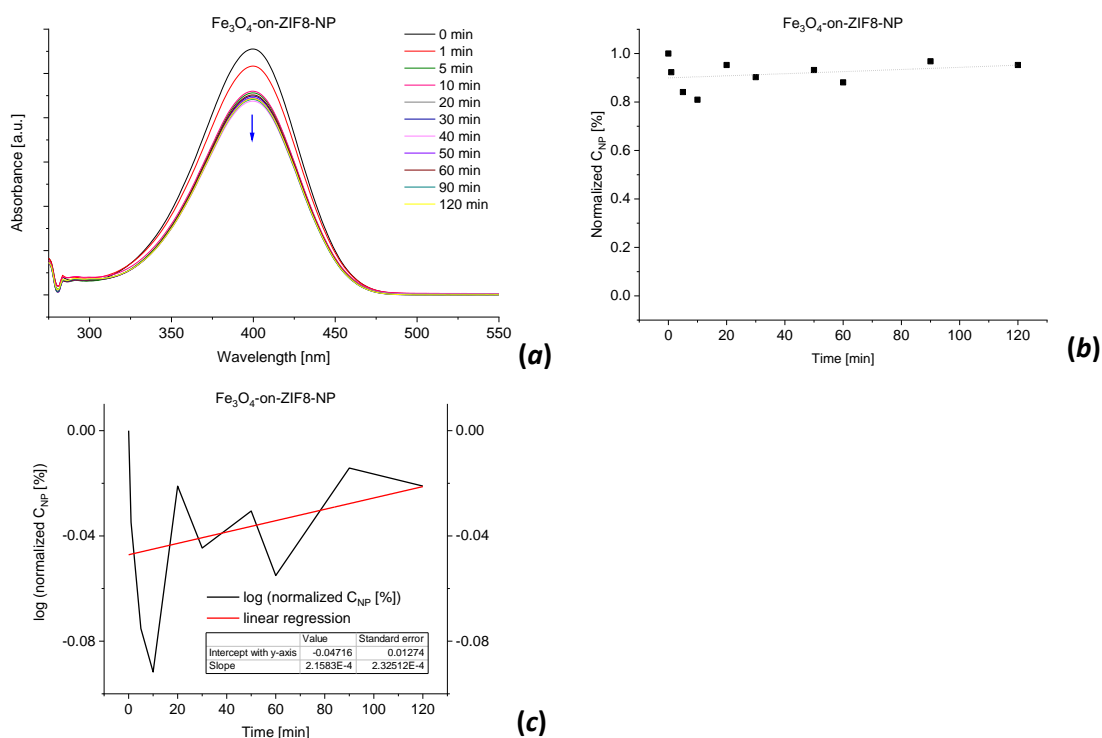


Fig. S96 (a) Temporal development of UV-Vis spectra for a blank experiment with the added Fe₃O₄-on-MOF composite; (b) the concentration change of 4-nitrophenol with time.

Fe₃O₄-on-ZIF90NH₂

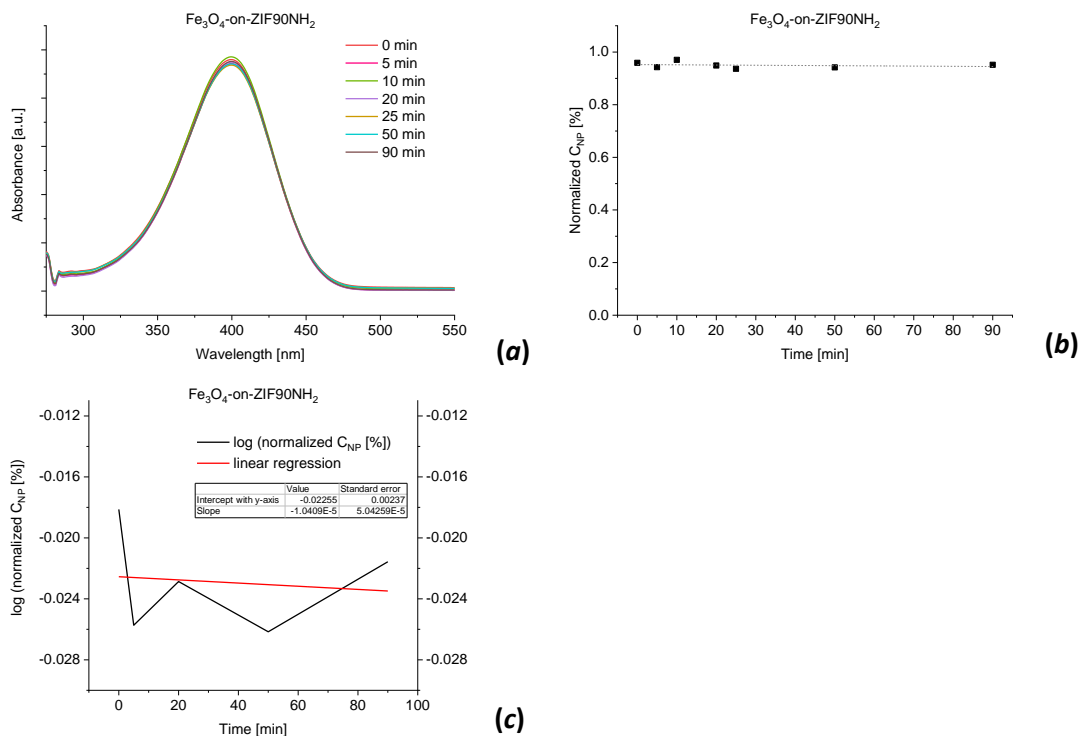


Fig. S97 (a) Temporal development of UV-Vis spectra for a blank experiment with the added Fe₃O₄-on-MOF composite; (b) the concentration change of 4-nitrophenol with time.

Fe₃O₄-on-ZIF90NH₂-NP

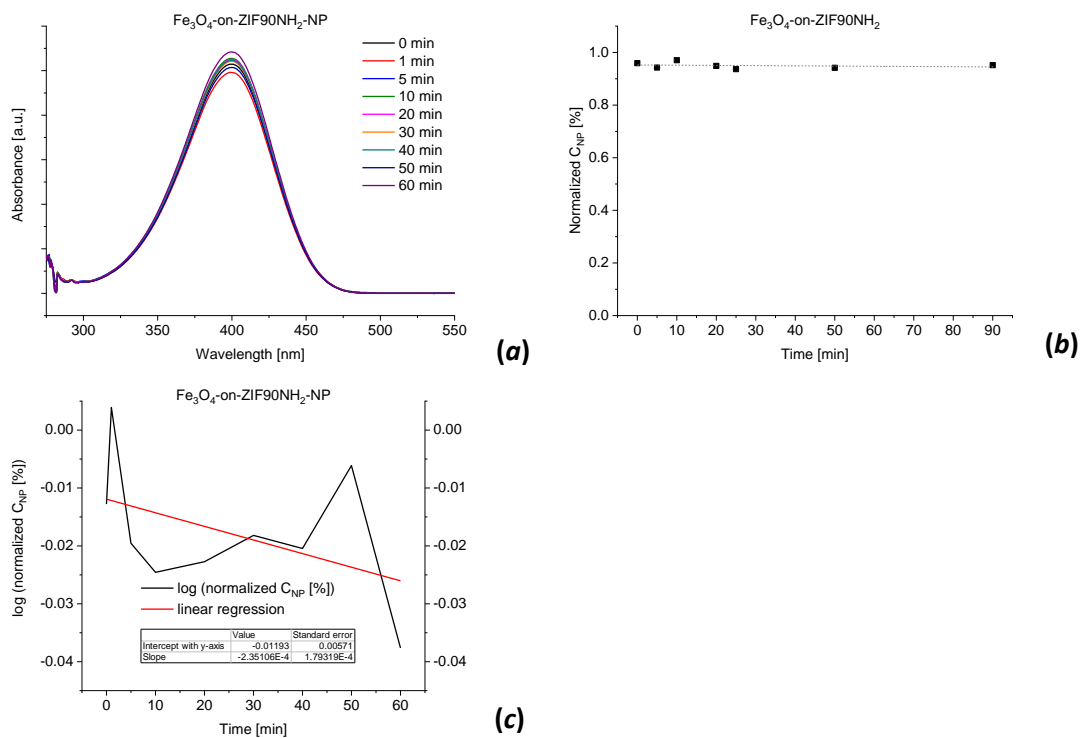


Fig. S98 (a) Temporal development of UV-Vis spectra for a blank experiment with the added Fe₃O₄-on-MOF composite; (b) the concentration change of 4-nitrophenol with time.

Pd/C, 10%wt standard catalyst

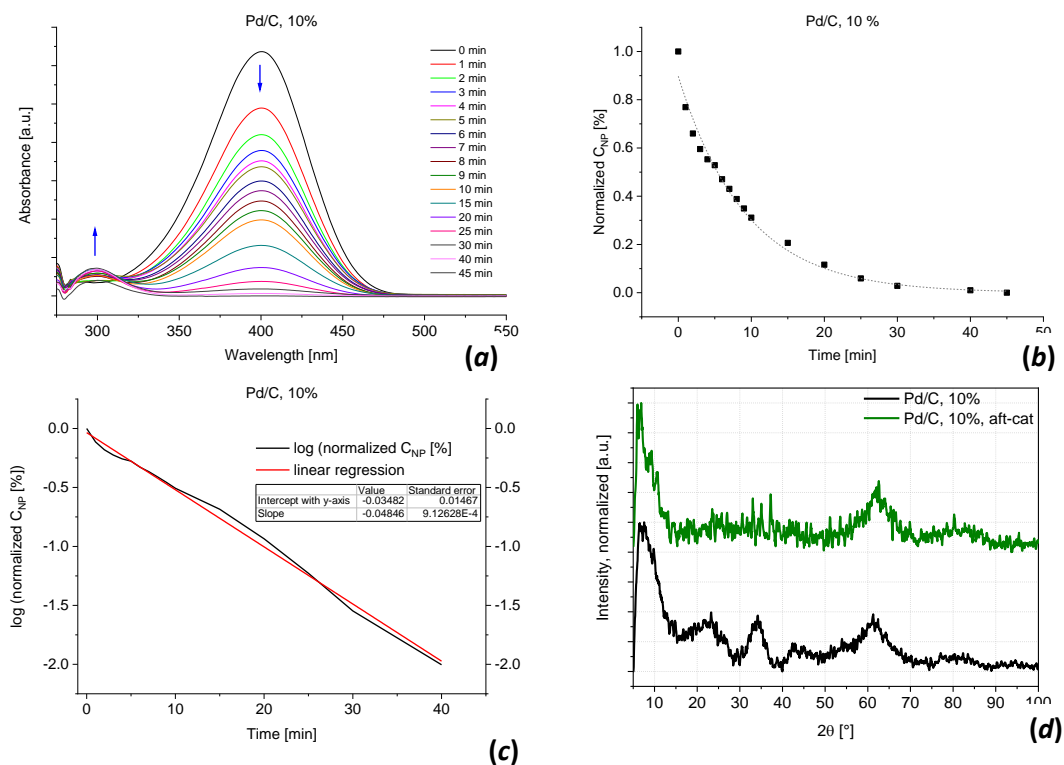


Fig. S99 (a) Temporal development of UV-vis spectra for a blank experiment with the added Pd/C catalyst and sodium borohydride; (b) the concentration change of 4-nitrophenol with time; c) $\log(c(\tau))$ graph and the respective linear regression.

Pd-on-MOFs

Pd-on-ZIF8-NP

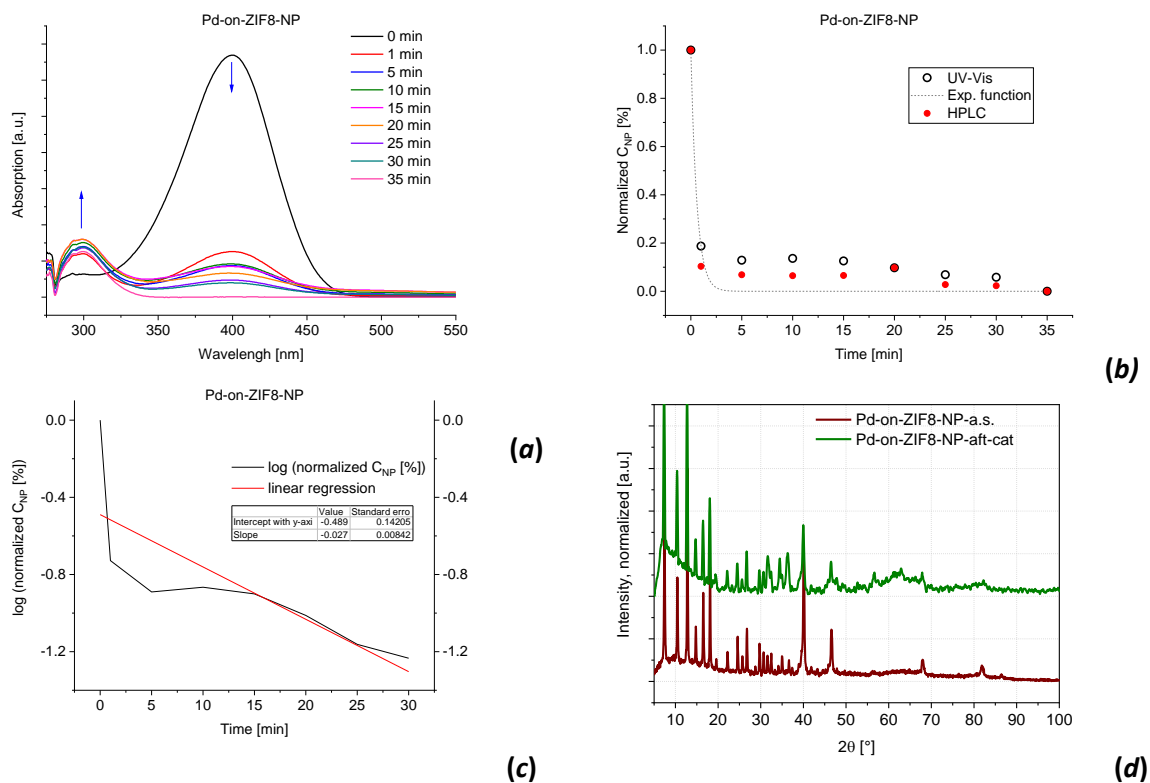


Fig. S100 (a) Temporal development of UV-Vis spectra for a blank experiment with the added Pd-on-ZIF8-NP catalyst; (b) the concentration change of 4-nitrophenol, determined by UV-Vis spectroscopy and checked by HPLC c) $\log(c(\tau))$ graph and the respective linear regression; (d) the PXRD patterns before (below) and after (above) the catalytic tests.

TEM

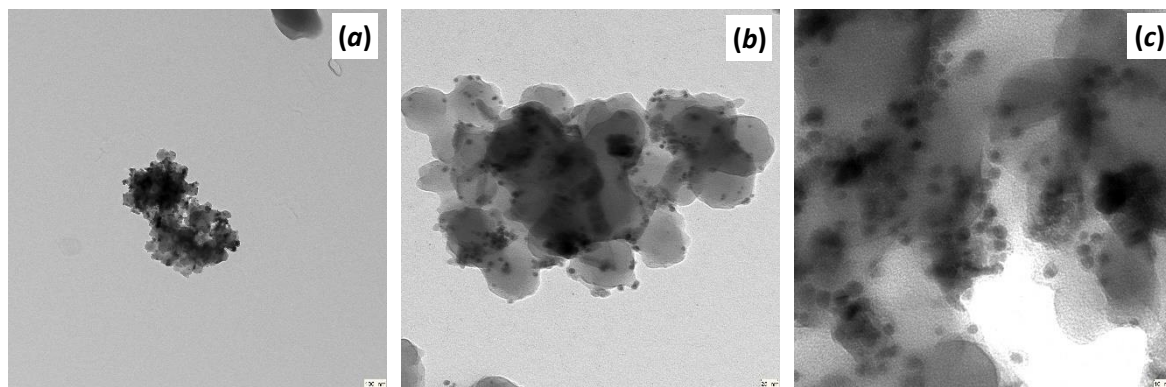


Fig. S101 (a-c) TEM images of Pd-on-ZIF8-NP after catalytic reduction of 4-nitrophenol [Pd: 7 ± 1 nm; ZIF-8: 72 ± 12 nm].

Pd-on-ZIF90NH₂

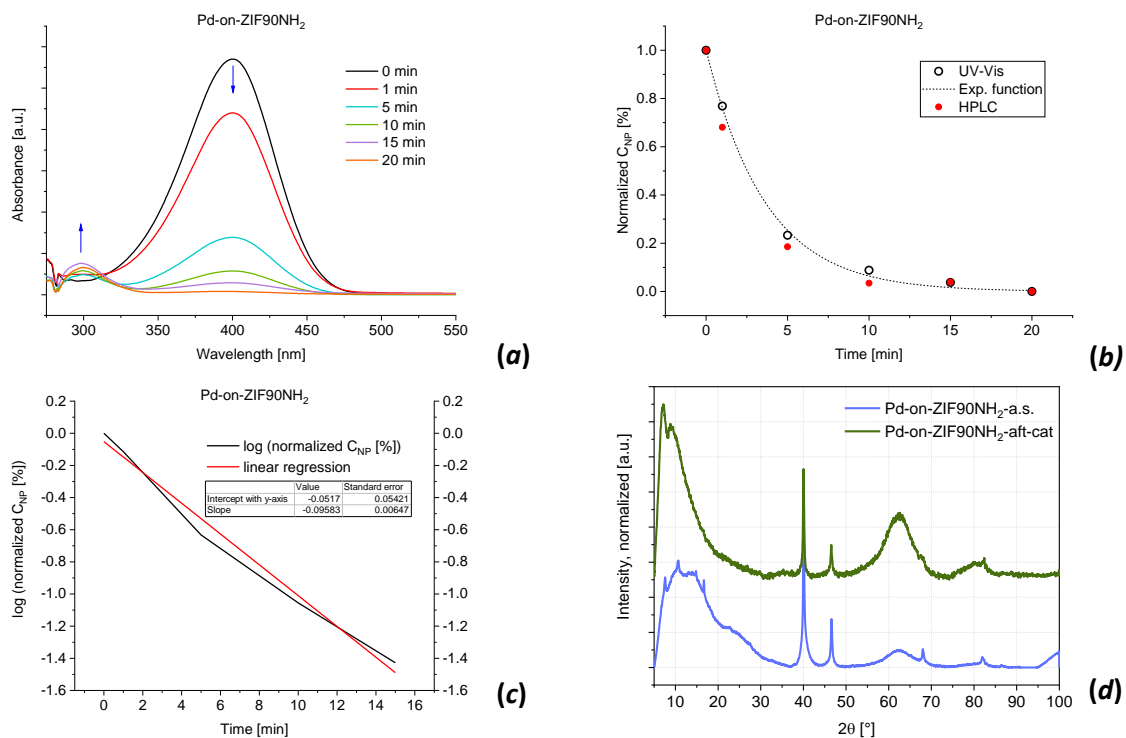


Fig. S102 (a) Temporal development of UV-Vis spectra for a blank experiment with the added Pd-on-ZIF90NH₂-catalyst; (b) the concentration change of 4-nitrophenol with time; (c) $\log(c(\tau))$ graph and the respective linear regression; (d) the PXRD patterns before (below) and after (above) the catalytic tests.

Pd-on-ZIF90NH₂-NP

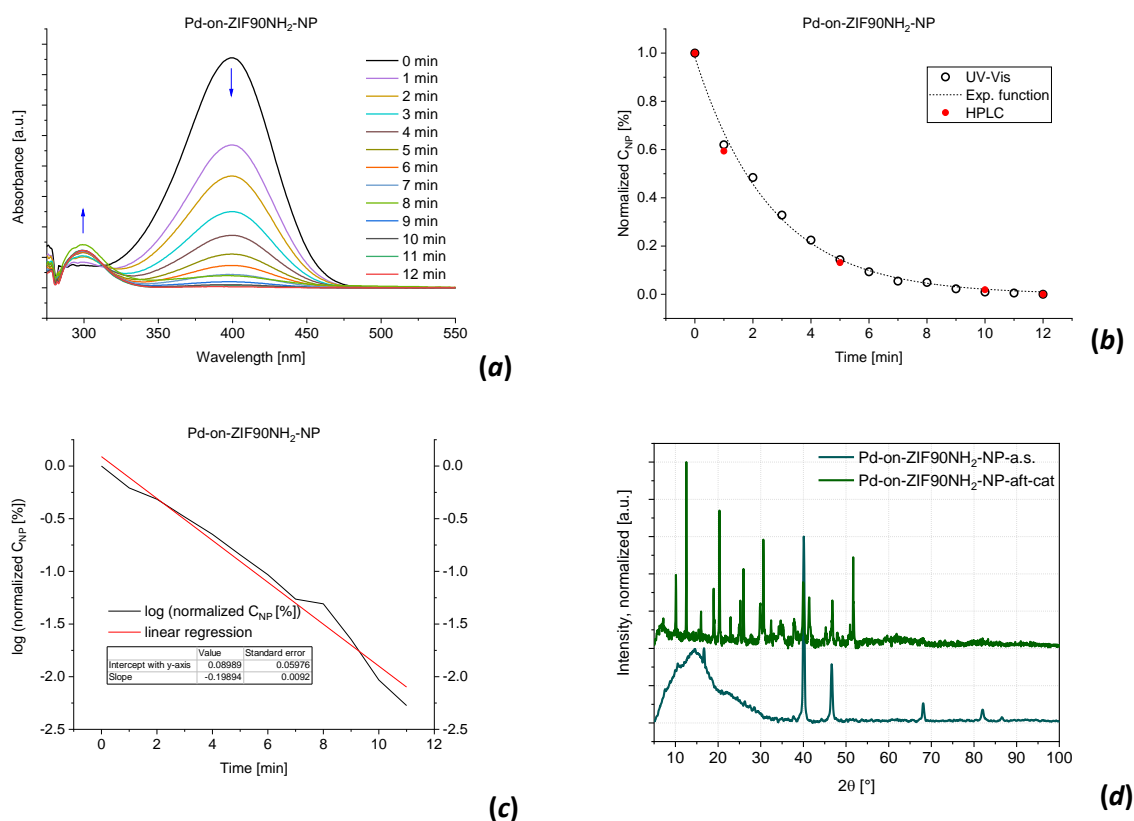


Fig. S103 (a) Temporal development of UV-Vis spectra for a blank experiment with the added Pd-on-ZIF90NH₂-NP catalyst; (b) the concentration change of 4-nitrophenol with time; c) log(c(τ)) graph and the respective linear regression; (d) the PXRD patterns before (below) and after (above) the catalytic tests.

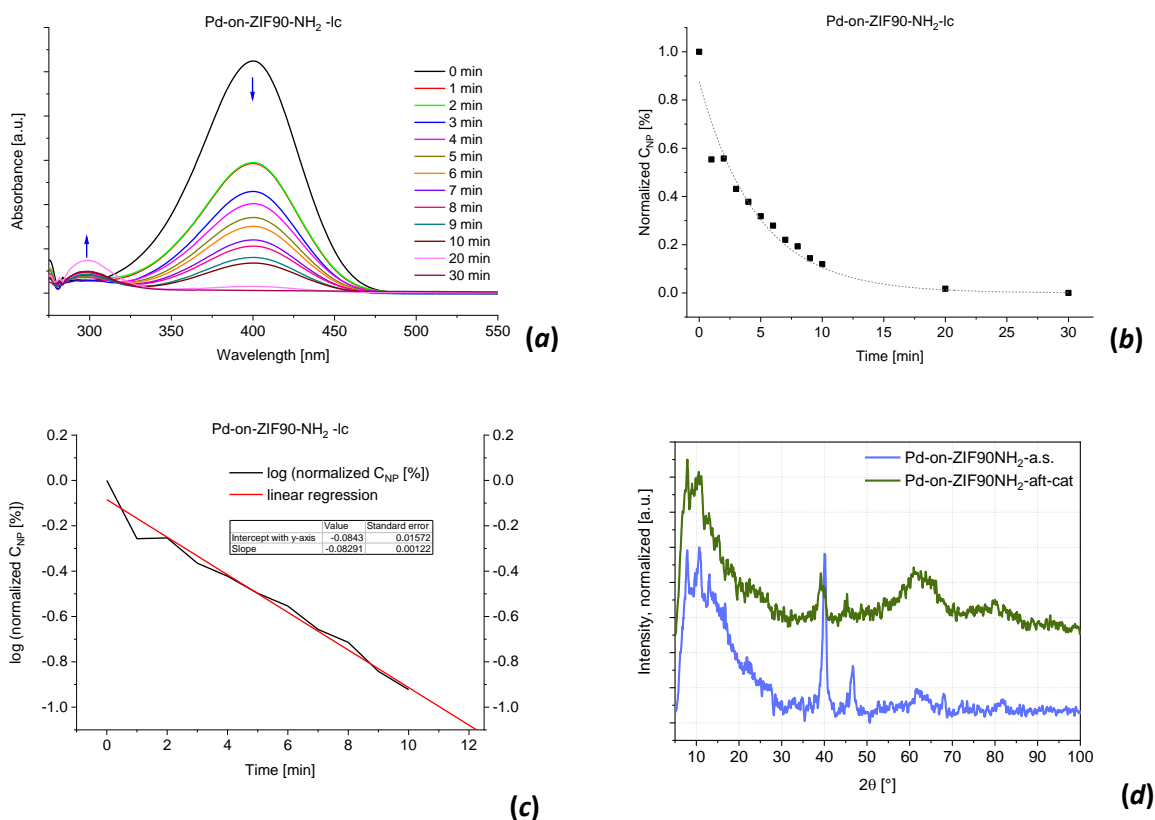


Fig. S104 (a) Temporal development of UV-Vis spectra for a blank experiment with the added Pd-on-ZIF90NH₂-lc catalyst; (b) the concentration change of 4-nitrophenol with time; (c) log($c(\tau)$) graph and the respective linear regression; (d) the PXRD patterns before (below) and after (above) the catalytic tests. .

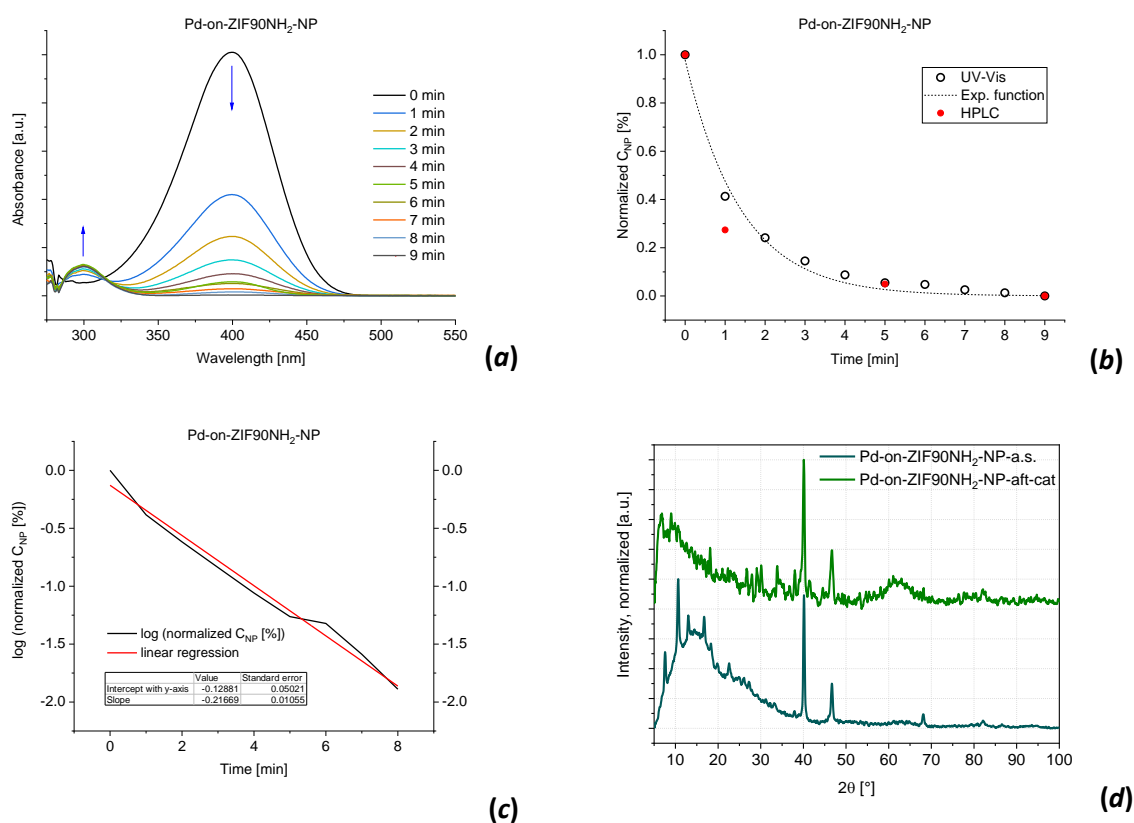


Fig. S105 (a) Temporal development of UV-Vis spectra for a blank experiment with the added Pd-on-ZIF90NH₂-NP catalyst; (b) the concentration change of 4-nitrophenol with time; (c) $\log(c(\tau))$ graph and the respective linear regression; (d) the PXRD patterns before (below) and after (above) the catalytic tests.

Pd-on-MAF66

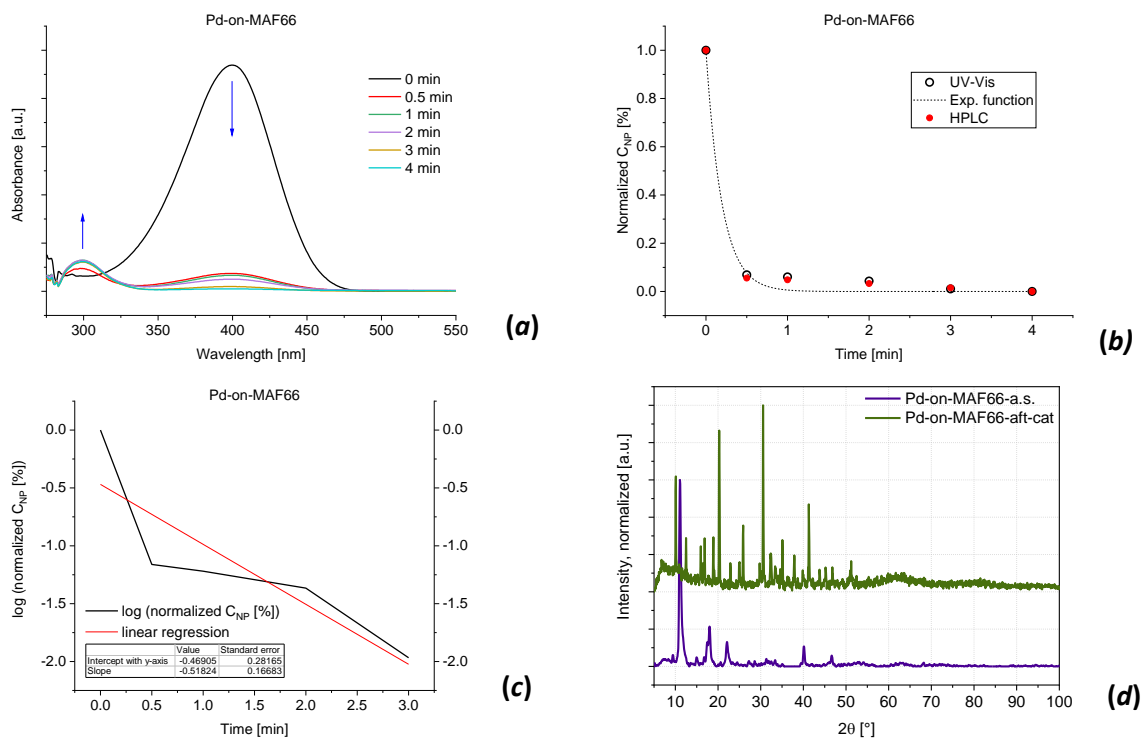


Fig. S106 (a) Temporal development of UV-Vis spectra for a blank experiment with the added Pd-on-MAF66 catalyst; (b) the concentration change of 4-nitrophenol with time; (c) $\log(c(\tau))$ graph and the respective linear regression; (d) the PXRD patterns before (below) and after (above) the catalytic tests.

Pd-on-ZIF-90-CHO (secondary experiment: substandard quality material) .

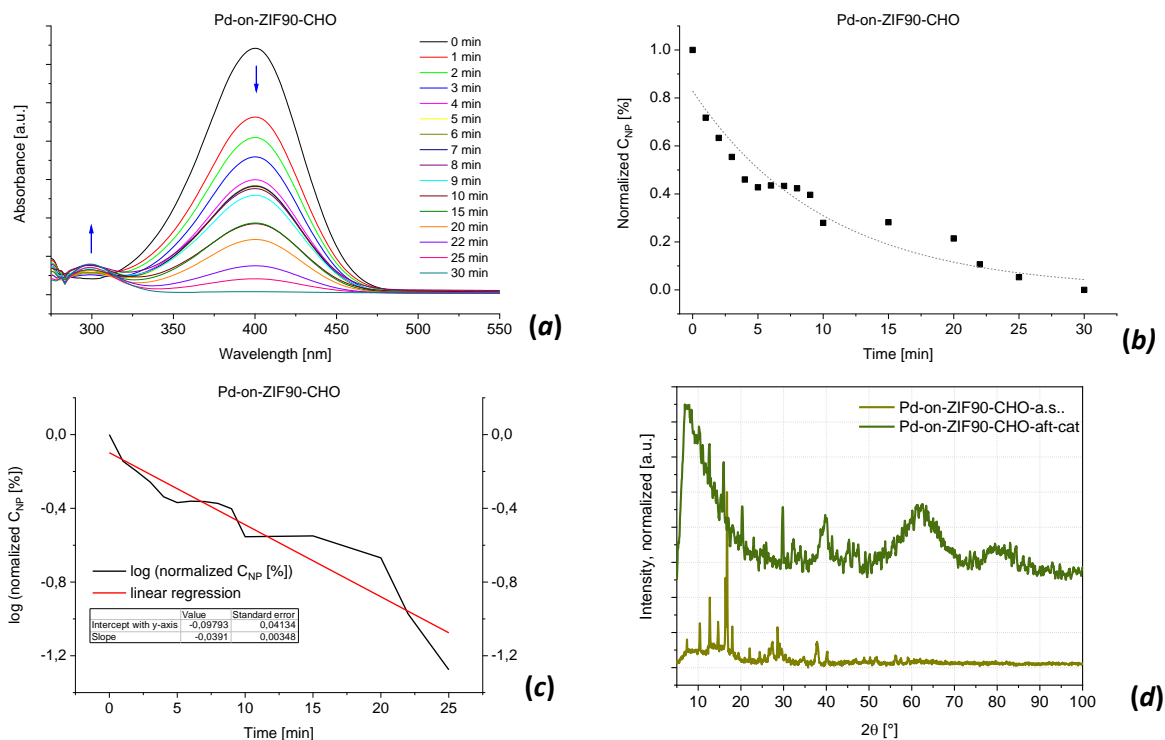


Fig. S107 (a) Temporal development of UV-Vis spectra for a blank experiment with the added Pd-on-ZIF-90-CHO catalyst; (b) the concentration change of 4-nitrophenol with time; (c) $\log(c(\tau))$ graph and the respective linear regression; (d) the PXRD patterns before (below) and after (above) the catalytic tests.

Note: the sample has a relatively poor quality regarding the crystallinity of the Pd particles (see the PXRD below) and hence it was not analyzed in-depth. The testing of kinetics was done for the sake of general comparison.

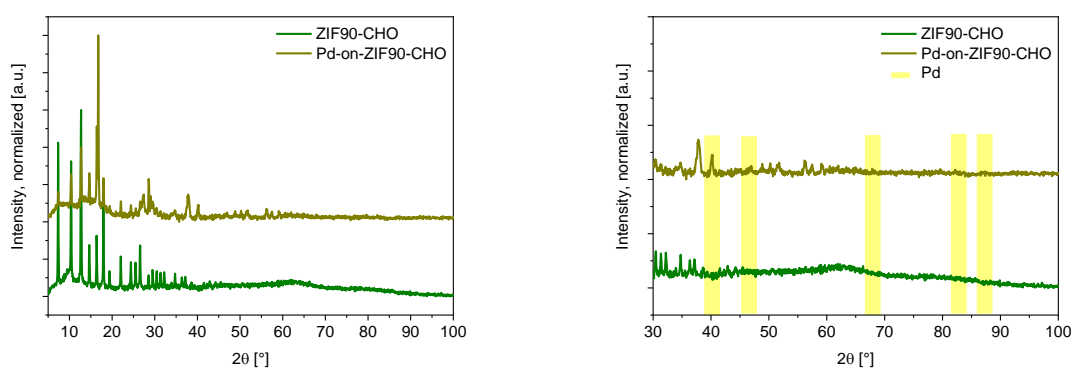


Fig. S108 PXRD spectra of the ZIF90-CHO before and after catalysis (the expansion on the right features the zones where the Pd-peaks are expected).

Pd-on-ZIF-90-COOH (secondary experiment: low quality material) .

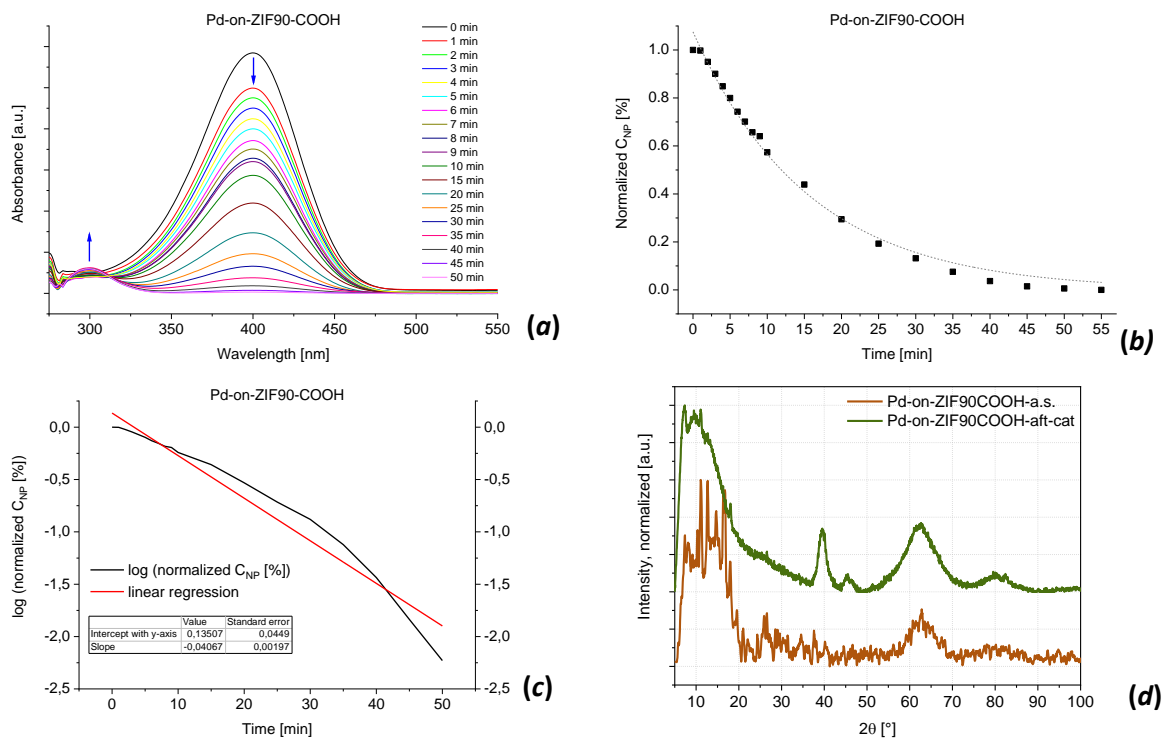


Fig. S109 (a) Temporal development of UV-Vis spectra for a blank experiment with the added Pd-on-ZIF-90-COOH catalyst; (b) the concentration change of 4-nitrophenol with time; (c) log(c(τ)) graph and the respective linear regression; (d) the PXR patterns before (below) and after (above) the catalytic tests.

Note: the sample has a particularly poor quality regarding the crystallinity of both the MOF-support and the Pd particles (see the PXR below) and hence it was not analyzed in-depth. The testing of kinetics was done as a part of general screening.

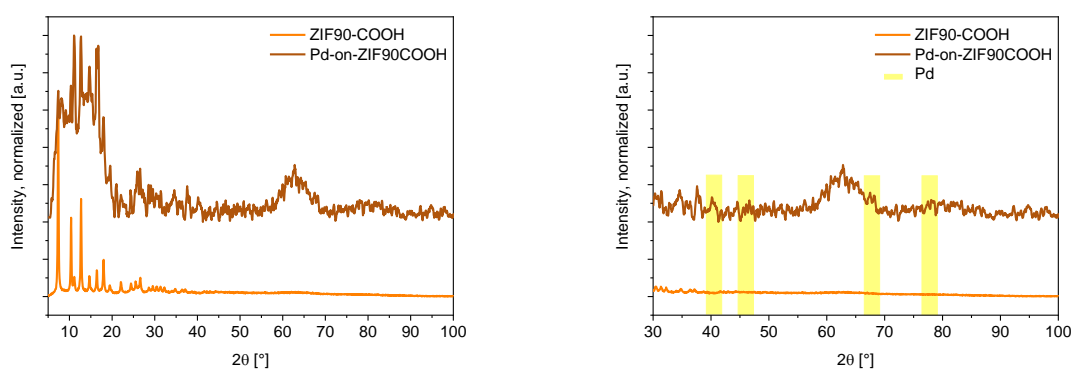


Fig. S110 PXR spectra of the ZIF90-COOH before and after catalysis (the expansion on the right features the zones where the Pd-peaks are expected).

Pd/Fe₃O₄-on-MOFs

Pd/Fe₃O₄-on-ZIF8-NP

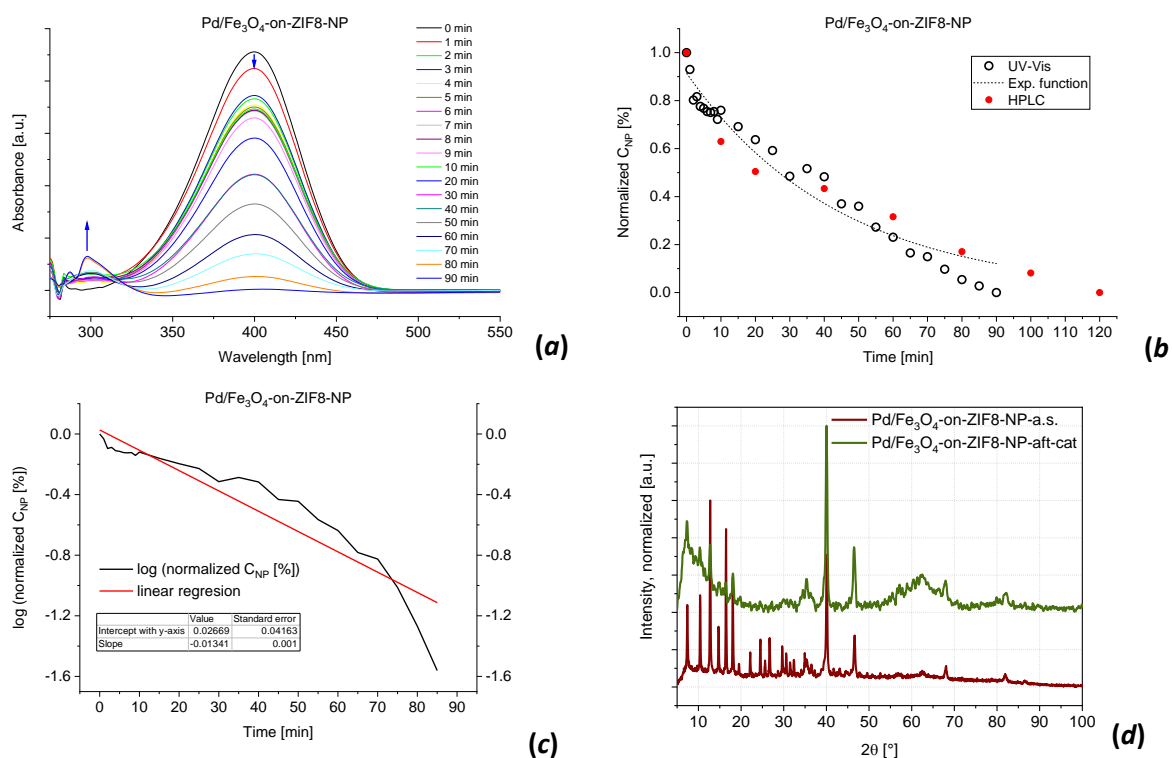


Fig. S111 (a) Temporal development of UV-Vis spectra for a blank experiment with the added Pd/Fe₃O₄-on-ZIF-8 catalyst; (b) the concentration change of 4-nitrophenol with time; (c) log(c(τ)) graph and the respective linear regression; (d) the PXRD patterns before (below) and after (above) the catalytic tests.

Pd/Fe₃O₄-ZIF90NH₂

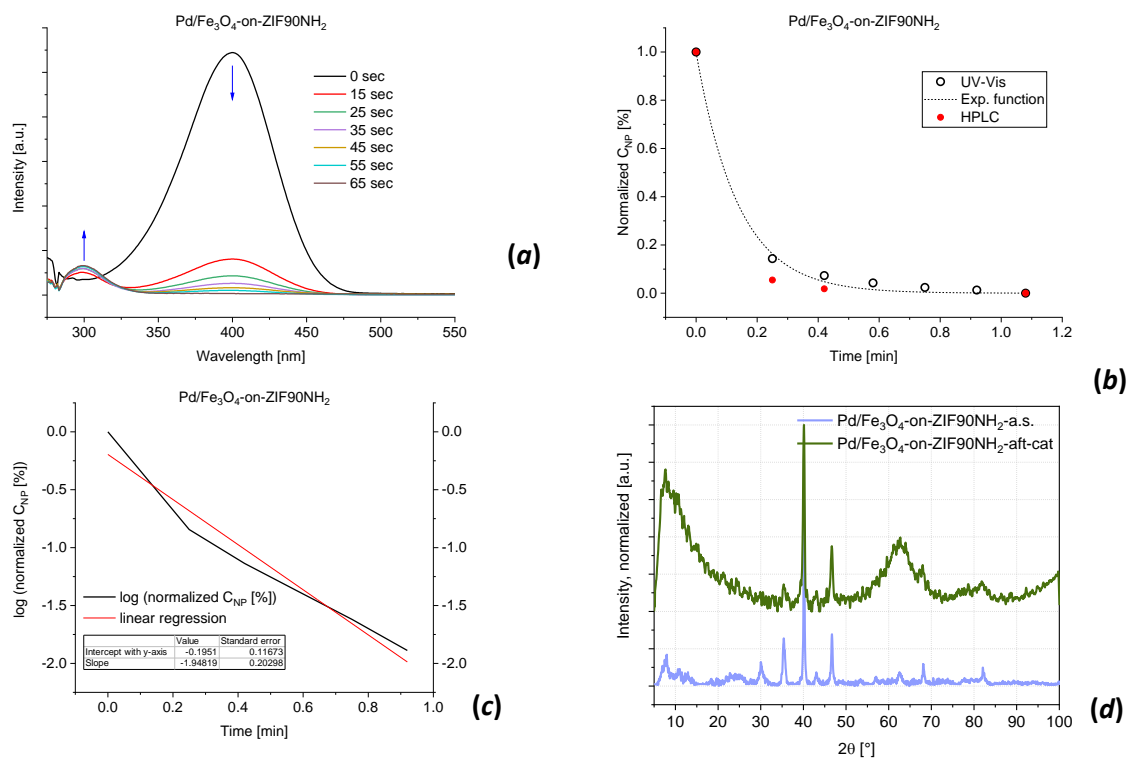


Fig. S112 (a) Temporal development of UV-Vis spectra for a blank experiment with the added Pd-Fe₃O₄-on-ZIF90NH₂-catalyst; (b) the concentration change of 4-nitrophenol with time; (c) log(c(τ)) graph and the respective linear regression; (d) the PXRD patterns before (below) and after (above) the catalytic tests.

Pd/Fe₃O₄-on-ZIF90NH₂-NP

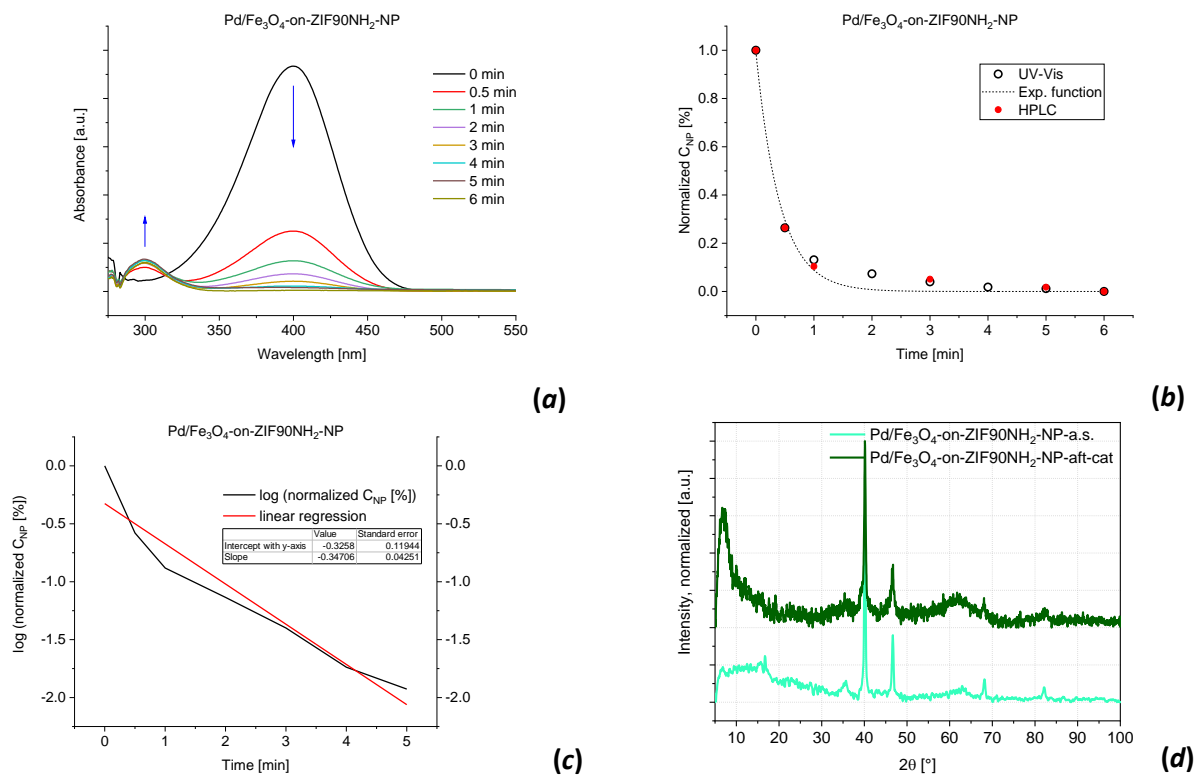
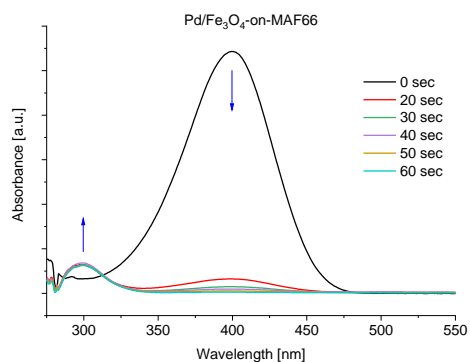
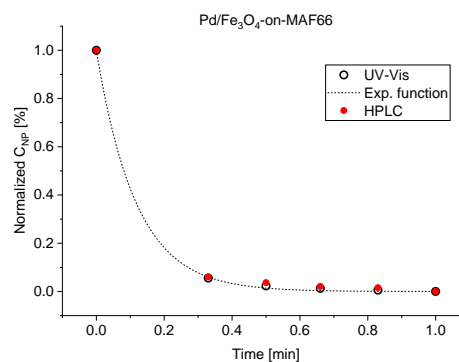


Fig. S113 (a) Temporal development of UV-Vis spectra for a blank experiment with the added Pd-Fe₃O₄-on-ZIF90NH₂-NP catalyst; (b) the concentration change of 4-nitrophenol with time; (c) log($c(\tau)$) graph and the respective linear regression; (d) the PXRD patterns before (below) and after (above) the catalytic tests.

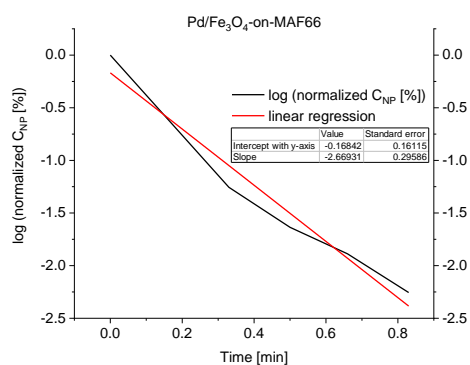
Pd/Fe₃O₄-on-MAF66



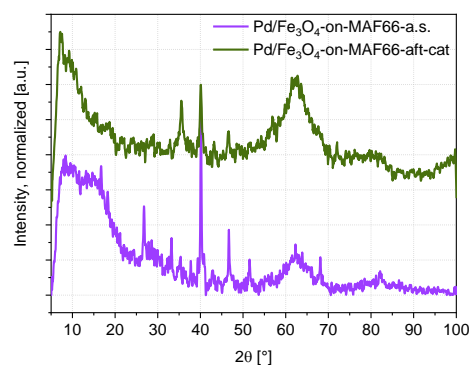
(a)



(b)



(c)



(d)

Fig. S114 (a) Temporal development of UV-Vis spectra for a blank experiment with the added Pd-Fe₃O₄-on-MAF66 catalyst; (b) the concentration change of 4-nitrophenol with time; (c) log(c(τ)) graph and the respective linear regression; (d) the PXRD patterns before (below) and after (above) the catalytic tests.

Fe₃O₄/Pd-on-MOFs

Fe₃O₄/Pd-on-ZIF8-NP

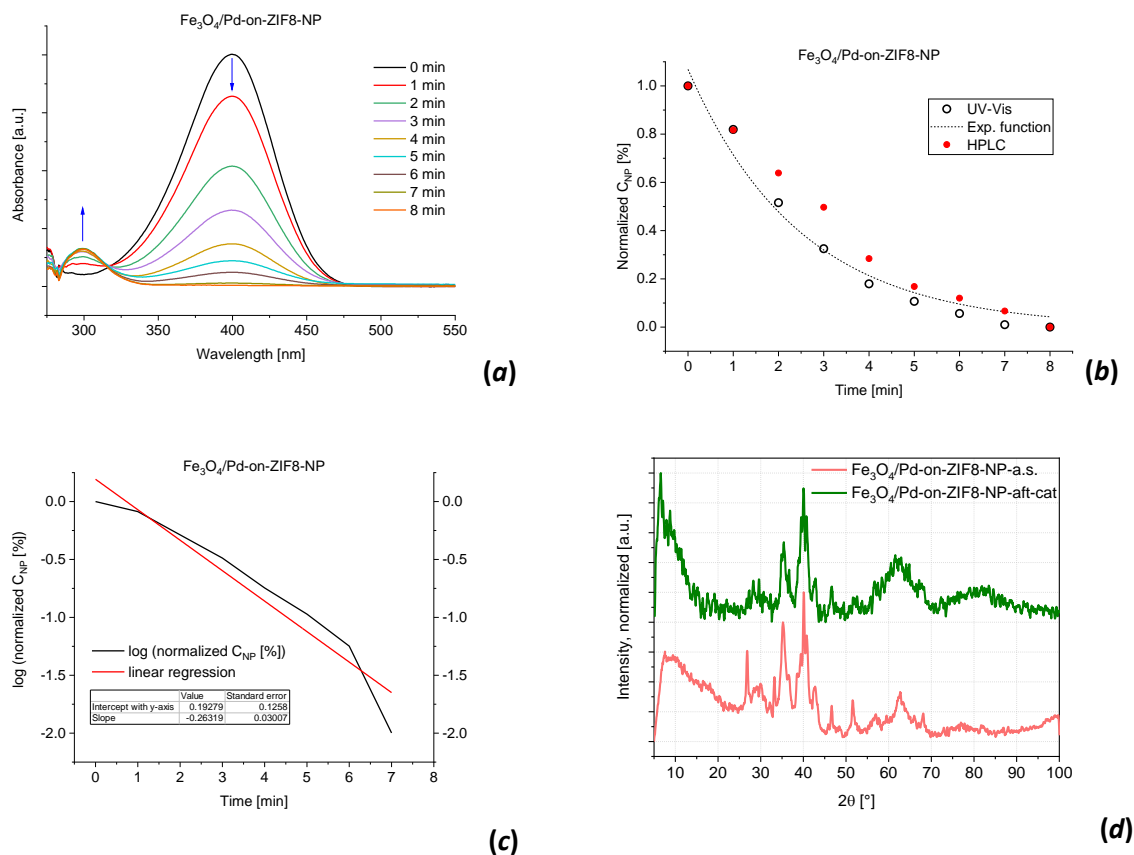


Fig. S115 (a) Temporal development of UV-Vis spectra for a blank experiment with the added Fe₃O₄-Pd-on-ZIF8-NP catalyst; (b) the concentration change of 4-nitrophenol with time; (c) log(c(τ)) graph and the respective linear regression; (d) the PXRD patterns before (below) and after (above) the catalytic tests.

Fe₃O₄/Pd-on-ZIF90NH₂-NP

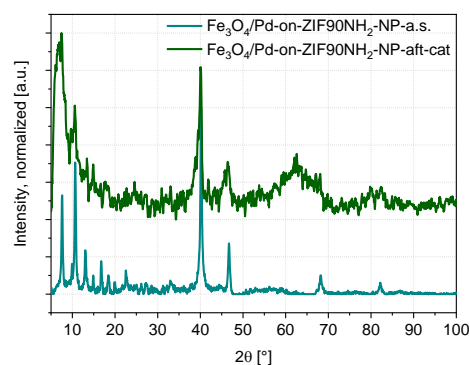
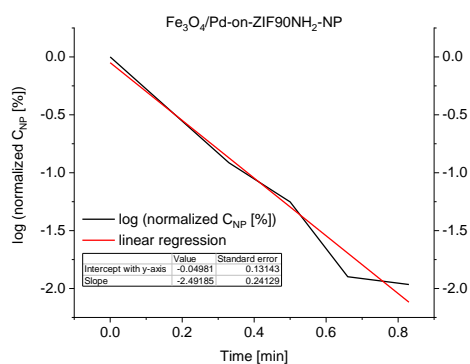
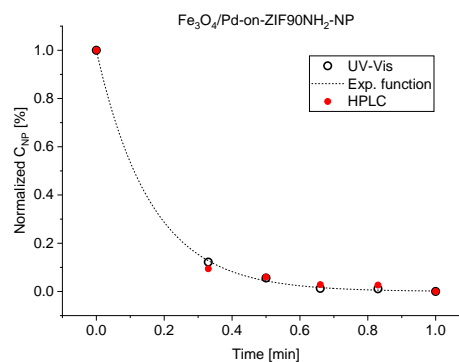
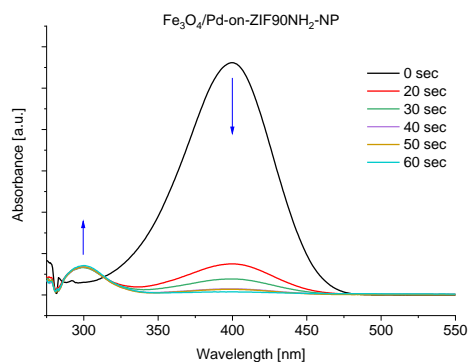


Fig. S116 (a) Temporal development of UV-Vis spectra for a blank experiment with the added Fe₃O₄-Pd-on-ZIF90NH₂-NP catalyst; (b) the concentration change of 4-nitrophenol with time; (c) log(c(τ)) graph and the respective linear regression; (d) the PXRD patterns before (below) and after (above) the catalytic tests.

7.2 Hydrogenation of cyclohexene

Hydrogenation set-up: the hydrogenation was performed in a glass insert, equipped with the magnetic stirrer in a stainless-steel autoclave (Fig. 114). In order to keep the volume low, 10 ml MW-reactor glass tubes, similar to the ones used for the MW-assisted syntheses of the composite NPs were used (functionally, only the robustness of the thick-wall reactor tubes were used in this case). Strong rare-earth metal magnets were proven to be necessary for efficient stirring, due to significant separation from the magnetic stirrer (this might mean that the results featuring the Fe_3O_4 -containing magnetic composite NPs, secondary in importance, are only of qualitative use. The preservation of the identity of Fe_3O_4 under the aggressive hydrogenation conditions was also not proven).



Fig. S117 The hydrogenation set-up. Left to right:

- Cap of the autoclave with the manometer and valves,
- Aluminum thermostat (heated directly on the stirrer-hotplate; the small holes are the thermometric probe inlets. Alternatively, silicon-bath with inferior precision of the thermal control was also used in early experiments),
- Bottom part of the autoclave

Autoclave insert with the glass reaction tube (the insert serves the minimization of the residual volume; the removable screw acts as an extractor).

Gas exchange in the autoclaves: the ambient air was triple exchanged first by N_2 gas (filling at ~ 2 bars and emptying against atmospheric pressure under stirring). A triple exchange by H_2 -gas was followed strictly without stirring (filling at ~ 4 -5 bars and slow emptying against atmospheric pressure. It is implied that in the absence of stirring the reaction rates were negligible compared

with the case of stirring. This assumption is evidently correct only for reactions, relatively slow at room temperature – the majority of cases in this work –because the H₂ gas exchange causes some foaming and, hence, mixing).

H₂ pressure control: the hydrogenation was done using the Büchi pressflow controller hydrogenation system (bpc). The addition of H₂ was performed automatically to maintain the given pressure, while the volume/amount of the added gas was measured against time, serving as a primary analytical tool for fast assessment.

Method, catalytic experiment: a 10 mL reaction tube was charged in the air by the composite-catalyst, the substrate (typically cyclohexene), and the internal standard/solvent (typically octane, in some cases decane). The tube was transferred to an autoclave and sealed. After the exchange of the atmosphere to H₂, the autoclave was transferred to the preheated thermostat / bath. After ~20 min of thermostating, the pressure of H₂ had been set to nominal (typically 2 bars) and the stirring has been started, marking the starting time point. The reaction monitoring was performed *via* observing the amount of H₂ consumed.

At the time, corresponding to the end of the experiment, the H₂ feed was stopped, the overpressure accurately vented and the stirring was switched off, marking the final time. The autoclave was removed from the thermostat / bath and left to be cooled. The glass tube was extracted, the stirring rod removed, and the residue centrifuged out (in selected cases it was stored for subsequent experiments after ×3 washing with the same solvent, as had been used in the reaction, and drying in 10⁻³ Torr vacuum at room temperature during a few hours). The obtained solution was analyzed by gas chromatography (GC) to estimate the final yield and, in selected cases, compare the result with the monitoring based on H₂-adsorption.

Analytics, methodology

The yield for was calculated using a simplified formula (see a short explanation of the limitations below):

$$\text{Yield}(\text{product}) : C_{\text{product}} / (C_{\text{product}} + C_{\text{substrate}}) \quad (\text{Eq. 7.5})$$

$$\text{Yield}(\text{product}) = \frac{C_{\text{product}}}{C_{\text{product}} + C_{\text{substrate}}} = \frac{\frac{C_{\text{ref,product}}}{I_{\text{ref,product}}} * I_{\text{product}}}{\frac{C_{\text{ref,product}}}{I_{\text{ref,product}}} * I_{\text{product}} + \frac{C_{\text{ref,substrate}}}{I_{\text{ref,substrate}}} * I_{\text{substrate}}} \quad (\text{Eq. 7.6})$$

Where the C_{compound} is the concentration of the respective compound calculated from the $F_{\text{cal}} = C_{\text{compound}}(I_{\text{compound}})$ calibration function, where C_{compound} is the concentration of the compound,

while I_{compound} is the integral intensity, *i.e.* area under the peak. While the calibration function was highly linear and passing through (0,0) point with reasonable precision in all cases, the $C_{\text{compound}} = (C_{\text{ref}}/I_{\text{ref}}) * I_{\text{compound}}$ approximation, where $C_{\text{ref, compound}}/I_{\text{ref, compound}}$ is the slope of the $c(I)$ dependence for the respective compound, was used.

When the reaction was performed with a standard, the yield was calculated using the standard as the reference (the approach is exactly the same, if the calibration curves are strictly linear and their intercepts are zero. If carried out consequently, the relation to the intermediary concentrations of the standard could give better precision. The results in this work were very close, the tabulated yields are given interchangeably).

$$\text{Yield}(\text{product, standard based}) = \frac{I_{\text{product}} / (\text{RRF}_{\text{product:standard}})}{(I_{\text{product}} / (\text{RRF}_{\text{product:standard}})) + (I_{\text{substrate}} / (\text{RRF}_{\text{substrate:standard}}))} \quad (\text{Eq. 7.7})$$

Where I_{compound} is the area under the peak for the respective compound, while RRF is the *relative response factor*, used to relate the response signal intensities of the analyte to the response signal of the standard ($\text{RRF}_{\text{compound:standard}} = (I_{\text{ref, compound}}/C_{\text{ref, compound}})/(I_{\text{ref, standard}}/C_{\text{ref, standard}})$), at $I_{\text{ref-S}}$ interpolated to be equal to the respective I_{compound} concentrations. Due to linearity and negligible intercept of the calibration curves the approximated $I_{\text{compound}}(C_{\text{compound}})$ slopes were used in this work).

The limitation of the taken approach is that it explicitly takes as granted that $C_{\text{substrate}}(0) = C_{\text{substrate}}(t) + C_{\text{product}}(t)$, where $C_{\text{compound}}(t)$ is the respective concentration at time t. This assumption neglects the possible formation of side products and/or intermediaries (like in the case of the hydrogenation of cyclohexene those could be 1,3-cyclohexadiene and benzene).

To avoid cases, when the assumption of significant discrepancies the obtained the yield was compared with the

$$\text{Yield}(\text{product, cross-check}) = \frac{C_{\text{product}}(\text{time final})}{C_{\text{substrate}}(0)} \quad (\text{Eq. 7.8})$$

If the discrepancy was more than ~10% the result was not analyzed further (there were only a few cases, which might be indications of high experimental errors. *No accumulation of significant amounts of side products were observed*).

8 References

- [1] "Match!" software. Crystal Impact - Dr. H. Putz. GbR, Kreuzherrenstr. 102, 53227 Bonn, Ger. <http://www.crystalimpact.com/diamond>.
- [2] J. Cravillon, R. Nayuk, S. Springer, A. Feldhoff, K. Huber, and M. Wiebcke, *Chem. Mater.*, 2011, **23**, 2130–2141.
- [3] W.-S. Lo, S.-M. Liu, S.-C. Wang, H.-P. Lin, N. Ma, H.-Y. Huang, and F.-K. Shieh, *RSC Adv.*, 2014, **4**, 52883–52886.
- [4] D. Hua, Y. K. Ong, Y. Wang, T. Yang, and T.-S. Chung, *J. Memb. Sci.*, 2014, **453**, 155–167
- [5] C.-I. Yen, S.-M. Liu, W.-S. Lo, J.-W. Wu, Y.-H. Liu, R.-J. Chein, R. Yang, K. C.-W. Wu, J. R. Hwu, N. Ma, and F.-K. Shieh, *Chem. - A Eur. J.*, 2016, **22**, 2925–2929.
- [6] R.-B. Lin, D. Chen, Y.-Y. Lin, J.-P. Zhang, and X.-M. Chen, *Inorg. Chem.*, 2012, **51**, 9950–9955.
- [7] S. Gražulis, D. Chateigner, R. T. Downs, A. F. T. Yokochi, M. Quirós, L. Lutterotti, E. Manakova, J. Butkus, P. Moeck, and A. Le Bail, *J. Appl. Crystallogr.*, 2009, **42**, 726–729.
- [8] *Kirk-Othmer Encyclopedia of Chemical Technology*; John Wiley & Sons, 2000.
- [9] M. J. Vaidya, S. M. Kulkarni, and R. V. Chaudhari, *Org. Process Res. Dev.*, 2003, **7**, 202–208.
- [10] Eckenfelder, W. W. *Industrial Water Pollution Control* Vol. 1 (ed W. W., Eckenfelder) Ch. 1, 1–4 (McGraw-Hill Science, 1999).
- [11] Z. Wu, X. Yuan, H. Zhong, H. Wang, G. Zeng, X. Chen, H. Wang, L. Zhang, and J. Shao, *Sci. Rep.*, 2016, **6**, 25638.
- [12] Reduction of Nitro Compounds to Amines, Azo Compounds, Hydroxylamines, and Oximes, and Reduction of N-Oxides to Amines. In *Catalytic Reduction in Organic Synthesis 2*; de Vries, J. G., Ed.; Georg Thieme Verlag: Stuttgart, 2018.
- [13] B. Xu, X. Li, Z. Chen, T. Zhang, and C. Li, *Microporous Mesoporous Mater.*, 2018, **255**, 1–6.